UNIVERSIDADE ESTADUAL DE CAMPINAS
FACULDADE DE ENGENHARIA MECÂNICA

MAURICIO RAMACCIATO MASSAROTTI

Aeroacoustics of Automotive Roof Crossbars

Aeroacústica de Barras Transversais de Teto Automotivas

CAMPINAS
2017

Mauricio Ramacciato Massarotti

Aeroacoustics of Automotive Roof Crossbars

Aeroacústica de Barras Transversais de Teto Automotivas

Dissertation presented to the School of Mechanical Engineering of the University of Campinas in partial fulfillment of the requirements for the degree of Master in Mechanical Engineering, in the area of Thermal and Fluids.

Dissertação apresentada à Faculdade de Engenharia Mecânica da Universidade Estadual de Campinas em preenchimento parcial dos requisitos para obtenção do título de Mestre em Engenharia Mecânica, na área de Térmica e Fluidos.

Orientador: William Roberto Wolf

Este exemplar corresponde à versão final da dissertação defendida pelo aluno Mauricio Ramacciato Massarotti, e orientada pelo Prof. Dr. William Roberto Wolf.

Assinatura do Orientador

_____

Campinas

2017

Agência(s) de fomento e nº(s) de processo(s): Não se aplica.

Ficha catalográfica
Universidade Estadual de Campinas
Biblioteca da Área de Engenharia e Arquitetura
Luciana Pietrosanto Milla - CRB 8/8129

M382a

Massarotti, Mauricio Ramacciato, 1985-
Aeroacoustics of automotive roof crossbars / Mauricio Ramacciato Massarotti. – Campinas, SP : [s.n.], 2017.

Orientador: William Roberto Wolf.
Dissertação (mestrado) – Universidade Estadual de Campinas, Faculdade de Engenharia Mecânica.

1. Ruido aerodinamico. 2. Elipse (Geometria). I. Wolf, William Roberto, 1980-. II. Universidade Estadual de Campinas. Faculdade de Engenharia Mecânica. III. Título.

Informações para Biblioteca Digital

Título em outro idioma: Aeroacústica de barras transversais de teto automotivas
Palavras-chave em inglês:
Aerodynamic noise
Ellipse (Geometry)
Área de concentração: Térmica e Fluídos
Titulação: Mestre em Engenharia Mecânica
Banca examinadora:
William Roberto Wolf [Orientador]
Rogério Gonçalves dos Santos
Carlos Roberto Ilário da Silva
Data de defesa: 01-12-2017
Programa de Pós-Graduação: Engenharia Mecânica

UNIVERSIDADE ESTADUAL DE CAMPINAS

FACULDADE DE ENGENHARIA MECÂNICA

COMISSÃO DE PÓS-GRADUAÇÃO EM ENGENHARIA MECÂNICA

DEPARTAMENTO DE TERMICA E FLUIDOS

DISSERTAÇÃO DE MESTRADO ACADÊMICO

Aeroacústica de Barras Transversais de Teto Automotivas

Autor: Mauricio Ramacciato Massarotti

Orientador: William Roberto Wolf

A Banca Examinadora composta pelos membros abaixo aprovou esta dissertação:

Prof. Dr. William Roberto Wolf
Instituição UNICAMP

Prof. Dr. Rogério Gonçalves dos Santos
Instituição UNICAMP

Prof. Dr. Carlos Roberto Ilário da Silva
Instituição EMBRAER

A Ata da defesa com as respectivas assinaturas dos membros encontra-se no processo de vida acadêmica do aluno.

Campinas, 1 de Dezembro de 2017.

Acknowledgments

Few people are natural leaders and have the ability to inspire and motivate others with authenticity at the same time they are extremely good people to work and live with. This thesis is primarily dedicated to Prof. William Wolf and to Yuri Ribeiro Silva, two of those personalities who have supported the execution of this project with endeavor.

I am thankful to Prof. José Arruda from UNICAMP for connecting me with Prof. William Wolf, and to Prof. Rogério Gonçalves Santos and Prof. Rafael Glaber Gontijo for their great contribution in the qualification of this thesis. I am glad as well to the companion and support from the students of the Laboratory of Aeronautical Sciences at UNICAMP: Cristiano Pimenta, Jean Marques, Renato Miotto, Tulio Riccardi, Walter Ramirez, Luiz Schiavo, Bruno Backes, Brener d'Lélis, Lucas Mascagni, and so many others who have been working together in the classrooms and Laboratory.

I am also thankful to the General Motors South America (GMSA) technicians who have worked hard in the preparation and execution of the track tests: Alexandre Ceccato, Jean Souza, Thiago Turri and Rafael Silva. I also thank the GMSA Leadership Marcelo Maturano and Luiz Eduardo Martins for coping with the project amid programs' workload. I also appreciate the efforts from the General Motors North America (GMNA) Wind Noise Team (Christopher L. Banks and James Zunich) in supporting the correlation tests performed in the GMNA Aeroacoustic Wind Tunnel.

At last, I am grateful to the support of my family, Delcides, Aparecida and Luciana R. Massarotti, for their understanding of all the spare time invested on this project, despite they never really understood why it was taking so long. Now they might.

Ainda não terminou isso, Mauricio?
Mom

Abstract

Aeroacoustic noise reduction is one of the growing concerns in the automotive industry. With the advention of Electric Vehicles and Autonomous Driving, vehicle occupants will become more exposed to aerodynamic noise. The most severe aeroacoustic phenomena in ground vehicles are the ones with a tonal nature. Roof carrier systems have a leading crossbar directly exposed to the airflow, generating broadband noise and a discrete aeolian tone. Nowadays, most of the applied solutions to aeolian tone are empirical, sustained by the fact that commercial crossbar profiles are not as blunt as a circular cylinder, neither as thin as a wing section. The objective of this project is to investigate the noise mechanisms involved in elliptical crossbars through actual acoustic measurements taken on track. The first part of the project correlated sound pressure and intensity measurements taken on track and in an aeroacoustic wind tunnel, with the objective of assessing track data accuracy and repeatability. Acoustic pressure measured outside the vehicle with a single microphone has demonstrated good accuracy in capturing both narrow and broadband noise effects, despite of the uncontrolled background noise. The crossbar wake interaction with the roof plane was also assessed through reference measurements and local flow visualization. The second part of the project compared the noise generated by an elliptical cylinder with that generated by a circular cylinder and a NACA 0012 airfoil with the same thicknesses and at the same operational conditions. Results have shown that the elliptical crossbar noise characteristics have similarities when compared to those of blunt bodies at low Reynolds numbers and wing sections at higher speeds. The following step investigated the effects of the ellipse geometry and angle of attack on the generated sound. Different leading and trailing edge combinations were tested and demonstrated that the trailing edge is the key contributor to the aeolian tone characteristics, while the leading edge affects primarily the broadband noise. Thin trailing edges were capable to completely eliminate the aeolian tone. Positive and negative incidence angles presented opposite trends towards noise reduction and have proven to be ineffective in higher speeds. Finally, industry-known solutions such as Boundary Layer Tripping (BLT) were assessed and compared to innovative solutions (Trailing Edge Blowing (TEB) and Perforation). Both TEB and Perforation were effective on reducing the aeolian tone but presented side effects such as high frequency whistling.

Keywords: Aeroacoustics, Tonal noise, Blunt body, NACA 0012, Elliptical cylinder.

Resumo

Redução de ruído aeroacústico é uma crescente preocupação na indústria automotiva. Com a proliferação de Veículos Elétricos e Direção Autônoma, os ocupantes de um veículo estarão mais suscetíveis a ruídos aerodinâmicos. Os fenômenos aeroacústicos de natureza tonal são os mais severos em veículos automotores. Bagageiros de teto possuem uma barra transversal diretamente exposta ao escoamento e geram ruído em banda larga e um tonal aeólico característico. Atualmente, as soluções aplicadas ao ruído tonal são empíricas, sustentadas pelo fato de os perfis comerciais não serem rombudos como um cilindro, nem finos como um perfil de asa. O objetivo deste trabalho é investigar os mecanismos de geração de ruído em barras transversais de teto com perfil elíptico, através de medições acústicas em pista. Na primeira parte do projeto, medições de pressão e intensidade sonora feitas em pista e em túnel de vento aeroacústico foram correlacionadas com o objetivo de avaliar a precisão e repetitividade dos testes em pista. A medição de pressão sonora com um único microfone posicionado fora do veículo se demonstrou um método preciso na captura de efeitos de banda larga e estreita, apesar da condição não controlada do ruído de fundo. A interação da esteira da barra com o teto também foi avaliada através de medições acústicas de referência e visualização de escoamento. Na segunda parte, o ruído gerado por um perfil elíptico foi comparado ao ruído gerado por um cilindro circular e por um perfil NACA 0012 de mesma espessura e nas mesmas condições de operação. Os resultados mostraram que as características do ruído do perfil elíptico se aproximam às do cilindro circular em números de Reynolds mais baixos, e às do perfil NACA 0012 em velocidades mais altas. Na etapa seguinte, investigou-se o efeito de alterações geométricas do perfil elíptico no ruído gerado. Diferentes combinações de bordo de ataque e fuga foram testadas e demonstraram que o bordo de fuga é o principal contribuinte para o ruído tonal, enquanto que o bordo de ataque está associado ao ruído em banda larga. Bordos de fuga finos foram capazes de eliminar completamente o ruído tonal. Ângulos de incidência positivos e negativos apresentaram tendências contrárias em relação à redução de ruído, e se demonstraram soluções não efetivas em altas velocidades. Por final, soluções conhecidas como perturbação da camada limite foram testadas e comparadas com soluções inovadoras (Assopramento e Perfuração). Ambas técnicas reduziram efetivamente o ruído tonal mas apresentaram efeitos indesejados como a excitação de tons em alta frequência.

Palavras-chave: Aeroacústica, Ruído tonal, Corpos rombudos, NACA 0012, Elipse.

List of Figures

List of Acronyms

Latin Letters

A_b	Total blowing jet area
AI	Articulation Index
AR	Aspect Ratio
c	Chord
c_0	Speed of sound in free-stream
F_i	Dipole source distribution
G_{12}	Cross spectra
h	Thickness
$H(f)$	Heaviside function
M_∞	Free stream Mach number
L_I	Intensity Level
L_P	Pressure Level
p'	Acoustic pressure
Q_i	Monopole source distribution
R^2	Coefficient of Determination
Re	Reynolds Number
Re_c	Reynolds Number based on the chord
t	Time
T_{ij}	Lighthill stress tensor
u	Velocity component along x-axis
U_b	Blowing jet flow speed
U_∞	Free stream velocity
v	Velocity component along y-axis
$\dot{V}$	Air Conditioning volumetric flow rate
x	Abscissa of the Cartesian plane
y	Ordinate of the Cartesian plane

Greek Letters

α	Angle of Attack
$\delta(f)$	Dirac delta function
δ_{ij}	Kronecker delta
Δr	Spacing between two microphones
λ	Wavelength
μ	Dynamic viscosity
ν	Kinematic viscosity
ω	Angular frequency
π	Pi
ρ	Air density
θ	Angle to the source

Abbreviations

AoA	Angle of Attack
AC	Air Conditioning
BEM	Boundary Element Method
BL	Boundary Layer
BLT	Boundary Layer Tripping
CAA	Computational Aeroacoustics
CAPG	Cruz Alta Proving Ground
CFD	Computational Fluid Dynamics
FW-H	Ffowcs Williams–Hawkings (Acoustic Analogy)
FWH	Ffowcs Williams & Hall (trailing-edge noise theory)
DNS	Direct Numerical Simulation
DOF	Degree of Freedom
EXT	Exterior
FFT	Fast Fourier Transform
GMAL	General Motors Aero Lab
GMNA	General Motors North America
GMSA	General Motors South America
INT	Interior
LE	Leading Edge
LES	Large Eddy Simulation

Lwr	Lower
N&V	Noise & Vibration
OEM	Original Equipment Manufacturer
PIV	Particle Image Velocimetry
RF	Right Front
SIL	Sound Intensity Level
SP	Sound Pressure
SPL	Sound Pressure Level
TE	Trailing Edge
TEB	Trailing Edge Blowing
Upr	Upper
URANS	Unsteady Reynolds Averaged Navier-Stokes
VG	Vortex Generator

Contents

1 INTRODUCTION

1.1 Automotive Aeroacoustics

Aeroacoustic noise reduction is one of the growing concerns in the automotive industry. With the advention of hybrid and electric vehicles and advances in the suppression of tire airborne noise driven by legal requirements, aerodynamic noise (also known as "wind noise") is becoming a dominant contributor to the vehicle interior noise at high cruising speeds. An analogy with the aeronautical industry can be made. For example, while jet noise was the dominant source in the period of turbojet engines, airframe noise was of secondary importance. In the 1970s, with the introduction of turbofan engines with larger bypass ratios, the aeroacoustic noise generated by the interaction of unsteady flows with the airframe has gained importance, in special during landing conditions when landing gears and high-lift devices are deployed. Moreover, with the proliferation of autonomous driving, vehicle occupants will be more sensitive to cabin noise, and aeroacoustic noise is expected to become more prominent in customer surveys (Oettle and Sims-Williams (2017), Terakado *et. al* (2017)).

Automakers are investing a reasonable amount of resources to investigate noise mechanisms and mitigate them in order to meet aggressive comfort requirements. The most severe aeroacoustic noise phenomena in ground vehicles are those with a tonal nature[1] in addition to the broadband[2] contribution. The presence of discrete tones during vehicle operation is unacceptable, and one of the most critical components in terms of noise performance are the roof-mounted luggage carriers, which typically have a leading crossbar with direct exposure to the airflow. The noise generated from roof bars, when uncontrolled, can be very annoying to the customer.

[1] According to ISO 1996-2:2017, the definition of a spectral tone is that when a specific frequency band is higher than its direct neighbors by an amount dependent upon frequency. Tonal noise is commonly referred to as discrete or narrowband frequency noise, and is characterized by wave forms that occur at a center single frequency. The fundamental tone may also manifest itself at progressively lower intensity levels at integer harmonic multiples.

[2] Noise at a wide mixture of frequencies. Most industrial noise consists of broadband noise. If the noise has frequencies evenly distributed throughout the audible range, it is known as white noise and sounds like rushing water.

1.2 Aeroacoustics of Roof Crossbars

Roof-mounted luggage carrier crossbars have become a very popular feature of ground vehicles as the global market demand for small, mid and full-size Sport Utility Vehicles (SUV) and Crossovers has increased drastically over the years. Automakers are offering roof racks as a standard content rather than optional in several models. In parallel, accessory roof carriers are increasingly popular as they are used for holding sports gear and many other types of load. Figure 1.1 shows several roof rack system designs from different manufacturers. The racks are composed basically of a crossbar supported by longitudinal side rails and stanchions mechanisms.

From the wide range of vehicle's exterior parts that generate airflow noise, e.g. outside mirrors, A-pillars, roof antennas and windscreen wipers, roof racks are the most critical in terms of aeroacoustic performance. The noise contribution of a roof rack is both tonal and broadband in nature. The characteristic aeolian tone, when uncontrolled, is capable to reduce cabin intelligibility drastically in cruising speeds, causing annoyance to the vehicle occupants. The aeolian tone is described as a low frequency "howl" and invariably leads to customer complaints if not mitigated. The broadband noise is less intense and less severe to customer perception, but also requires attention during development.

Figure 1.1: Typical crossbar, stanchions and side rail system.

Figure 1.2 shows the uncontrolled noise contribution of a typical elliptical shape crossbar (no aeroacoustic solutions applied), measured on-track at 120km/h (actual vehicle and wind speed) with interior and exterior microphones. Acoustic pressure values are omitted due to confidentiality, as for this entire dissertation. The interior microphone is installed inside the vehicle cabin at the passenger's ear position. The exterior microphone is located 150mm above the crossbar, perpendicular to the radiated noise. The experiment will be further described in the section Experimental Method of this dissertation.

The incremental noise from the crossbar is within the wide frequency range from 0.1 to 3kHz, as it was measured by the exterior microphone. At those frequencies, the intelligibility inside the vehicle cabins is highly impacted. The incremental amplitude is

in the order of 15 dB at the 700Hz frequency band. Most of the noise is either reflected or attenuated in the path (roof panel, roof liners and glazed surfaces), so that at the receiver position (interior microphone), the noise increment concentrates at the regions of 200Hz and 0.5 to 1kHz. Even with the attenuation and reflection along the path, the increment at the passenger's ear location is approximately 5 dB at 600Hz, which demonstrates the severity of the phenomenon.

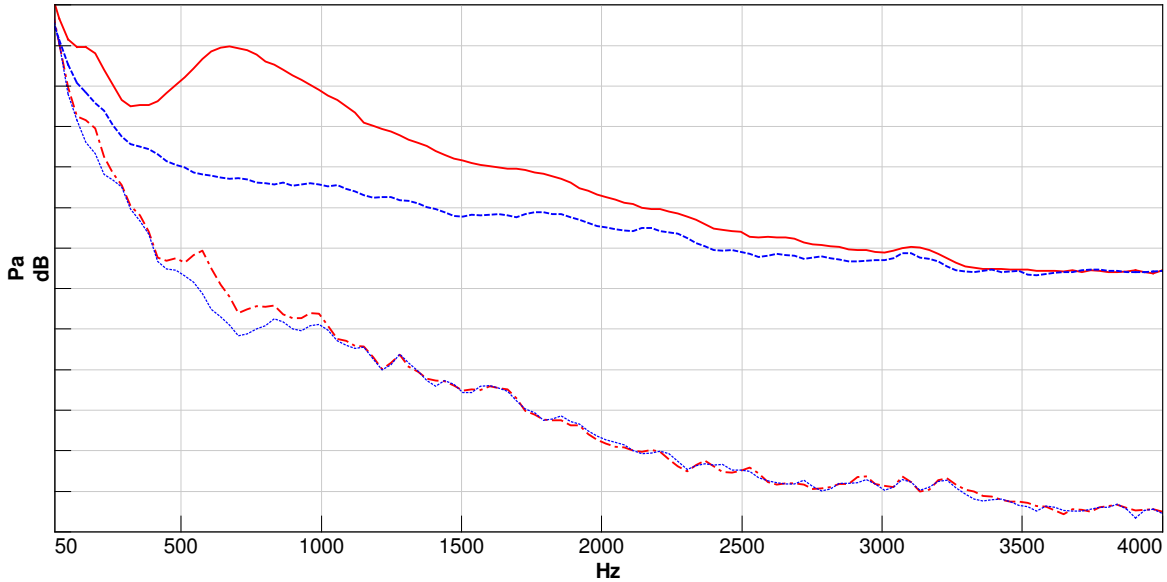

Figure 1.2: Noise spectra of a crossbar with uncontrolled noise.
SPL [Grid = 5 dB]. Frequency range: 0.05 – 4kHz. Wind speed: 120km/h.
Interior SPL: ··· No bar, —· Elliptical shape crossbar.
Exterior SPL: --- No bar, — Elliptical shape crossbar.

The aeolian tone is usually attributed to the crossbar shape, as a result of the direct exposure of the crossbar to the exterior airflow. Isolated component tests over many types of roof racks have proven that the aeolian tone is generated by the interaction of the crossbar with the air stream, whilst the longitudinal side rails and stanchion mechanisms contribute to the broadband noise generated by the roof rack system.

The leading crossbar is typically the most severe in terms of noise generation once the trailing crossbar is immersed either in the turbulent wake of the leading crossbar or the boundary layer developed along the vehicle roof. Side rails and stanchion mechanisms can eventually generate discrete high frequency tones known as "whistles", but the main contributor to the roof rack system tonal noise is beyond question the crossbar. Kingan and Pearse (2006) describe other noise sources involved in roof rack systems such as edge tones and wake-roof interaction, but also defines the crossbar self-noise as the primary noise source in the system.

1.3 Human Perception & Acoustic Requirements

Due to the anatomy of hearing organs, humans with average hearing acuity can hear pure tones from 0.02 up to 20kHz depending on the amplitude (Kuttruff (2004), Everest (2001)). The average thresholds of hearing and pain (when ear damage initiates) are shown in Figure 1.3. The region between the upper and lower thresholds is called the Auditory Area[3]. The frequency-level map shows that a normally hearing person is more sensitive to noise within the frequency range from 0.2 to 5kHz, with the highest sensitiveness at the 2 to 5kHz region (Brüel&Kjaer (1984)). The image also shows the typical area where speech occurs. In the automotive industry and many other industrial applications, standardized A-Weighting curve (Kuttruff (2004), Everest (2001)) is commonly applied to the metrics to compensate for this difference in ear's response. The A-Weighting adjusts the raw signal frequency domain spectra to approximate human hearing sensitivity, however, for investigative studies, in special those focused on the characterization of aeroacoustic noise sources, it is not recommended to modify any part of the original spectra, so no weighting (linear weighting) is applied in this study.

In a modern vehicle driving in cruising speeds, most of the aeroacoustic noise starts at frequencies as low as 20Hz, up to frequencies as high as 10kHz, caused by a wide range of flow phenomena such as turbulent boundary layers, separated and reattaching flows, a variety of types of cavity flows, vortex shedding and aspiration (air leakage) flows (Wang (2010)). Those phenomena are caused by the interaction of the exterior airflow with the vehicle components and design features such as A-pillars, outside mirrors, windscreen wipers, underbody parts, surface cavities and protrusions, radio antenna, roof crossbars and others (Oettle and Sims-Williams (2017)). The generated noise is transmitted into the passenger cabin through glazed surfaces, door-body weatherstrips and sheetmetal panels. Roof crossbars are critical in terms of wind noise performance once they are capable of generating dipole sources (which have a tonal nature), as well as broadband noise from quadrupole sources originated by its shear layers and free turbulence. The tonal noise is typically centered at frequencies from 0.1 to 1kHz depending on the shape parameters of the crossbar and the vehicle speed, and the broadband noise is typically observed within the wide range from 0.5 up to 5kHz. The amplitudes vary depending intrinsically on the vehicle speed and on the crossbar and vehicle designs, i.e. the characteristics of the source and the transmission paths. As a consequence, considering that normal human speech occurs within the 0.2 and 5kHz frequency range (Figure 1.3), roof crossbars directly affect the passengers' intelligibility in the vehicle cabin. In subjective evaluations, crossbar noise is easily noticed and complained by untrained evaluators, demonstrating

[3]The responsiveness of human hearing given by the Auditory Area changes with age.

the importance of addressing crossbar noise issues. As mentioned in Section 1.1, with the advention of electric vehicles and autonomous driving, the perception to crossbar noise will be imminently higher in forthcoming years.

A common psychoacoustics metric used to quantify the sound quality and communication ability of a noisy ambient is the Articulation Index (AI). It was originated in the field of communications and now is widely used in the automotive industry. AI measures the speech intelligibility of an acoustical environment and is rated from 0 to 100%. The higher the rate, the higher the intelligibility of words and sentences understood. Typically, an AI lower than 30% indicates unintelligible speech, and over 70% excellent intelligibility. The procedure to calculate the AI considers frequencies from 0.2 to 6.3kHz (Onusic *et. al* (2000), Oettle and Sims-Williams (2017)). Therefore, the noise emitted by roof crossbars greatly affects cabin Articulation Index and requires design optimization to lead to satisfactory AI rates and to an acoustically comfortable environment. Table 1.1 shows the calculated AI at the vehicle cabin for the conditions of background noise (no bar) and with the elliptical cylinder bar with uncontrolled noise. The crossbar reduces the AI by 3.3, 4.1 and 5.3%, respectively for the speeds of 80, 100 and 120km/h.

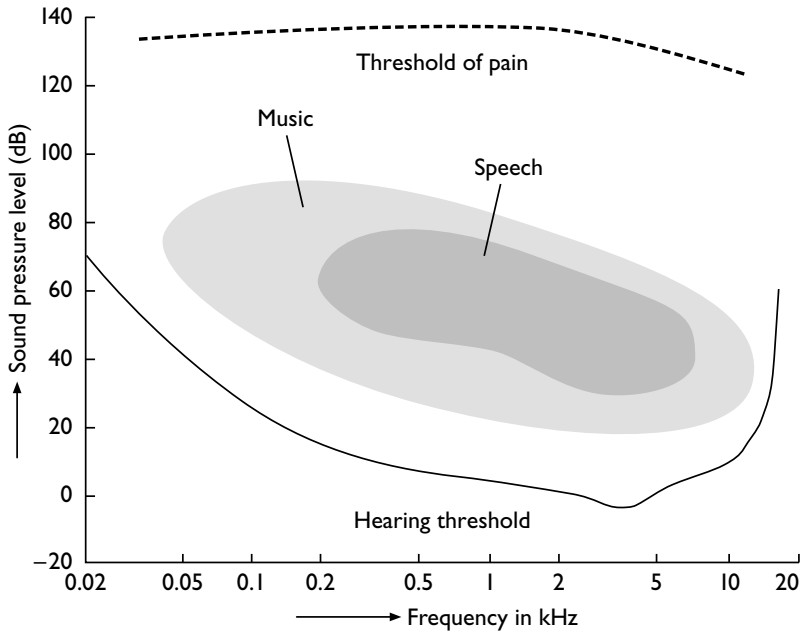

Figure 1.3: Thresholds of audibility and pain, adapted from Kuttruff (2004).

Articulation Index (AI), %			
Wind speed	80km/h	100km/h	120km/h
No bar	82.2	69.7	58.1
With crossbar	78.9	65.6	52.8

Table 1.1: Articulation Index (AI) for the conditions of Figure 1.2.

In the aeroacoustic development of a roof crossbar, the engineering objective can be defined in two requirements:

- Total elimination or suppression of the aeolian tone to an unnoticed level for all vehicle occupants. Tonal noise sources are more annoying than broadband sources of the same level since the sound of pure tones are prominent and easily perceived by the human ear, so they must be completely eliminated at the receiver. This requirement is intrinsically associated to the characteristics of the source (crossbar design). Rarely the transmission paths (glazed windows, sheetmetal panels and door seals) will reduce the sound energy transmission of the strong dipole sound source on the vehicle roof.

- Unnoticed incremental broadband noise by all vehicle occupants. The broadband noise increment from a roof crossbar is inherent, and the engineering objective is to minimize it to unnoticed levels in the vehicle cabin. The broadband noise is associated to both source and path characteristics, the latter being of critical importance and vehicle-dependent. Broadband noise is also originated by the roof crossbar stanchion systems, which also require optimization.

In summary, the subjective rating of crossbar noise is highly decreased when there are prominent tones at the interior. The acoustic pressure inside the vehicle must present a smooth frequency domain spectra, free of incremental noise peaks. At this point, the use of A-weighting on the interior noise signals is acceptable once it represents human hearing sensitivity more precisely. As a typical automotive engineering requirement, the decremental Articulation Index rate, without and with a roof rack system, must be null.

1.4 Common Industry Practices

One of the challenges involved in mitigating roof rack noise lies in commercial aspects. Roof racks are commercialized in three different strategies. First, OEM Parts are originally designed by the Automaker in partnership with a Tier-1 Supplier and are commercialized in regular models as standard or optional content. Second, OEM Accessory parts are also designed by the Automaker but are commercialized by the Dealers as accessories for specific models. Original OEM roof rack systems from these two categories are subjected to the engineering requirements of the Automaker. Third, Aftersales parts are designed by random suppliers for random vehicle models. In this category, the performance requirements are not controlled by the Automakers, and the components are not designed for specific vehicle models. In consequence, Aftersales accessory systems have higher

risk of presenting unsatisfactory noise performance than original Automaker components, although there exist independent roof rack manufacturers that offer systems with great aeroacoustic noise performance in the market. Some of them sell the aeroacoustic solutions separately as exclusive features, and some sell generic aeroacoustic solutions to any type of crossbar. The range of different roof rack systems, manufacturers, and consequently levels of performance, is countless.

Nowadays, most of the applied solutions to the aeolian tones were designed with a high level of empiricism. The design of a roof bar involves a number of criteria such as appearance, packaging, structural stiffness, aerodynamic drag and manufacturing requirements. The crossbar sections are typically not chosen for their aeroacoustic performance and the solution to the aeolian tone is typically applied experimentally after the basic cross-sectional shape dimensions are defined. In some cases, the solution is the addition of features or extra parts, which end up increasing part complexity, tooling and piece cost, as well as potentially jeopardizing style, aerodynamics and broadband noise performance. One of the rationale behind that is that accurate Computational Aeroacoustics (CAA) predictions are difficult and time-consuming due to the complicated three-dimensional flow physics that occur in the near wake. Therefore, not all manufactures and accessory suppliers are capable to predict early in the development process whether a conceptual bar shape will generate an audible discrete tone and address it in advance, during the early geometric release phases. Despite the fact that the aeolian tone is a severe phenomenon that affects the component design, its noise generation mechanisms, including the control and mitigation, are not fully understood, and the solutions are typically developed empirically during full-scale clay model and integration vehicle wind tunnel testing, when most of the design boundaries are constrained.

Figure 1.4 illustrates three cases of commercial crossbar profiles with advertised aeroacoustic solutions. Manufacturer I adopts the two-dimensional Boundary Layer Tripping (BLT) technique by inserting a rubber strip into the upper leading edge of the extruded profile. In its advertisement, the manufacturer claims "The Wind Barrier creates small swirls, forming an air cushion on the surface of the cross bar which acts as a bridge for the airstream above the T-Slot, preventing the development of noise under all driving conditions[4]". Manufacturer II also adopts the 2D BLT technique on the upper leading edge of the profile. It claims that the crossbar was optimized in the Wind Tunnel and has "drag and noise reduced to nearly zero[5]". The tapered and sharp trailing edge also plays an important role in reducing noise, as it will be discussed in section 3.3.1. Another common solution applied in the automotive industry is the installment of a

[4] http://www.atera.de/en/signo-rt-rail-roof-bars.html
[5] http://www.whispbar.com/about/technology/

rubber insert on the upper surface of the crossbar similar to a serration trip. The insert has tipped vanes that change local airflow direction and promote instantaneous boundary layer transition. Manufacturer III claims the "Wind Diffuser™ technology disturbs the airflow to reduce noise and drag[6]". These and other solutions are further discussed in section 4.1.3. Three commercial profiles were also tested and the results are discussed. Notwithstanding, plenty of other aerodynamic and aeroacoustic solutions exist worldwide.

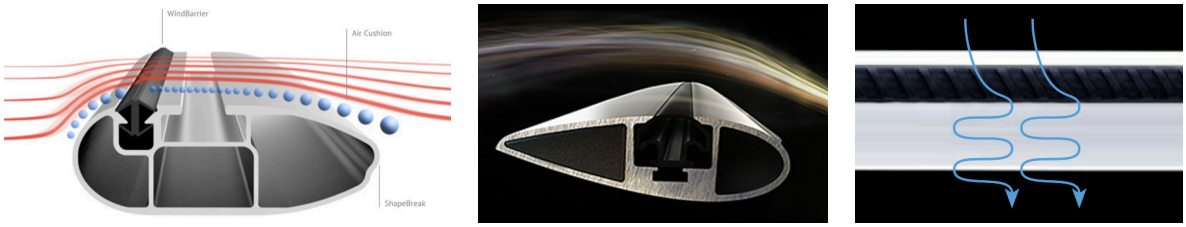

(a) Manufacturer I. (b) Manufacturer II. (c) Manufacturer III.

Figure 1.4: Commercial crossbars advertised solutions.

1.5 Noise Generation Mechanisms

1.5.1 Fundamentals of Aeroacoustics

Aeroacoustics is a field in the acoustic science which studies the noise generated by the airflow and by the interaction of aerodynamic fluctuations in the presence or not of rigid surfaces, and is commonly referred to as aerodynamic noise. Aeroacoustics is a relatively new field of study, being born in the 1950's essentially to understand the generation of jet noise (Lighthill (1952)). Currently, it is a growing field of study due to stringent modern aviation noise regulations and the advention of electric vehicles in the automotive industry. Moreover, aeroacoustics has important applications in wind energy since the wind farms are becoming closer to residential areas and leading- and trailing-edge noise is a relevant source of aeroacoustic noise in wind turbines. Aeroacoustics also finds application in military aircraft and helicopters, high-speed trains, musical instruments and house appliances, such as vacuum cleaners. In rocket engines, aeroacoustic fluctuations are limiting factors in the design. All these scientific and technological applications are pushing the limits of comprehension of aerodynamic noise generation and driving the development of experimental and numerical methods to measure, model, control and mitigate the aeroacoustic sources existing today.

[6] https://www.thule.com/en-gb/gb/roof-rack/roof-bars/thule-wingbar-960-_-960100

1.5.1.1 Aeroacoustic Sources

A direct method to calculate aerodynamic noise is to solve the Navier-Stokes equations in a three-dimensional unsteady and compressible flow. However, this is not feasible except for very simple cases. In order to overcome that, in several studies (Lighthill (1952); Ffowcs Williams and Hawkings (1969)), the Navier-Stokes equations were rewritten as non-homogeneous wave equations, a procedure that originated the Acoustic Analogies, which modify the full equations of fluid dynamics in an equivalent wave equation. The equations governing the flow-generated acoustic field are rearranged in such a way that the wave operator is at one side and the non-linear source mechanisms responsible for the noise generation on the other side. Approximations are introduced to make the source terms independent of the acoustic variables. In this way, linearized equations describe the propagation of the acoustic waves in a homogeneous stationary medium excited by the acoustic source terms, which are determined from the turbulent perturbations.

Common to all Acoustic Analogies are the fundamental aeroacoustic source terms. They consist of pressure fluctuations originated by turbulent perturbations that excite the acoustic medium with different directivity patterns. The terms are present in the wave equations of each Acoustic Analogy formulation, and can be separated in three distinct categories (Figure 1.5):

- A Monopole source (Figure 1.5a) generates omni-direction spherical waves. It can be considered as a small pulsating sphere, contracting and expanding with time. The fluctuating pressure amplitude p' is a function of the radial distance from the source r ($p' = f(r)$). The intensity of the Monopole source is proportional to the Mach number ($I \sim \frac{\varrho}{c} u^4 = \rho u^3 M$), and is the most efficient noise propagation source. In automotive aeroacoustics, the occurrence of Monopole aeroacoustic sources is rare. It can be originated from unsteady volumetric flow addition, such as leaks in the sealing of doors, or unsteady addition of fluid volume to the passenger compartment through leak paths. Following the ideas from Ffowcs Williams and Hawkings (1969), a distribution of Monopoles in its differential form is given by Equation 1.1. Q_i gives rise to a Monopole-type contribution that can be thought of as an unsteady mass addition. The function $f = 0$ defines the surface outside of which the solution is desired. The total density and pressure are given by ρ and p respectively. The fluid velocities are u_i, while v_i represents the velocities of the surface f. Perturbation quantities relative to the free-stream conditions are denoted by the subscript 0. The Cartesian coordinates and time are x_i and t respectively. The term $\delta(f)$ is the Dirac delta function, which is zero for $f \neq 0$, and yields a finite value when

integrated over a region including $f = 0$.

$$\frac{\partial}{\partial t}(Q\delta(f)), \tag{1.1}$$

where

$$Q_i = (p_0 v_i + \rho(u_i - v_i))\frac{\partial f}{\partial x_i}. \tag{1.2}$$

- A Dipole source (Figure 1.5b), contrary to the Monopole, has two magnitude components, the near and far-field terms. Moreover, it is directional in the sense that the radiation has a component which depends on the angle of the dipole axis. It can be considered as two adjacent Monopole sources of the same magnitude oscillating out of phase. The fluctuating pressure amplitude is a function of the the radial distance and angle (θ) from the source ($p' = f(r, \theta)$). The intensity of the Dipole source is proportional to the third power of the Mach number ($I \sim \frac{\rho}{c^3}u^6 = \rho u^3 M^3$) and, for low Mach numbers, such as in automotive aeroacoustics ($M < 0.3$), it is less effective than the Monopole source. The noise from a turbulent flow over a small obstruction in an airstream, and the interaction of unsteady pressures upon a rigid surface (such as it occurs in a roof rack crossbar), provide good examples of fluid mechanical Dipole sources of aerodynamic noise. Compact bodies radiate a Dipole sound field associated with the unsteady forces which they exert on the flow as a reaction to the hydrodynamic forces of the flow applied to them. A distribution of Dipoles is given by Equation 1.3. Again, following the ideas of Ffowcs Williams and Hawkings (1969), F_i involves unsteady forces due to surface pressure and stress fluctuations originated by the interaction of the flow with the moving bodies as

$$-\frac{\partial}{\partial x_i}(F_i\delta(f)), \tag{1.3}$$

where

$$F_i = (P_{ij} + \rho u_i(u_j - v_j))\frac{\partial f}{\partial x_i}. \tag{1.4}$$

- A Quadrupole source (Figure 1.5c), similarly to the Dipole, presents an acoustic pressure which depends on a near and far-field terms and that has a directional component ($p' = f(r, \theta)$). A Quadrupole source can be considered as four Monopoles (or two Dipoles) which would model the noise generated by stresses of fluid elements. As fluid can be expected to support such stresses poorly and Quadrupole sources are less efficient radiators of noise. The far-field intensity of the Quadrupole source is proportional to the eighth power of the Mach number ($I \sim \frac{\rho}{c^5}u^8 = \rho u^3 M^5$), and it is less effective than the Dipole sources in road vehicle applications for low Mach

numbers ($M < 0.3$). In road vehicle aeroacoustics, Quadrupole sources are often neglected. In the absence of leak noise, Dipole sources tend to dominate the overall cabin noise of a road vehicle. A volumetric distribution of Quadrupoles in the outer region of the surfaces due to the turbulent flow is given by Equation 1.5, where T_{ij} is the Lighthill stress tensor. The Kronecker delta, δ_{ij}, is unity for $i = j$ and zero otherwise.

$$\frac{\partial^2}{\partial x_i \partial x_j}(T_{ij}H(f)), \tag{1.5}$$

where

$$T_{ij} = \rho u_i u_j + P_{ij} - c_0^2 \rho' \delta_{ij}. \tag{1.6}$$

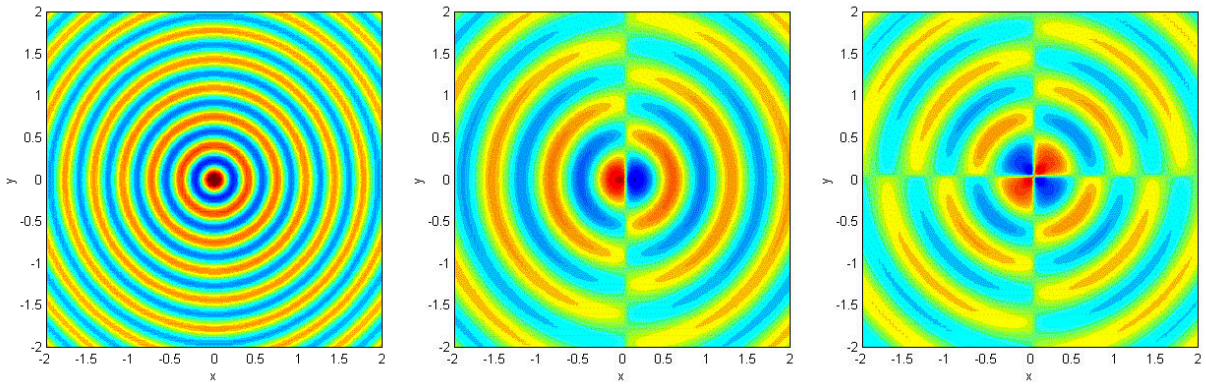

(a) Monopole. (b) Dipole. (c) Quadrupole.

Figure 1.5: Aeroacoustic sources cartesian directivity fields.

1.5.1.2 Acoustic Analogy

The application of different simplifications to the Navier-Stokes equations has led to the formulation of different Acoustic Analogy equations. The most used Acoustic Analogies are Lighthill's Analogy and its extensions made by Curle and Ffowcs Williams & Hawkings. Those Analogies can be used in a wide range of applications, and are typically used in Computational Aeroacoustics (Hirschberg and Rienstra (2004)).

Lighthill's Acoustic Analogy (Lighthill (1952)) was originally developed for unbounded flows, such as jet flows in aviation engines. It assumes the fluid is ideal (no viscous or thermal effects), and that outside of the source region, there is no flow. Refraction effects are not included in the wave operator. Lighthill's stress tensor, which forms the source part of the analogy, is represented by a distribution of Quadrupole sources. Its most important component for turbulent flows in absence of temperature fluctuations is that of the Reynolds' stresses, which implicates that the spatial turbulent velocity fluctuations are the main source of the flow-generated sound. The Lighthill Acoustic Analogy is written

in differential form as Equation 1.7. T_{ij} is the Lighthill stress tensor given by Equation 1.6. In Lighthill's equation, no Monopole or Dipole source terms are present.

$$\left(\frac{\partial^2}{\partial t^2} - c_0^2 \frac{\partial^2}{\partial x_i \partial x_j}\right)\rho' = \frac{\partial^2}{\partial x_i \partial x_j} T_{ij}. \tag{1.7}$$

Ffowcs Williams & Hawkings Acoustic Analogy (FW-H, Ffowcs Williams and Hawkings (1969)) is an extension of Lighthill's Acoustic Analogy, based on the same starting point but taking into account the effects of moving boundaries. The aim is to handle solid surface interactions that are directly involved in the generation of flow-generated sound. The normal component of the surface velocity forms the equivalent surface Monopole source distribution and the sound pressure at the boundary forms the equivalent surface Dipole source distribution. The calculation also involves Quadrupole terms. The Ffowcs Williams–Hawkings Acoustic Analogy is used in many technical applications, e.g. aircraft airframe and fan engine noise, automotive aeroacoustics, helicopter rotors, marine propellers, compressors and turbines noise. The FW-H equation can be written in differential form as

$$\left(\frac{\partial^2}{\partial t^2} - c_0^2 \frac{\partial^2}{\partial x_i \partial x_j}\right)(H(f)\rho') = \frac{\partial^2}{\partial x_i \partial x_j}(T_{ij}H(f)) - \frac{\partial}{\partial x_i}(F_i \delta(f)) + \frac{\partial}{\partial t}(Q\delta(f)). \tag{1.8}$$

The Monopole-type contribution Q_i is given by Equation 1.2, the Dipole term F_i is given by Equation 1.4 and the Lighthill stress tensor of Quadrupoles T_{ij} is given by Equation 1.6. The usual convention involves a quiescent ambient state with f prescribed as a function of time so that it always surrounds a moving source region of interest. $H(f)$ is the Heaviside function which is equivalent to one for $f > 0$ and zero for $f < 0$. The derivative of the Heaviside function $H'(f) = \delta(f)$ is the Dirac delta function, which is zero for $f \neq 0$, but yields a finite value when integrated over a region including $f = 0$ (Lockard (2000)).

Curle's Acoustic Analogy (Curle (1955)) is obtained from the Ffowcs Williams & Hawkings Acoustic Analogy but assuming the boundaries are stationary. In this case, only the equivalent surface Dipole source distribution is present to take into account the sound scattering on the surface.

1.5.2 Aeroacoustics of Cylinders and Aerodynamic Profiles

In a circular cylinder, the aeolian tone is caused by the periodic shedding of vortices on the trailing edge of the cylinder immersed in the airflow. The boundary layers formed at the leading edge of the cylinder separate in the rear portion near the top and bottom of the

cylinder and form shear layers with periodic oscillations that grow behind the cylinder and form the von Karman vortex wake (Figure 1.6). The oscillating structures cause pressure fluctuations which scatter along the solid surface and create a source of sound that propagates as a Dipole, i.e., the aeolian tone (Doolan (2009)). For Reynolds numbers above 80,000, typical of roof bar applications, the turbulent wake has the fundamental mechanics of the von Karman vortex wake, added to three dimensional turbulent velocity fluctuations of several different scales (wavelengths). These three-dimensional pressure perturbations also meet the rear cylinder wall and generate a broadband effect of the aeolian tone and its harmonics (Doolan (2009)). The fundamental frequency of the tone (f_0) emitted by a circular cylinder is given by the fundamental Strouhal number $St_0 \approx 0.2$ (Strouhal (1878)), where $f_0 = \frac{St_0 U_0}{D}$. D is the cylinder diameter and U_0 the free stream velocity. The frequency of the tone increases with the velocity of the airflow and decreases with the increase of cylinder diameter.

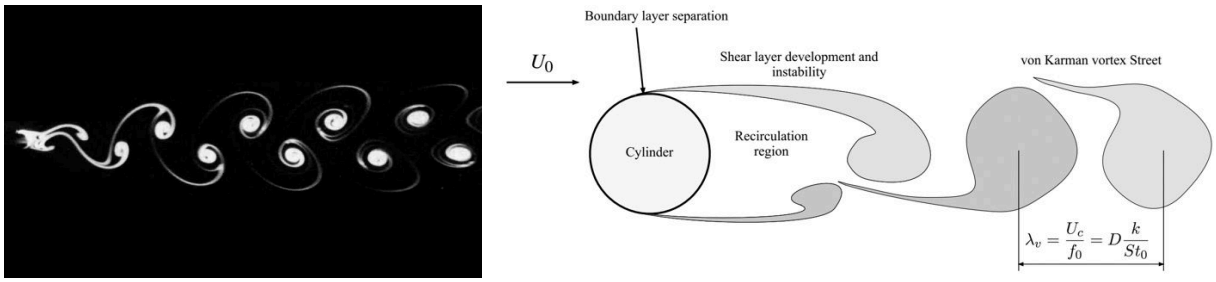

(a) Kárman vortex wake. (b) Noise mechanism.

Figure 1.6: Noise generation mechanism of a circular cylinder (adapted from Van Dyke (1982) and Doolan (2009)).

In an airfoil, the aeroacoustic phenomenon is more complex. There are five known self-noise noise generation mechanisms involved in subsonic flow conditions: laminar boundary layer vortex shedding noise (low Reynolds number flows); turbulent boundary layer trailing edge noise (high Reynolds numbers flows); trailing edge bluntness vortex shedding noise; boundary layer separation and stall noise; and tip vortex formation noise (Brooks *et. al* (1989)). In automotive roof bar applications, tip vortex noise and deep stall noise do not occur. The other mechanisms, also referred to as trailing edge noise or boundary-layer instability noise, occur and generate both the broadband and tonal components of the noise.

At low Reynolds numbers, the flow over airfoils has different characteristics from that found at high Reynolds numbers. At $Re_c = 50,000$ and 0° Angle of Attack (Sandberg *et. al* (2008)), laminar boundary layers form initially on the airfoil leading edge, but differently from the circular cylinder, unsteady disturbances appear as Tollmein Schlicting or T-S waves. These are the first stages of the boundary layer transition to a turbulent state and, depending on the flow regime, they can separate and create oscillating

shear layers that interact with the trailing edge, developing a complex wake behavior and noise generation mechanism which further involves diffraction and scattering of the acoustic waves. Different from the circular cylinder Dipole radiation, the directivity of the acoustic waves presents a cardioid pattern whose mechanism is remarkably described by (Arcondoulis *et. al* (2011)): the noise sources within the boundary layer are represented by Quadrupoles that are responsible for an incident acoustic field. When an incident wave encounters the airfoil trailing edge, a scattered wave is produced and travels upstream the airfoil. This scattered wave is represented by a combination of dipole sources along the airfoil surface. However, since the airfoil behaves as a non-compact surface for high frequencies, it radiates as a more efficient cardioid directivity with acoustic intensity proportional to Mach number to the fifth power, differently than that of the compact dipole (Ffowcs Williams and Hall (1970)) (Figure 1.7).

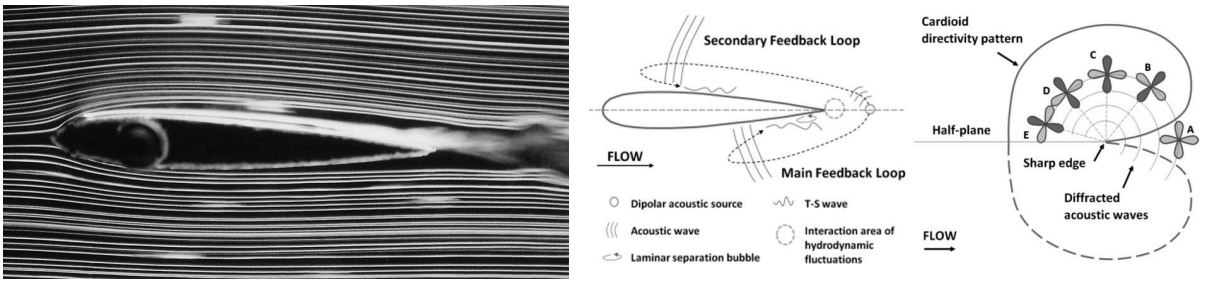

(a) NACA 0012 near wake at $Re_c = 48,000$. (b) NACA 0012 Noise mechanism (feedback loop).

Figure 1.7: Noise generation mechanism of a NACA 0012 wing section (adapted from Kim *et. al* (2011) and Arcondoulis *et. al* (2011)).

The generated airfoil noise is classified either as tonal or broadband, and in certain cases, at low to moderate Reynolds numbers of interest to the automotive industry, it contains a superposition of primary ($f_{n,max}$) and secondary (f_n) narrowband tones on a broadband hump (Arbey and Bataille (1983)). Broadband noise is due to a large number of incoherent eddies with a variety of scales and strengths, and the discrete tones are due to reasonably coherent eddies advected past the trailing edge. The discrete tones measured experimentally for the NACA0012 profile can be described in a ladder-like structure plot in function of the airstream velocity, and the primary tone is fitted by the curve $f_{n,max} = 0.011 U_0^{1.5}/\sqrt{C\nu}$, where C is the airfoil chord length and ν is the kinematic fluid viscosity (Arbey and Bataille (1983)). The main frequency has a Strouhal number and airfoil thickness dependence.

There is still no formal method for determining which Angle of Attack and Reynolds number causes the greatest tonal sound pressure level for an airfoil under low Reynolds number flow conditions, and there is no general consensus in the aeroacoustic community of the precise cause of trailing edge noise primary and secondary tones (Arcondoulis *et. al* (2011)). The strongest hypothesis is that at certain frequencies the sound is amplified via

an acoustic feedback mechanism near the trailing edge, but the physics of the feedback mechanism is still unclear. A summary of the various proposed causes for the tonal noise and the feedback mechanism is given by Arcondoulis *et. al* (2011). It is also known that depending on the Angle of Attack, airfoil geometry and the Reynolds number, discrete tones do not occur (Nash *et. al* (1999)). Ramirez and Wolf (2016) also demonstrated a direct relation of the trailing edge bluntness to the occurrence and characteristics of the narrowband tones.

In an elliptical cylinder, the aerodynamic characteristics are quite different from those of conventional airfoils. At low Reynolds numbers and zero Angle of Attack (Figure 1.8a), the coherent von Karman vortex wake initiates after the shear layers become unstable, similarly to a circular cylinder. The vortex initiation seems to occur later than in a circular cylinder, however, what may have a direct effect on the generate noise. Kwon and Park (2005) investigated the boundary layer velocity profiles and vortices structures behind the trailing edge of an elliptical profile of $AR = 0.16$ at zero Angle of Attack by Particle Image Velocimetry (PIV). At $Re_c = 300,000$ (Figure 1.8b), the boundary layer on both sides of the smooth surface separates early ahead of $x/c = 0.90$ forming a reversed flow region with parallel vortices just after the trailing edge. The far wake is not covered in the PIV domain, but apparently the flow reattaches and the Von Karman vortices do not occur. Those observations suggest the noise generated by an elliptical cylinder is strictly dependent on the Reynolds number. Few to none experimental data on the noise generated by elliptical cylinders is available in the literature. Iglesias *et. al* (2016) have studied the tonal noise amplitude, frequency and relative bandwidth generated by elliptical cylinders of different aspect ratios. They identified that the increase of the elliptical cylinder chord (and consequently reduction of the aspect ratio) causes a slight increase in Strouhal number (St), and that St and the relative bandwidth of the main shedding vortex frequency (main tone) are strictly dependent on the flow speed (Re_c).

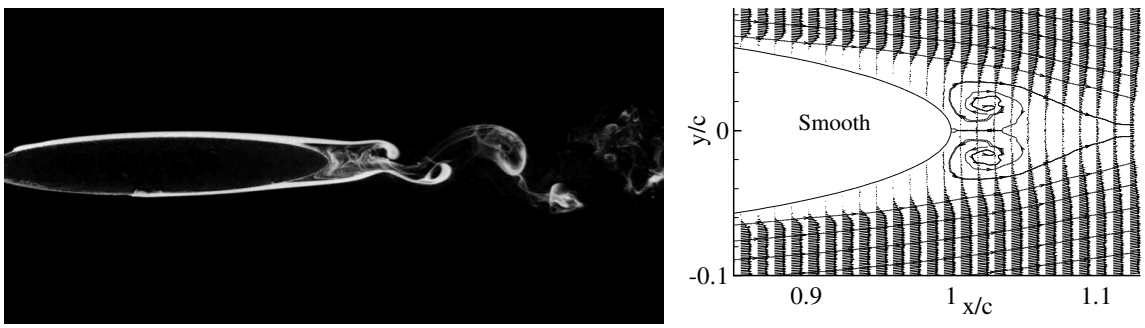

(a) $Re_c = 4,000$. (b) $Re_c = 300,000$.

Figure 1.8: Elliptical cylinder wake structure at $Re_c = 4,000$ (adapted from Van Dyke (1982) and Kwon and Park (2005)).

1.5.3 Principles of Automotive Crossbar Aeroacoustics

Several geometrical factors affect the aeroacoustic self-noise of a roof rack crossbar. The critical controlled factor is the crossbar shape: thickness, chord, Angle of Attack and profile (outline), including symmetry (Figure 1.9a). Other factors such as longitudinal position and height (related to the boundary layer formation on the vehicle roof), surface roughness and cross-car curvature are secondary factors, highly constrained and complex to control. The roof crossbar is immersed in an inherently unsteady ambient air, and is typically located outside of the roof boundary layer due to distance-to-roof package requirements. It is also assumed that the surface roughness is as smooth as it typically is in commercial roof bar materials (e.g. aluminum extrusions), giving focus on the bar shape parameters.

One of the difficulties to understand the fundamental noise mechanisms of a roof crossbar shape is the fact that commercial crossbar profiles are not as blunt as a cylinder, neither as thin as a wing section or a flat plate. The physics involved in both types of bodies is reasonably well understood, but the automotive roof bar elliptical shapes have the general fluid dynamic features "between" those conditions. In some cases, the profiles are basically airfoil sections with truncated trailing edges. Figure 1.9(b) shows four commercial extruded roof bar sections, two of them with package for the installation of rubber inserts. None of those is as blunt as a cylinder, neither as thin as a wing section. For these typical shapes, characteristic Reynolds numbers are low due to the small length scales (chord) and low wind speeds (typically, the flow conditions lead to $80,000 < Re_c < 300,000$), and the operational Mach number is very low (between 0.05 and 0.2). At these conditions, aerodynamic and aeroacoustic characteristics are fundamentally different from those seen in typical aerospace applications (Santhanakrishnan and Jacob (2005)).

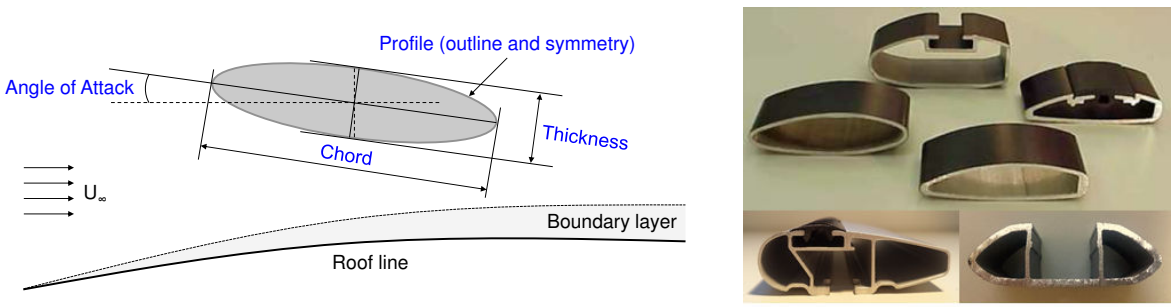

(a) Parameters affecting crossbar self-noise. (b) Commercial extruded profiles.

Figure 1.9: Controlled noise parameters and commercial Aluminum profiles.

1.6 Outline and Objectives

The noise emitted by elliptical shape automotive crossbars presents characteristics similar to those of both circular cylinders and airfoils in low Reynolds number regimes. A reasonable assumption is that, the higher the crossbar thickness ratio, the more it will approximate to the circular cylinder noise characteristics, but not much more than that is understood. In the applied literature, focus has been given on numerical methods[7] to predict tonal and broadband noise behavior from automotive crossbars (Lee *et. al* (2002), Karbon and Dietschi (2005), Jeong *et. al* (2007), Senthooran *et. al* (2007)), but few to none experimental studies with an investigative approach are available. The variety of different crossbar sections available in market also increases the challenge in understanding the noise generation physics involved. In addition, most of the *know-how* on noise control techniques is based on empirical assessments of corporate property.

Given this scenario, the major objective of this project is to contribute to the open understanding of the physics involved in this classic aeroacoustic problem of modern vehicles and support the development of the next generation of noise control techniques, as well as the development of numerical tools by providing experimental data from basic geometry cases. The project and its objectives are outlined in the following topics.

- **Chapter 2:** Establish a robust and reliable data acquisition method based on track testing. That was accomplished by correlating measured track data to wind tunnel measurements of the same vehicle and part configurations. Both Sound Pressure and Intensity Levels are compared and the measurement variation on-track is also assessed.

- **Chapter 3, Section 3.1:** Investigate the effects of the vehicle roof on the near-wake flow structure of the crossbar, and how it affects the generated noise in comparison to free-flow and free-sound field condition. That is performed by assessing reference bodies' measurements and local flow visualization.

- **Chapter 3, Section 3.2:** Compare the noise generated by an elliptical cylinder with that generated by a circular cylinder and a NACA 0012 airfoil with the same thicknesses and at the same operational conditions. The key objective is to understand whether the noise emitted by elliptical crossbar profiles have more similarities with a blunt or an aerodynamic profile.

[7] Computational Aeroacoustics methods are discussed in Appendix A.

- **Chapter 3, Sections 3.3 and 3.4:** Investigate the effects of changing the basic ellipse geometry parameters and Angle of Attack on the generated sound. Different leading and trailing edge combinations are tested using a clay-milled reference elliptical crossbar.

- **Chapter 4, Sections 4.1 and 4.1.3:** Investigate the effectiveness of common industry noise reduction practices based on passive Boundary Layer Tripping techniques (BLT), and perform a parametric study of different BLT types, locations and geometries in an elliptical crossbar shape. Two-dimensional outward and inward and three-dimensional tripping types of different configurations are also assessed.

- **Chapter 4, Sections 4.2 and 4.3:** Assess the noise reduction effectiveness of innovative noise solutions such as the application of perforations and active Trailing Edge Blowing (TEB) on the trailing edge of an elliptical crossbar. TEB was investigated at various blowing speeds relative to the vehicle speed by piping a fraction of the HVAC system airflow into the crossbar.

- **Appendixes A, B and C:** Bring an introductory overview of Computational Aeroacoustics methods; demonstrate the occurrence of discrete tones on the NACA 0012 profile; and revels the effects of different surface roughness on the aeroacoustic noise generated the elliptical shape crossbar.

2 EXPERIMENTAL METHOD

In the current project, acoustic measurements are performed using the experimental methodology described in this chapter. Test track, tools, parts, vehicle and data acquisition equipment are employed in the experimental framework. The uncontrolled ambient condition on-track, however, poses a challenge for the present analysis. Shift-to-shift and run-to-run variations of ambient conditions and transient wind gusts can harm data and lead to incorrect conclusions. In order to understand how accurate it would be to measure aeroacoustic noise on-track, a correlation study between track and wind tunnel data was performed first. Track tests were performed at the straightaway track of General Motors South America Cruz Alta Proving Ground (CAPG, Figure 2.1a). Wind tunnel tests were performed in the Aeroacoustic Wind Tunnel of General Motors North America (GMAL, 2.1b). The following sections will describe both test facilities and the adopted acquisition setup.

(a) CAPG Test track.

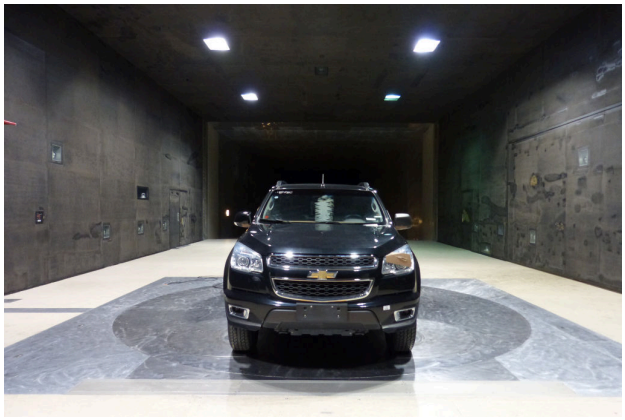

(b) GMAL Wind Tunnel.

Figure 2.1: Experimental method correlation study.

2.1 On-Track Testing

On-track tests were performed at the smooth asphalt straightaway track of the CAPG (Figure 2.1a), located in the city of Indaiatuba, SP, Brazil. The track has two straight flat sections of 2.5km each, interconnected by 180° tilted turns. Data acquisition was taken uniquely at the track sections with less exposure to crosswind. In order to reduce run-to-run variations, measurements were triggered at the same point for each test speed. Ambient conditions were monitored during the test to avoid wind speeds above 3m/s and

high temperature gradients. Each series of acquisition did not last longer than 2 hours to avoid drastic ambient condition changes within a single test shift. In order to minimize powertrain airborne noise, the lowest gear ratio available and cruise control were used to maintain low and stable engine rotational speed.

The interior microphones were installed using a supporting frame attached to the driver and passenger seat headrests (Figure 2.2a). For the exterior noise measurements, a 3-DOF supporting arm was developed in-house to accommodate both single (Figure 2.2b) and dual microphone probes with varying spacings (Figure 2.2c). The microphones were levered in x, y and z directions using a bubble level ruler, accounting for any static vehicle pitch and roll angles.

(a) Interior microphone. (b) Exterior microphone. (c) Exterior intensity probe.

Figure 2.2: Track data acquisition hardware.

2.2 Wind Tunnel Testing

Wind tunnel tests were executed at the General Motors Aerodynamics Laboratory (GMAL, Figure 2.1b), located at the General Motors Warren Technical Center in Michigan, United States. The facility is used for aerodynamics, cooling airflow and aeroacoustics investigations. The closed-jet test section is 5.5m high, 10.4m wide and 21.7m long, and is the largest wind tunnel in the world dedicated to automotive testing. The stationary floor test section is semi-anechoic and the 301m long air path is acoustically treated. The interior surface of the air path has acoustic absorption panels consisting of fiberglass batting behind perforated sheet metal panels, and turning vanes are acoustically treated to absorb background noise.

The interior microphones used a supporting frame positioned on the driver and passenger seat cushion (Figure 2.3a). For the exterior noise measurements, a 3-DOF supporting arm was used to install both single (Figure 2.3b) and dual microphone probes (Figure 2.3c). The microphones were levered in x, y and z axis using local flow visualization with tufts of yarn aided by cameras positioned at the side walls and roof of the test section.

(a) Interior microphone.

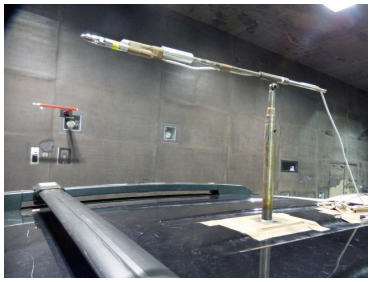

(b) Exterior microphone.

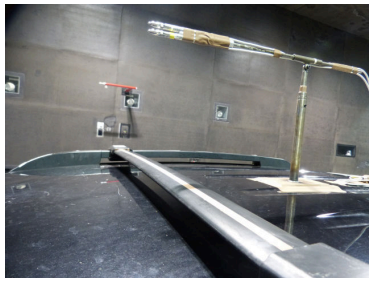

(c) Exterior intensity probe.

Figure 2.3: Wind Tunnel data acquisition hardware.

2.3 Data Acquisition & Signal Processing

The same vehicle and parts were tested in both wind tunnel and track using three different data acquisition setups:

- Interior Sound Pressure (INT-SPL)
- Exterior Sound Pressure (EXT-SPL)
- Exterior Sound Intensity (EXT-SIL)

2.3.1 Interior and Exterior Sound Pressure

For interior and exterior acoustic pressure measurements, Brüel & Kjaer 1/2" microphones type 4189-A-021 were used. The interior microphones were installed at seat headrests (receiver position, Figures 2.2a and 2.3a). The exterior microphones were located at vehicle centerline 300mm above the roof crossbar and perpendicular to the radiated noise (Figures 2.2b and 2.3b). The transducers were calibrated using the Brüel & Kjaer microphone calibrator type 4231.

For exterior measurements, Brüel & Kjaer nose cones type UA-0386 (Figure 2.4) were used to reduce the microphone aerodynamically self-induced noise. The cone has a streamlined shape with a highly polished surface in order to give the least possible resistance to air flow. A fine wire mesh around the nose cone permits sound pressure transmission to the microphone diaphragm while a truncated cone behind the mesh reduces the air volume in front of the diaphragm.

Figure 2.4: Brüel & Kjaer nose cones type UA-0386.

For interior and exterior sound pressure level measurements, channel A-weighting was applied, and the frequency resolution was set to a narrowband bandwidth of 32Hz. The frequency range covered the range from 160Hz to 16,384Hz on-track and from 160Hz to 13,248Hz at the wind tunnel (lower and upper cutoff frequencies), with linear averaging and 50% overlap. The gain of each channel was set to maximize signal but avoid overloads. The frequency domain spectral plots were calculated using a Fast Fourier Transform (FFT) analyzer (LMS TestLab®).

2.3.2 Exterior Sound Intensity

The advantage of measuring sound intensity instead of sound pressure is that intensity accounts for the acoustic power in a given direction in a free or partially diffuse sound field (case of this study), and a steady background noise makes no contribution to the magnitude measured. Because sound intensity gives a measure of direction as well as magnitude, it is very useful to characterize sources of sound, and its application to crossbar track testing is promising.

For acoustic intensity measurements, a parallel-aligned phase-matched microphone pair (intensity probe) was used. The probe was especially designed for sound intensity measurements and used B&K 1/2" microphones type 4189-A-021 and nose cones B&K UA-0386 (Figure 2.4). The transducers were calibrated using the Brüel & Kjaer microphone calibrator type 3541. The exterior intensity probe was located at the vehicle centerline 300mm above the roof crossbar and perpendicular to the radiated noise (same as for the Exterior SPL, Figures 2.2c and 2.3c). The microphone spacing direction is the same of the sound propagation (z).

In order to define the proper microphone spacing, the upper and lower frequency limits for different spacers were analyzed. The assumptions made in theory impose an upper frequency limit, i.e., the smaller the spacer, the higher the frequency that can be measured. On the other hand, phase mismatch in the analyzing system causes a low frequency limit, i.e., the larger the spacer, the lower the frequency limit. Considering a pressure-intensity index ($L_P - L_I$) of 3 dB (maximum) and a conservative phase mismatch in the analyzing system of $\pm 0.3°$ for Brüel & Kjaer instrumentation, the spacing selected was 16mm, which can cover the frequency range of interest from 0.1 to 3kHz (Sound Intensity Manual, Brüel & Kjaer). A 50mm spacer would measure from 63Hz but would be limited in high at 1.25kHz, while a 12mm spacer would measure up to 5kHz but would be limited in low at 250Hz.

The in-flow sound intensity I was calculated using the Two-Microphone Cross-Spectral Intensity Method (Chung and Blaser (1980)). The intensity is calculated by the FFT

based indirect method, i.e., from the imaginary part of the cross-power sound pressure spectrum between the two microphones:

$$I = -\frac{1}{\omega\rho\Delta r} Im(G_{12}), \tag{2.1}$$

where G_{12} is the cross spectra between the two microphones, ω is the angular frequency, ρ is the air density, and Δr is the spacing between the two microphones. The reference value for sound intensity level is one pico-Watt per square-metre ($10^{-12} W/m^2$).

To process the signal, no channel weighting was applied, and the frequency resolution was set to a narrowband bandwidth of 32Hz. The frequency range covered the same range from Section 2.3.1, with same averaging, overlap channel gain. The calculation is embedded into the Brüel & Kjaer Pulse LabShop®.

2.4 Track and Wind Tunnel Correlation

Three different design conditions were tested at the wind tunnel and track at 100km/h and 120km/h of actual wind speed, and the results were compared. Figure 2.5(a) represents the in-flow background noise condition, where no bar is installed on the roof. Figure 2.5(b) shows the condition where the elliptical cylinder crossbar is installed but no noise control is applied. Figure 2.5(c) shows the controlled noise condition (aeolian tone solution in place).

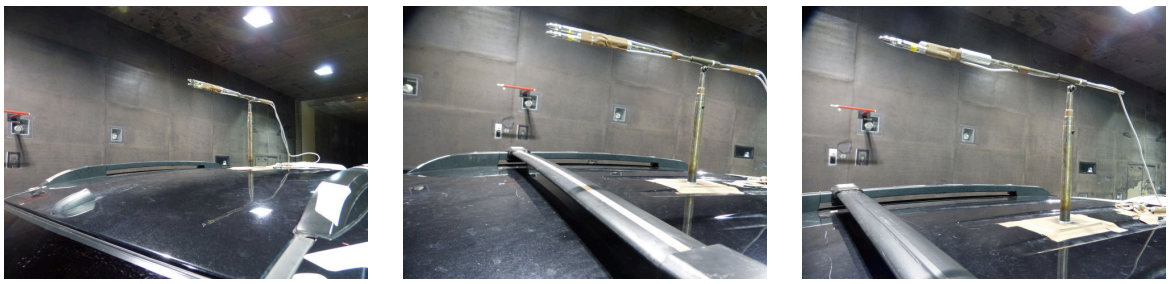

(a) No-bar. (b) With crossbar. (c) With crossbar and solution.

Figure 2.5: Wind Tunnel and Track correlation conditions.

The tested crossbar is an elliptical cylinder with 20mm of thickness and Aspect Ratio $AR = 0.3$, and the solution refers to a typical design feature applied in commercial parts to reduce tonal noise (solution developed empirically). The objective of comparing those three conditions is to understand whether track data is capable to repeatedly capture the same noise characteristics as captured in the isolated ambient of the aeroacoustic wind tunnel. Only the spectral content of each data acquisition method was compared. Overall single values were not analyzed.

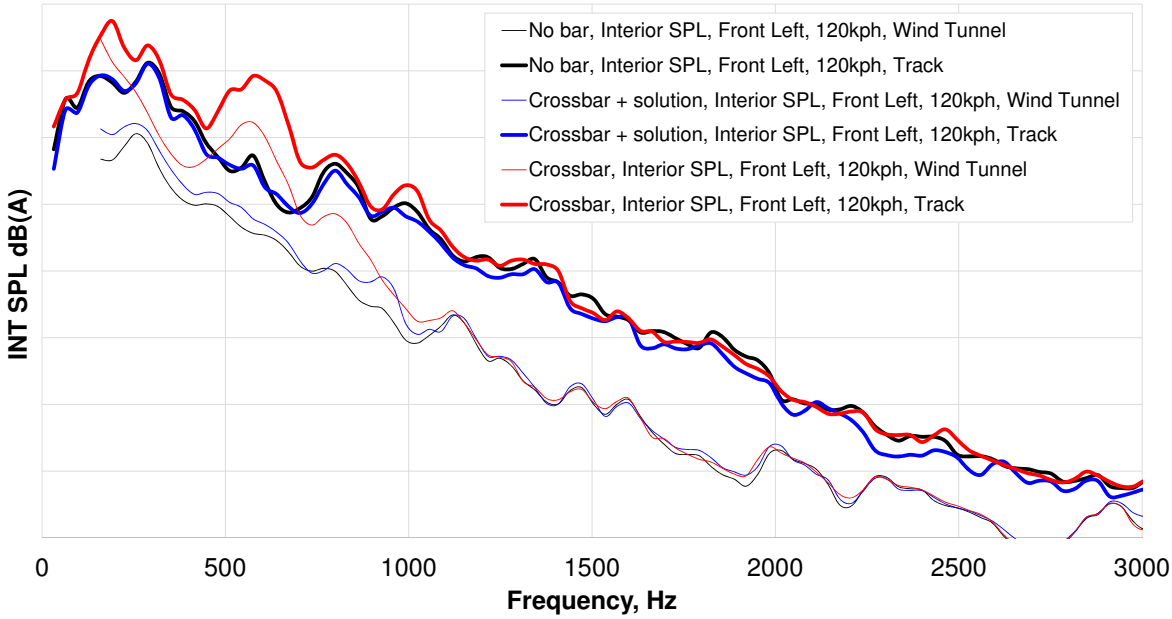

Figure 2.6: Interior noise SPL correlation.
Interior SPL [Grid = 5 dB], Frequency range: 0 – 3kHz.
Wind speed: 120km/h. Thin lines: Wind Tunnel, Thick lines: Track.
— Uncontrolled-noise crossbar, — Controlled-noise crossbar, — No bar.

Figure 2.6 shows the acoustic pressure spectral content from wind tunnel and track data taken inside the vehicle cabin (interior SPL), at the speed of 120km/h. At that speed, wind noise is the dominant airborne noise source, but the offset between the spectra proves the contribution from other airborne noise sources on-track, such as tire-pavement and powertrain airborne noise. The matching trends between track and wind tunnel data indicate, however, that the spectral content on-track is predominantly aeroacoustic noise.

Looking only at track data, one can barely see the difference between the black (no bar) and blue (bar with solution) lines at the critical frequencies of 300Hz and 600Hz. That indicates, from the receiver standpoint and at the real operational condition, that the noise generated by the crossbar is effectively mitigated. The incremental noise from the uncontrolled bar (thick red line) is clearly noticed. Looking at the wind tunnel data, all effects are amplified. In lower background noise conditions and free of disturbing noise sources, an incremental noise is observed even with the "resolved" bar case (thin blue line). The same observations were made for the 100km/h wind speed condition. That proves that the interior SPL is not the proper method to perform the present study, once a great amount of information is lost along the transmission path and the actual aeroacoustic behavior of the bar is masked.

Figure 2.7 shows the acoustic pressure spectral content from wind tunnel and track data taken outside the vehicle cabin (exterior SPL), at the speed of 120km/h. As described

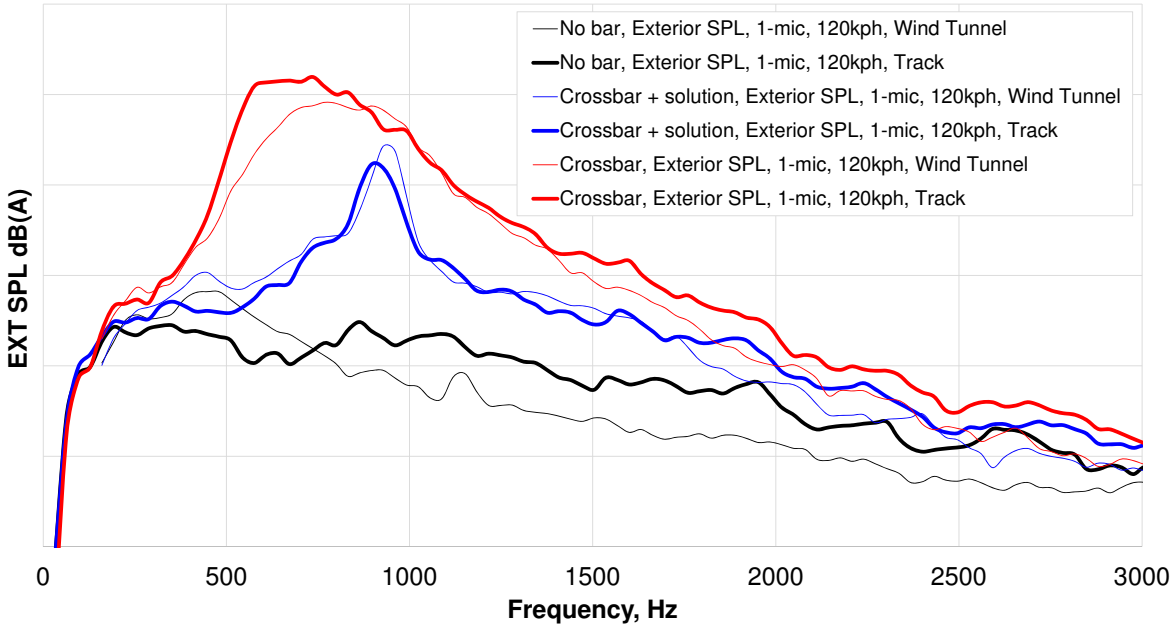

Figure 2.7: Exterior noise SPL correlation.
Exterior SPL [Grid = 5 dB], Frequency range: 0 – 3kHz.
Wind speed: 120km/h. Thin lines: Wind Tunnel, Thick lines: Track.
— Uncontrolled-noise crossbar, — Controlled-noise crossbar, — No bar.

in Section 2.3, the exterior microphone is located 300mm above the crossbar. At that acquisition location and vehicle speed, the measured noise did not differ considerably from wind tunnel to track conditions. The background noise condition (black lines) do not match, as expected, but the conditions with the installed bar (red and blue lines) match surprisingly well, both qualitatively and quantitatively. The effects of applying the solution to the bar were properly captured similarly to wind tunnel data. The same trends were observed at 100km/h.

Figure 2.8 shows the comparison of acoustic intensity measurements. The amplitudes in the spectra match reasonably well (except for the "no bar" condition) but both wind tunnel and track data are highly affected by phase mismatching below 1kHz. Those phase errors directly affect the region of interest.

When sound intensity is measured in the presence of a strong extraneous background noise, phase mismatch and random errors become significant and make the measurement results inaccurate, in special at lower frequencies. Phase mismatch errors can be caused by the measurement system itself, airflow disturbance, insufficient averaging time and/or non-stationary source (Trinh (1994)). Each one will be commented next.

Measurement system mismatch is a combined effect of phase mismatch between the two microphones of the probe and between the channels of the analyzer. The intensity measured at a point in the sound field is directly related to the phase difference detected

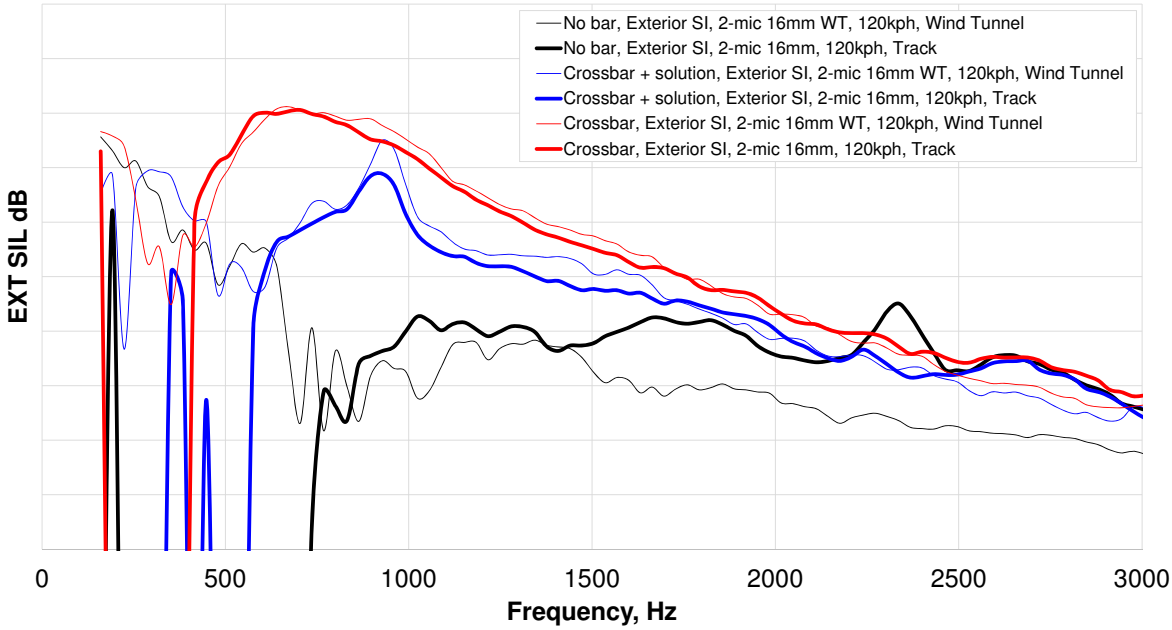

Figure 2.8: Exterior noise SIL correlation.
Exterior SIL [Grid = 5 dB], Frequency range: 0 – 3kHz.
Wind speed: 120km/h. Thin lines: Wind Tunnel, Thick lines: Track.
— Uncontrolled-noise crossbar, — Controlled-noise crossbar, — No bar.

by the system between the two microphones of the probe. Ideally, this phase angle should be purely the phase change of the sound field pressure across the two microphones, but in practice, there exists a phase mismatch in all sound intensity measurement systems. Hence, in an actual measurement, the phase difference detected between the two microphones is the sum of the actual phase change of the sound field and the system phase mismatch. For a measurement to be accurate, the system phase mismatch must be kept negligible, i.e., the phase change of the sound pressure across the microphones must be many times larger than the system phase mismatch. Consequently, the effect of system phase mismatch is most critical for small microphone spacings and at low frequencies since the sound field phase change is small in these cases. In this project, the analyzing system phase mismatch is fixed at $\pm 0.3°$ as informed by the manufacturer and, to reduce the effect of system phase mismatch at low frequencies, a larger spacing could be used, but this would reduce the system upper frequency limit. Once the next available spacer of 50mm would limit the high frequency measurements at 1.25kHz, a new spacer would need to be developed. An alternative solution would be to measure each condition with two different spacers (one for each frequency region) and process the signal separately, but that would not be practical.

Airflow disturbance can contaminate the signal from sound intensity probes. In outdoor measurements subjected to low ambient wind speeds, windscreens should be

enough to avoid abrupt pressure increase and signal contamination. In outdoor high speed measurements, nose cones are used to reduce the microphone aerodynamically self-induced noise, but they have the weakness of being subjected to turbulence and cross wind gusts. No countermeasure to airflow disturbances else than the adopted practice of measuring in shifts with still air condition is feasible in track testings.

Longer averaging time periods would be required if the sound field is contaminated with extraneous noise sources and/or a partially diffuse sound field. Under those conditions, random errors may appear. The measurement interval was set to cover the frequency range from 160 to 13,248Hz (approximately 15s), which is also the maximum time interval in which the vehicle can be accelerated to a speed of 120km/h and braked before the turn with safety. Within that 15s time interval, wind gusts can occur and potentially contaminate the signal. If the output of the sound source is not stationary with time, there will be an error in the intensity measured. In this study, the source is theoretically stationary, but in practice it varies depending on the incoming airflow condition. If the crossbar encounters a side wind gust or turbulent air, the generated tonal and broadband noise will change.

In order to reduce phase mismatch due to all potential causes described, an additional study would be required to assess system phase mismatch and optimize the probe spacer and/or the measurement acquisition interval. Nevertheless, airflow disturbance and non-stationary source would still pose a challenge on track. Added to the fact that measuring exterior acoustic pressure has demonstrated to be accurate in capturing both broad and narrowband contributions of a crossbar, and that measuring intensity demands significantly more resources than pressure (instrumentation, signal processing and data manipulation), measuring acoustic pressure with a single exterior microphone was adopted as the primary method to continue this project. Interior sound pressure was also measured, in parallel and in all runs, with the objective of monitoring the effects of the exterior noise to the occupant in specific cases. With that defined, microphone positioning, background noise and measurement variation were assessed.

2.5 Definition of Final Test Setup

The effects of microphone positioning in the longitudinal (x) and vertical (z) directions were assessed in order to define the measurement location which could offer an optimum dynamic range without signal saturation and/or extraneous noises from the sound field. The heights of 20mm, 75mm, 150mm and 300mm from the crossbar to microphone were tested (Figure 2.9). Dashed lines represent the conditions of in-flow background noise (no bar) for each microphone height. Each color refers to one microphone height. The

bar has an elliptical shape with uncontrolled noise. The heights of 20mm and 75mm are plotted, but their signal presented saturation as there were pressure peaks over 60 Pa during the acquisition interval. Extraneous noise peaks were measured in the background noise condition with the microphone at 300mm, 75mm and 20mm. The height of 150mm did not present neither signal saturation nor unknown peaks in the background, and is therefore the chosen microphone vertical position.

In the x direction, at the height of 150mm, noise was measured with the microphone installed above the center and above the Trailing Edge of the crossbar (Figure 2.9). No perceived difference justified choosing one or another longitudinal position. For practical reasons, microphone was positioned above the center of the crossbar in all further measurements. Three dimensional flow effects were considered negligible in the center region of the crossbar wake, so variations of the microphone position in y were not tested.

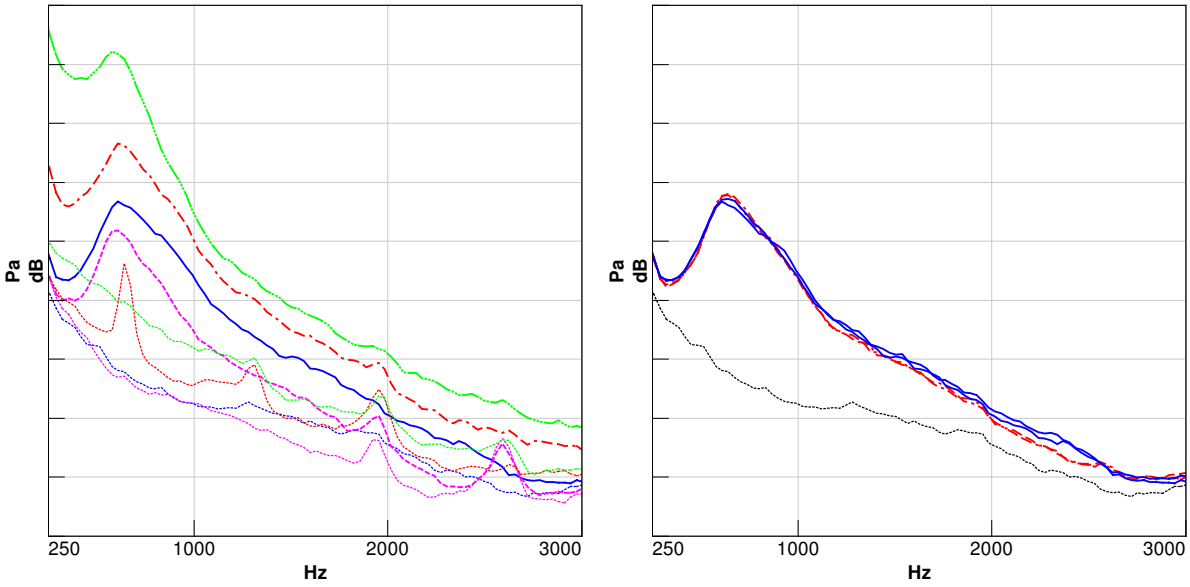

Figure 2.9: Microphone positioning in z and x.
Exterior SPL [Grid = 5 dB], Frequency range: 0.25 – 3kHz. Wind speed: 120km/h.
Left: --- $z = 300mm$, — $z = 150mm$, —· $z = 75mm$, —··· $z = 20mm$, ··· No bar.
Right: — $x = 0$ (Crossbar center), —· $x = 33mm$ (Trailing Edge), ··· No bar.

With the objective of reducing undesired noises from the background (in-flow), the vehicle exterior was treated to reduce sources of sound generated by the interaction of the airflow with the exterior surface and features of the vehicle. Roof rack longitudinal bars, windshield molding, A-pillar, exterior mirrors and door glass seals were taped. Roof antenna and windshield wipers were removed (Figure 2.10). In order to assess the influence of the microphone stand to the background noise, measurements with the interior microphone were taken with the stand on and off. No significant broad or narrowband noise increment from the microphone stand was noticed.

Figure 2.10: Background noise treatment.

The following list summarizes the final test setup and signal processing parameters.

- **Test setup**
  - Measurement type: Exterior and Interior SPL;
  - Microphones: B&K type 4189-A-021;
  - Exterior microphone self-noise treatment: Nose cones B&K UA-0386;
  - Exterior microphone location: 150mm above the center of the crossbar;
  - Interior microphone location: Right Front Headrest (RF);
  - Data acquisition front-end location: Rear left floor;
  - Test speeds: 80km/h, 100km/h and 120km/h (actual vehicle speeds).

- **Data acquisition & Signal processing parameters**
  - Measured Frequency Range: 0 to 12,800Hz;
  - Gain of each channel set to maximize signal and avoid overload;
  - Data acquisition & FFT Analyzer: LMS TestLab Ver.16A®;
  - Averaging: Linear, 50% overlap, 1000 averages (15s);
  - Frequency resolution: Narrowband bandwidth of 32Hz;
  - Channel Weighting: Linear.

2.6 Measurement Variation

One of the biggest challenges in track testing is repeatability. The variation of ambient conditions within a single or multiple test shifts (external noise factors) directly affects measured data. As described in section 2.1, several measures were taken to minimize run-to-run and shift-to-shift variation. Run variation was assessed by measuring the same design condition multiple times within a single test shift (Figure 2.11), and shift-to-shift variation was assessed by repeating the same measurements in different test shifts (Figure 2.12). Within the region of interest from 100 to 3kHz, the maximum amplitude variation observed across the spectra is 1 dB at 80km/h and 0.5 dB at 120km/h (Figure 2.11), which is considered an excellent run variation in experimental aeroacoustics given the transient nature of the flow field. Variation within shifts is 5 dB at 80km/h and 3 dB at 120km/h (Figure 2.12), which also represents a good repeatability taking into consideration all the external noise factors that aeroacoustic measurements on track are subjected to. At the controlled wind tunnel environment, lower run-to-run and shift-to-shift variation is expected, but the deltas measured on track increase confidence for the execution of this project. In all upcoming data analysis, those observed levels of variation were taken into consideration.

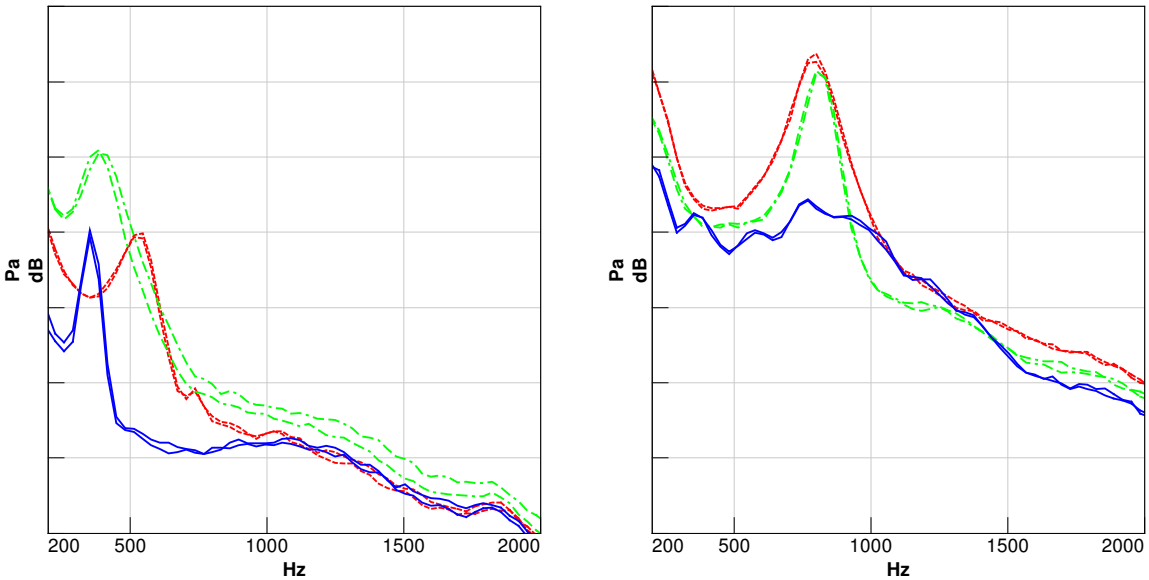

Figure 2.11: Test run variation.
Exterior SPL [Grid = 5 dB], Frequency range: 0.2 – 2kHz.
Left: 80km/h, *Right:* 120km/h.
— Condition A (two runs), --- Condition B (two runs), —· Condition C (two runs).

With the objective of assessing the influence of the ambient air conditions on the test shift variation, weather data was collected by the CAPG calibrated weather station

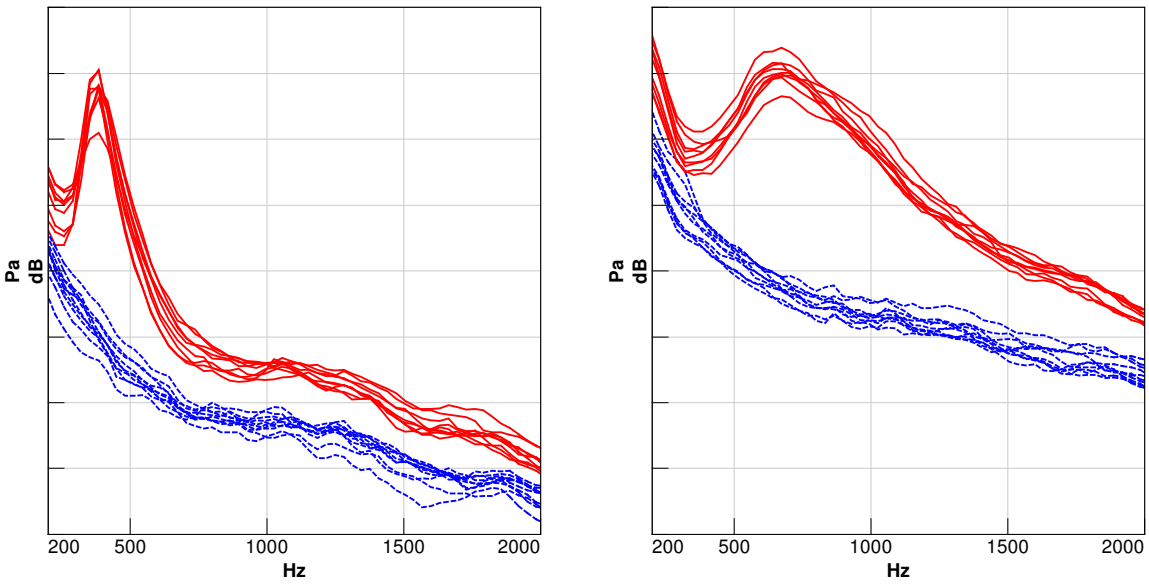

Figure 2.12: Test shift variation.
Exterior SPL [Grid = 5 dB], Frequency range: 0.2 – 2kHz.
Left: 80km/h, *Right:* 120km/h.
--- No bar (ten different test shifts), — Reference ellipse (ten different test shifts).

(Figure 2.13), and the Sound Pressure Levels of the background noise (no bar) and reference ellipse conditions, at the frequency where the broad tonal from the ellipse occurs, were plotted in reference to the local ambient air temperature (Figure 2.14) and to the maximum wind speed within the test shift period (Figure 2.15). No direct relationship between ambient air temperature and Sound Pressure Level was observed. At 80km/h, the SPL both with and without the crossbar slightly tends to increase with the increase in air temperature, but the sample of data points is too small and the coefficient of determination (R^2) is within the 0.01 to 0.16 range, which is too small to establish the correlation. In addition, at 120km/h, the trend inverts and SPL reduces with the increase in air temperature for both conditions, but also at very low R^2 (0.02 to 0.38). Better correlation of SPL is observed to the maximum wind speed within the test shift interval (Figure 2.15). At 80 and 120km/h, the SPL tends to increase with the increase in ambient wind speed in background noise condition, as expected. With the elliptical crossbar installed, however, SPL tends to decrease with the increase in wind speed. R^2 is within the 0.03 and 0.58 range, the latter referring to reference ellipse at 80km/h condition. A potential cause for those observations is that, at the background noise condition, the microphone is subjected to head and crosswind gusts at higher speeds than in still air, resulting in higher acoustic pressure fluctuations and consequently higher average levels. In contrast, with the crossbar installed, stronger wind gradients are capable of disorganizing the coherent vortex structures developed behind the crossbar. These coherent structures are the primary contributors to the tonal noise generation.

Figure 2.13: CAPG Weather station.

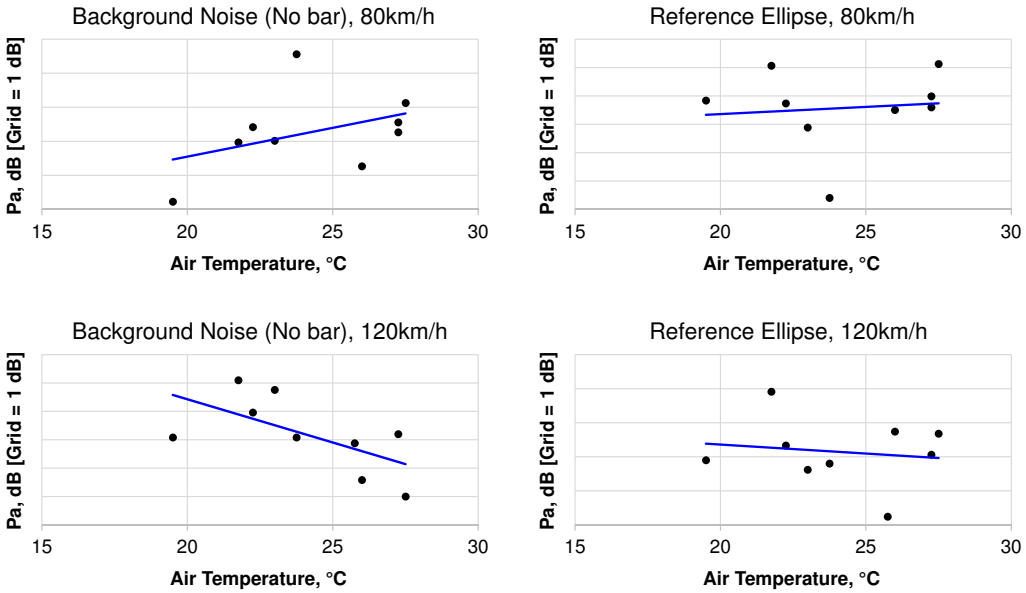

Figure 2.14: SPL variation with local ambient air temperature.

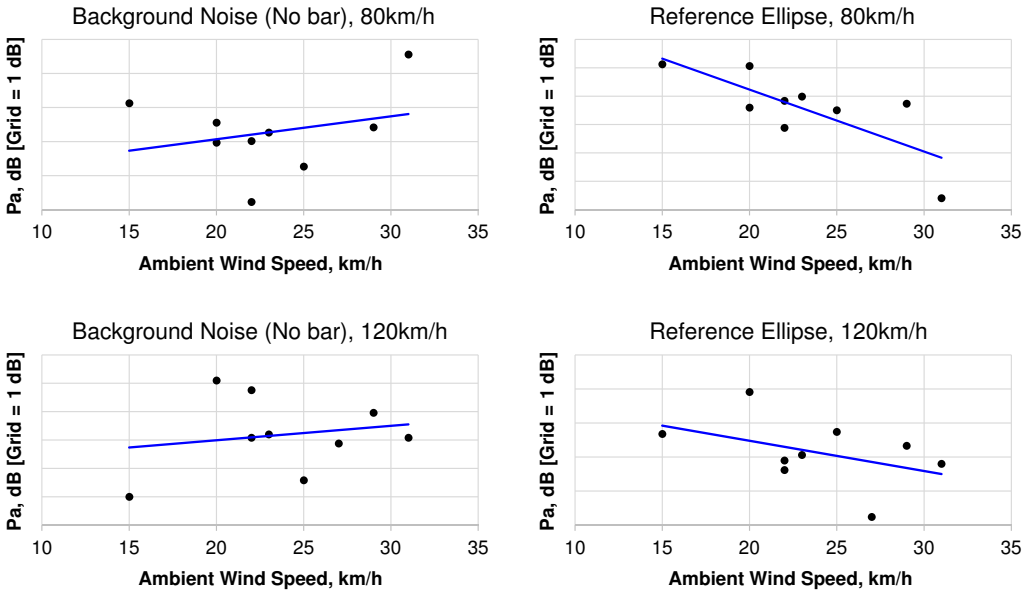

Figure 2.15: SPL variation with local ambient wind speed.

2.7 Measurement Uncertainty

Every measurement of any physical quantity is uncertain. The measurement results (also known as measurand) will always differ not only from the true value, but also from the results of repeated measurements. This characteristic of any measurement process is known as uncertainty, and its estimation is not an exact physical theory, but rather an approximate description of imperfections of experiments (Wszolek and Engel (2004)). According to JCGM 100:2008 (2008), the definition of uncertainty is: *A parameter related to the measured result, characterizing the scatter of results, which can be reasonably attributed to the measured value.* As a general rule, the causes[1] of uncertainty in acoustical measurements can be divided in the following categories (Miyara (2017)):

- Causes attributable to the measurand: An incomplete definition of the measurand (e.g. lack of specification of some variable that has a significant effect on the measurand); impossibility to warrant that the measurand's realization meets all specifications (e.g. the definition specifies the room temperature but it is known only approximately);

- Causes attributable to the measurement procedure: The model underlying the measurement method is incomplete, insufficient, or inaccurate (e.g. there is a correction of the effect of temperature but the temperature coefficient is known only approximately); Finite number of repetitions; presence of interferences or disturbances (e.g. background noise); presence of factors that alter the measurand (e.g. a reflective surface close to the measurement site); excessive effect of environmental conditions;

- Causes attributable to the measurement instrument: Finite resolution, lack of precision, manufacturing tolerance, inaccurate calibration, inadequate, or insufficient frequency response;

- Causes attributable to the operator: Alteration of the measurand due to their presence; parallax errors while reading analogical instruments; indecision on what value should be recorded from a digital instrument when the least significant digits fluctuate over time.

[1] Sources of uncertainty should not be confused with gross errors, mistakes, lack of calibration or incorrect application of procedures. It is assumed that all these defects have been prevented and all measurements are conducted by knowledgeable personnel.

In sound pressure meter systems, there are many noise factors to be considered when assessing the measurement uncertainty. The uncertainty contributions may be considered in two groups, one associated with the instrumentation itself (Group A), and the other associated with the operation of the equipment (Group B).

Group A - Instrumentation:

The basic acoustical measuring instrument subjected to most of noise factors are the microphones. All of the electronic components used in a sound level meter such as resistors, capacitors and even microprocessors will have very slight differences and these all sum up to give each microphone its own variation from the ideal. There are also other factors such as the uncertainty of the measurements made when an microphone is being certified and calibrated. The equipment used to test and calibrate a sound level meter has itself some level of tolerance and all of those factors also contribute to the total microphone uncertainty.

According to JCGM 100:2008 (2008), it is recommended that uncertainty is stated in terms of 2 standard deviations (2σ). This means that 95% of the calibrations will be within the stated uncertainty range for a normal distribution function. Normally, the uncertainty decreases the higher up in the hierarchy the chain the calibrations are performed, with absolute calibration methods based directly on the physical units at the top of the hierarchy (Brüel&Kjaer (1996)). The microphone units used in the experiments of this project (Brüel & Kjaer 1/2" type 4189-A-021) are Class 1 (IEC 61672), traceable by DPLA (Danish Primary Laboratory of Acoustics, Denmark) and NIST (National Institute of Standards and Technology, USA), with an uncertainty level of ±0.2 dB with 95% of confidence level (Figure 2.16).

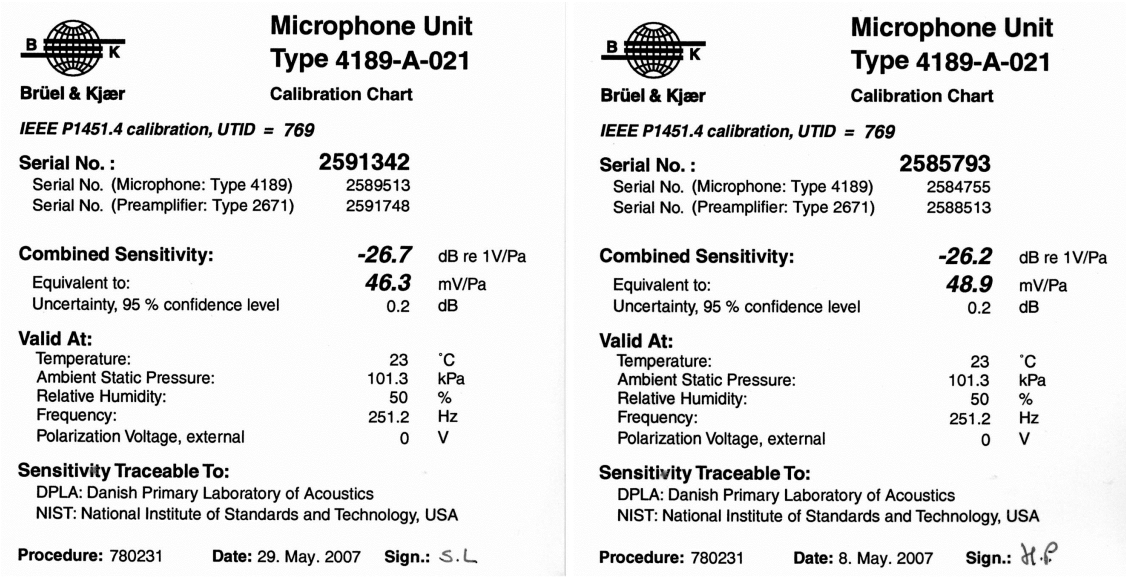

Microphone Unit
Type 4189-A-021

Brüel & Kjær **Calibration Chart**

IEEE P1451.4 calibration, UTID = 769

Serial No. :	**2591342**	
Serial No. (Microphone: Type 4189)	2589513	
Serial No. (Preamplifier: Type 2671)	2591748	
Combined Sensitivity:	***-26.7***	dB re 1V/Pa
Equivalent to:	***46.3***	mV/Pa
Uncertainty, 95 % confidence level	0.2	dB
Valid At:		
Temperature:	23	°C
Ambient Static Pressure:	101.3	kPa
Relative Humidity:	50	%
Frequency:	251.2	Hz
Polarization Voltage, external	0	V

Sensitivity Traceable To:
DPLA: Danish Primary Laboratory of Acoustics
NIST: National Institute of Standards and Technology, USA

Procedure: 780231 **Date:** 29. May. 2007 **Sign.:** S.L

Microphone Unit
Type 4189-A-021

Brüel & Kjær **Calibration Chart**

IEEE P1451.4 calibration, UTID = 769

Serial No. :	**2585793**	
Serial No. (Microphone: Type 4189)	2584755	
Serial No. (Preamplifier: Type 2671)	2588513	
Combined Sensitivity:	***-26.2***	dB re 1V/Pa
Equivalent to:	***48.9***	mV/Pa
Uncertainty, 95 % confidence level	0.2	dB
Valid At:		
Temperature:	23	°C
Ambient Static Pressure:	101.3	kPa
Relative Humidity:	50	%
Frequency:	251.2	Hz
Polarization Voltage, external	0	V

Sensitivity Traceable To:
DPLA: Danish Primary Laboratory of Acoustics
NIST: National Institute of Standards and Technology, USA

Procedure: 780231 **Date:** 8. May. 2007 **Sign.:** H.P

Figure 2.16: Microphones sensitivity and uncertainty.

The calibration of the microphone also contributes to the total measurement uncertainty. The sensitivity before each measurement was calibrated using Brüel & Kjaer microphone calibrator type 4231 (EN/IEC 60942 Class LS and Class 1, and ANSI S1.40–2006). According to supplier documentation, the calibration accuracy is ±0.2 dB specified at 2σ.

In addition to the uncertainty attributed to the microphone unit, the employment of accessories, in this case the nose cones Brüel & Kjaer type UA-0386, also represents a noise factor contributing to the total measurement uncertainty. However, there is no available information on the specific uncertainty of the nose cones. On the other hand, the nose cone is a geometric element which is fixed in all measurements, and its contribution to the scatter of results can be considered negligible. Uncertainty associated with the periodic calibration of the sound microphone and the sound calibrator, so that it is traceable to appropriate standards, also plays in a role in the inherent instrumentation uncertainty, however that is dependent on the quality control system of the authorized laboratory and is also considered negligible.

Group B - Operation:

Several operational noise factors affect measurement uncertainty, to mention: the contributions associated with variation in ambient temperature and pressure, installation of the instrumentation, adjustment of the sound level meter during calibration with the sound calibrator, equipment operation timing (e.g. triggering time), an potentially others. The assessment of those operational uncertainty quantities would require a separate study which is not in the scope of the present study. In order to minimize the effects of operation uncertainty in the repeatability of the measurements, the measures described in Section 2.1 were taken. In addition, the number of instrumentation re-installments was minimized and an unique operator triggered all measurements during the experiments window.

3 GEOMETRIC ASSESSMENT

3.1 Wake Interaction

The first step given towards understanding the fundamental aeroacoustic noise mechanisms in elliptical shape crossbars was to investigate the effect of the vehicle roof on the near-wake flow structure of the crossbar and how it could possibly affect the generated noise in comparison to free-flow and free-sound field condition. The confusing interaction of the crossbar wake with the boundary layer formed on the roof is called wake interference or wake interaction.

The flow regime around the crossbar is analogous to that of a blunt body in ground effect at moderate to high Reynolds ($Re_c = 80,000 - 300,000$), except for the ground (vehicle roof) that moves with the crossbar and develops a boundary layer. Therefore, it is expected that the flow around the crossbar will depend not only upon the Reynolds number and the gap between the crossbar and the roof, but also upon the characteristics of the roof boundary layer. In this project, the gap from the roof to the bottom surface of the crossbar (h) is fixed at $40mm$, respecting several dimensional criteria and style requirements. The non-dimensional gap-thickness ratio, or just gap-ratio, is $h^* = \frac{h}{thickness} = 2$. The Aspect Ratio ($AR = \frac{thickness}{chord}$) of the elliptical crossbar is 0.3.

There are several experimental and numerical studies in literature describing the flow past a circular cylinder in the vicinity of a plane wall. Understanding the interaction between the boundary layer developed over a flat plate and a bluff body wake for different flow regimes and gap ratios is a topic of academic interest, given the geometric simplicity and the vortex shedding characteristics, as well as the wide range of engineering applications, e.g. heat exchangers, chimneys, undersea pipelines (Choi and Lee (2000), Bimbato *et. al* (2009), Cavalheiro *et. al* (2016)), and now automotive roof crossbars. However, there are few studies describing the flow dynamics over an elliptical cylinder near a plane wall, in special at moderate and high Reynolds numbers.

Choi and Lee (2000) have studied the wake interaction of an elliptical cylinder near a flat plate immersed in a turbulent boundary layer ($AR = 0.5$, $h^* = 0 - 2$, $Re_c = 14,000$), using hot-wire anemometry and smoke-wire flow visualization. Vortex shedding frequencies for the ellipse and a reference cylinder body ($AR = 1$) were compared by spectral analysis. The authors have found the critical gap-ratio of the elliptical cylinder, at which periodic vortices cease to shed, is larger than that of a circular cylinder with

the same thickness, meaning that the ground effect suppressing regular vortex shedding is stronger in the elliptical cylinder when compared to a circular cylinder ($h^*_{ellipse} \simeq 0.4$, $h^*_{circ.cyl.} \simeq 0.3$). Daichin (2001) assessed the wake interaction of an elliptical cylinder ($AR = 0.5$, $h^* = 0 - 1.1$, $Re_c = 2,900$) in a water channel using PIV. Vortex suppression started at $h^* \simeq 0.4$ in accordance with Choi and Lee (2000). At $h^* > 0.4$, the vorticity contours at the top and bottom sides of the ellipse are nearly symmetric with respect to the major axis of the ellipse, and the maximum of the positive and negative Reynolds stress are symmetrically distributed. However, the presence of the free layer causes the shear layer at the side closer to the wall to have a slightly higher velocity than the opposite shear layer (Figure 3.1), suggesting the presence of the ground would cause a slight increase in the natural frequency of the von Karman vortices. Recently, Cavalheiro *et. al* (2016) have used a hydrodynamic tunnel and dye colors to visualize the wall influence on the wake of a elliptical cylinder ($AR = 0.33$, $h^* = 0.2 - 1$, $Re_c = 2 - 2,200$), and have demonstrated the wall effect is more prominent in the far wake than the near wake, which is the critical region for noise generation aspects. It was also demonstrated that as Reynolds increases, the wake interaction with the wall starts earlier, what could potentially affect the generated sound at the trailing edge of the ellipse in high Reynolds numbers (Figure 3.2).

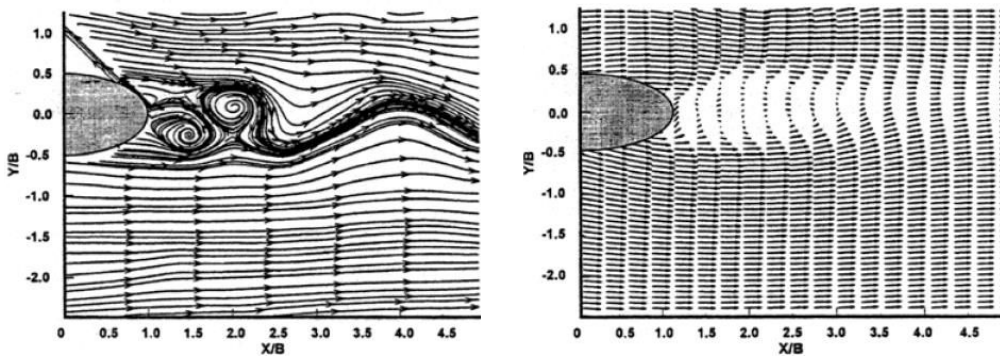

(a) Streamline contours. (b) Variations of mean velocity profile.

Figure 3.1: Ellipse flow structure at $h^* = 0.7$ (wall at the upper edge), adapted from Daichin (2001).

For higher Reynolds flows and thin wall boundary layers (conditions closer to this project), references were found only for circular cylinders. Bearman and Zdravkovich (1978) have investigated vortex suppression for a cylinder at $Re = 25,000 - 48,000$ in a wind tunnel using smoke flow visualization and hot wire anemometry for pressure coefficients. Gap-ratios h^* from 0 to 3.5 were assessed and revealed $h^*_{critical}$ for the cylinder is 0.3, as later confirmed by many authors. At $h^* = 2$ (same gap-ratio of this project), vortex shedding was similar to free-flow condition. However, considering $h^*_{ellipse} > h^*_{circ.cyl.}$, as previously observed, it is unknown only from literature whether at $h^* = 2$ there will

Figure 3.2: Flow around an elliptical cylinder at varying Reynolds ($AR = 0.33$, $h^* = 1$), adapted from Cavalheiro *et. al* (2016).

be no vortex suppression effects for the ellipse case. Added to the fact that the distance at which vortex starts to interact with the wall reduces with the increase of Reynolds, and that Reynolds of the present work is higher than those found in the literature, an experiment of flow visualization was performed.

A portable digital camera was installed on the vehicle roof and tufts of yarn were distributed along the roof and over the crossbar (Figure 3.3). Two different tuft thicknesses were used to minimize tuft inertia error. By comparing the dynamic behavior of the roof tufts before and after the crossbar at the vehicle speeds of interest, it was possible to visualize no evident interaction of the crossbar wake with the roof boundary layer, as shown in the screen captures of the Figures 3.4 and 3.5. Tufts after the crossbar kept attached within roof boundary layer as the ones before the bar, indicating no concerning interaction at the near-wake capable to drastically affect the noise generation mechanisms.

Literature on the acoustics of circular and elliptical cylinders near a plane wall is very scarce. The effect of the roof on the noise generated by the cylinder can be deduced from the available observations of flow structure changes under those conditions. Bearman and Zdravkovich (1978) demonstrated that, for a circular cylinder, the vortex shedding frequency (and consequently Strouhal number) increases with the decrease of h^* (also shown by Angrilli *et. al* (1982)). In summary, the closer the body is to the wall, the higher will be the vortex shedding frequency in comparison to free-flow, until it reaches $h^*_{critical}$ and vortices start to cease. Therefore, since $h^* > h^*_{critical}$, the main tone frequency emitted by the crossbar regular shedding vortices in the presence of the vehicle roof is expected to be higher than in free-sound field. In order to verify that effect in the conditions of the present study, the noise from a 19mm diameter circular

(a) Tufts of yarn and camera installation. (b) Camera view.

Figure 3.3: Roof flow visualization setup.

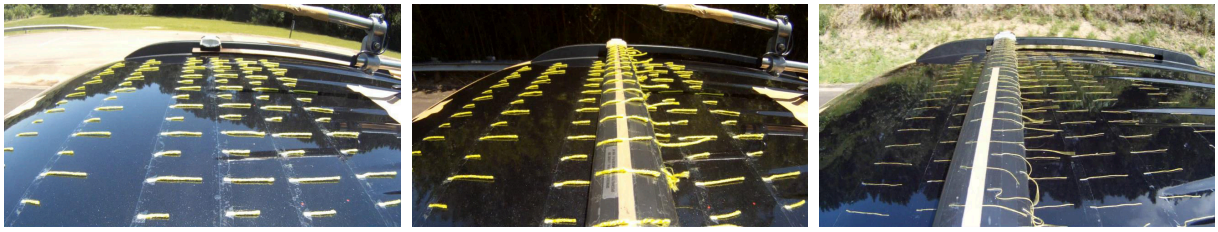

(a) No crossbar. (b) With crossbar (thicker tufts). (c) With crossbar (thinner tufts).

Figure 3.4: Roof flow visualization at 80km/h ($Re_c = 98,000$).

(a) No crossbar. (b) With crossbar (thicker tufts). (c) With crossbar (thinner tufts).

Figure 3.5: Roof flow visualization at 120km/h ($Re_c = 147,000$).

cylinder installed on the roof (Figure 3.6a) was measured with the setup described in section 2.5 and compared to free-flow theoretical data (Strouhal (1878)). The measured spectra (Figure 3.7) clearly reveal the main tones and their first and second harmonics (marked with black lines for the speed of 120km/h). The measured main tone frequencies are 256Hz, 310Hz and 375Hz for the actual wind speeds of 80km/h (22m/s), 100km/h (28m/s) and 120km/h (33m/s) respectively, which correspond to Strouhal numbers of 0.218, 0.212 and 0.214. The expected frequencies considering the fundamental Strouhal number ($St \simeq 0.2$, section 1.5.2) are 234Hz, 292Hz and 351Hz, i.e. an average of 20Hz lower than measured, confirming statements from Bearman and Zdravkovich (1978).

In addition to the gap-ratio ground effect that increases vortex shedding frequency, there are sound absorption, reflection, scattering and interference effects caused by the roof panel. Those effects were briefly assessed by changing the ground material from

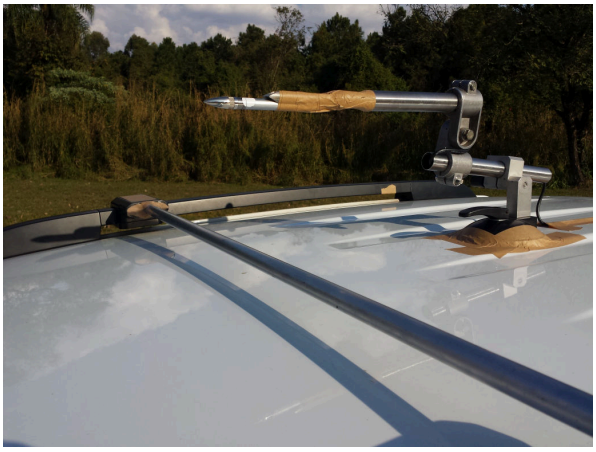

(a) Circular cylinder measurement setup.

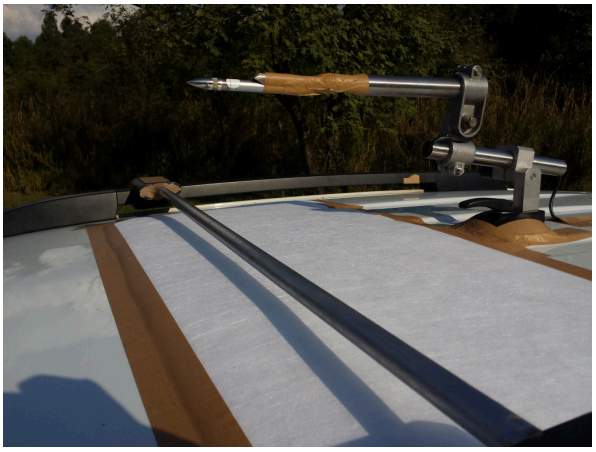

(b) Fibrous material ground.

Figure 3.6: Circular cylinder reference measurements.

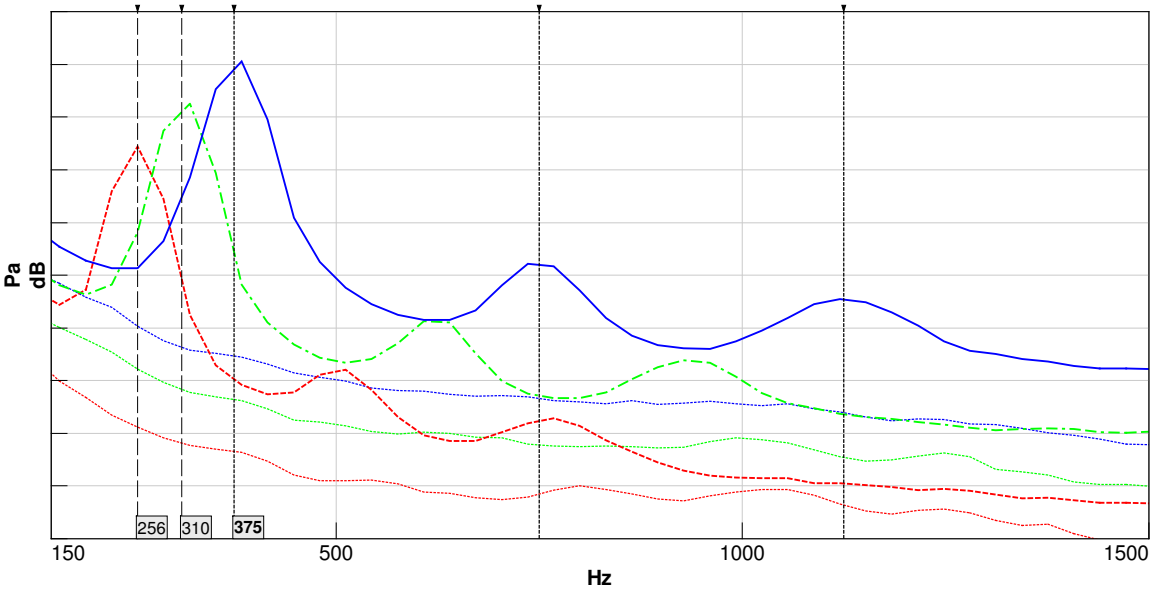

Figure 3.7: Circular cylinder noise at varying speeds.
Exterior SPL [Grid = 5 dB], Frequency range: 0.15 – 1.5kHz.
--- 80km/h, —· 100km/h, — 120km/h, ··· No bar.

sheetmetal to a random fibrous material (Figure 3.6b). Adding a layer of fibrous material on the roof did change the tonal noise drastically in both amplitude and frequency. That effect is a result from reducing the gap-ratio from $h^* = 2$ down to approximately 1, from creating a ground step before the crossbar, and from changing the acoustic absorption and reflection characteristics of the ground. Better understanding those effects would demand a parallel study which is not in the scope of the project, which focuses on elucidating the noise mechanisms and studying solutions at the real operational condition. The critical information at this point of the study is that the presence of the roof is not substantially changing the airflow physics and aeroacoustic noise generation mechanisms in comparison to a free-flow and free-sound field domain.

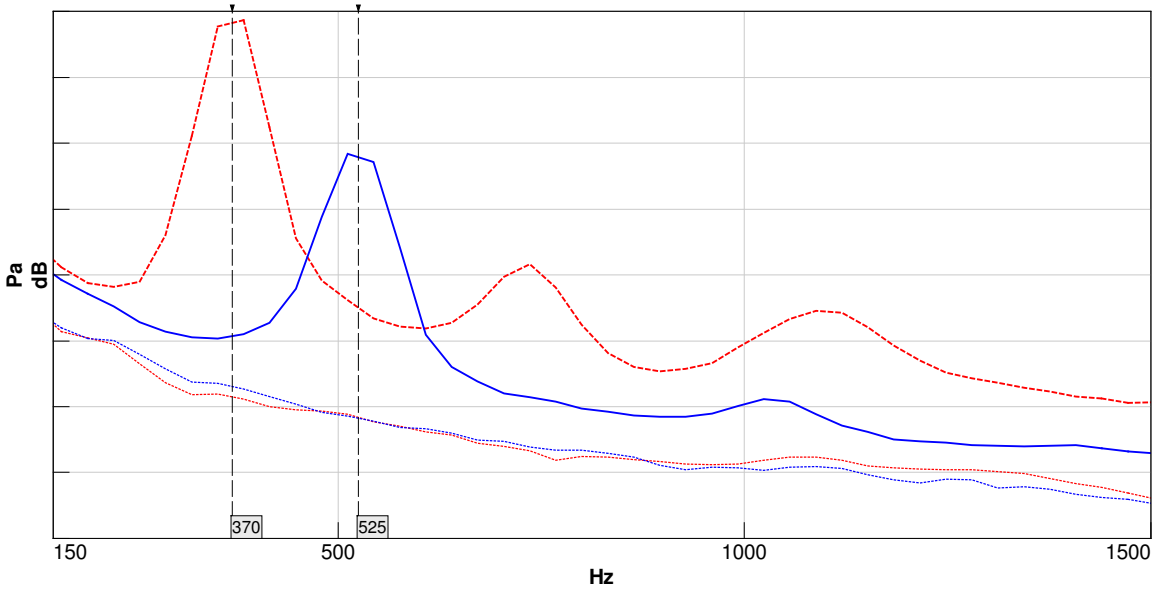

Figure 3.8: Fibrous material on roof effect.
Exterior SPL [Grid = 5 dB], Frequency range: 0.15 – 1.5kHz.
Wind speed: 120km/h ($Re_c = 42,369$).
--- Original Sheetmetal roof, — Fibrous material on the roof, ··· No bar.

3.2 Reference Profiles

With the objective of understanding the aeroacoustic noise mechanisms of an elliptical shape crossbar, the noise from a reference elliptical cylinder at zero Angle of Attack was measured and compared to the noise generated by two canonical profiles which aeroacoustic characteristics are well known from the literature: the circular cylinder and the NACA 0012 airfoil (Figure 3.9). Their noise generations mechanisms were previously discussed in Section 1.5.2.

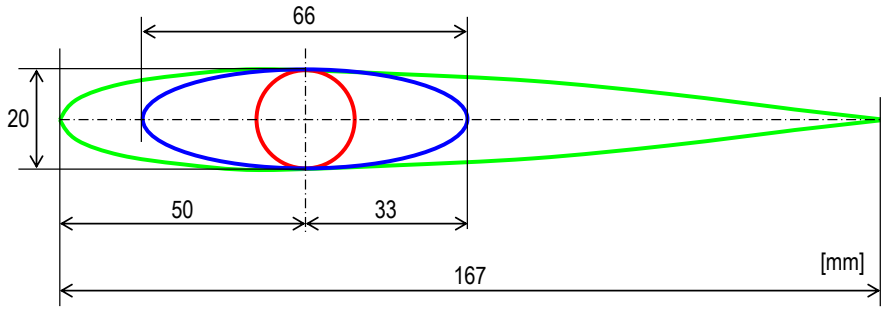

Figure 3.9: Reference profiles 2D sections.
— Circular cylinder, — Elliptical cylinder, — NACA 0012.

The elliptical cylinder trailing edge is an almost-perfect transition from the blunt circular cylinder to the thin airfoil profile. The thickness of the profiles was fixed at 20mm. Both circular and elliptical cylinders are Aluminum extrusions with highly polished surface, and the NACA 002 airfoil was profiled out of solid wood in a wood shop using milling machine and a belt sander (Figure 3.10). The NACA 0012 profile was coated in plastic film to grant it a highly sleek finishing. Figure 3.11 shows the final test parts installed on the roof of the vehicle. Zero Angle of Attack was obtained with the use of a goniometer. The gap-ratio to roof is constant and the parts are centered longitudinally at their maximum thickness vertical axis, i.e. the center of the circular and elliptical cylinders and at 30% of the chord of the NACA 0012.

(a) Solid wood blank. (b) Belt sander. (c) Profiled airfoil.

Figure 3.10: NACA 0012 fabrication.

(a) Circular cylinder. (b) Elliptical cylinder. (c) NACA 0012.

Figure 3.11: Reference profiles.

Figure 3.12 reveals the noise spectra for the three bodies tested at the same operational conditions, with focus on the frequency range within which the main tones occur (0.1 − 2kHz). In lower Reynolds (80km/h, $Re_c = 98,000$), noise behavior of the elliptical cylinder is similar to the circular cylinder. The ellipse presents a discrete narrowband tone at a similar frequency (slightly higher) and lower acoustic pressure than the circular cylinder, suggesting the main vortex shedding structure from the ellipse is not as well defined and does not initiate as near to the circular cylinder, as the von Karman vortex street. Consequently, the unsteady surface pressures and the dipole source of sound loose strength. The ellipse also did not present the harmonics of the circular cylinder. At 100km/h ($Re_c = 123,000$), the circular cylinder tonal peak increases in amplitude and

frequency proportional to $f_0 = \frac{St_0 U_0}{D}$ ($St_0 \approx 0.2$). The elliptical cylinder peak, however, keeps its amplitude and widen its bandwidth, assuming broad tonal characteristics. As Reynolds increases further, the elliptical cylinder noise deviates from the circular cylinder behavior and approaches that of the NACA 0012. At 120km/h ($Re_c = 147,000$), the ellipse noise presents the hump behavior, i.e. a broadband contribution centered on a main frequency, aligned with the NACA 0012 noise frequencies.

Figure 3.13 compares the noise from each profile at a different perspective. Each frame brings the noise of one profile at increasing Reynolds. The pattern which each profile progress with the increase of Reynolds is very different. The circular cylinder maintains the discrete tones and their harmonics at higher pressure levels. The elliptical shape widens its incremental noise frequency with a small increase in amplitude. The NACA 0012 noise interestingly preserves its frequency range with a linear offset in amplitude.

Figure 3.14 covers the frequency range up to 5kHz, to give rise to broadband effects. Past the tonal peak region, ellipse broadband noise is slightly higher than that of the NACA 0012 until both match the in-flow background noise condition (no bar) at approximately 3kHz. In contrast, the circular cylinder broadband noise contribution grows and is higher than the background noise condition in all frequencies, indicating the presence of eddies of many scales supporting quadrupole sources in the growing wake.

Conclusively, in regards to the tonal nature, elliptical profiles noise characteristics depend on the Reynolds regime (the lower Reynolds, the more it behaves as a blunt body). In regards to broadband noise, the elliptical cylinder generates more noise than the NACA 0012, but less than the circular cylinder in all Reynolds conditions. The main and secondary ladder-structure discrete tones from the NACA 0012 (Arbey and Bataille (1983)) were not observed in the NACA 0012 and the elliptical profiles at zero Angle of Attack[1]. From the receiver perspective in the vehicle's interior (Figure 3.15), the circular cylinder is the worst case in terms of tonal noise. The elliptical cylinder is also very annoying to the occupants as the increment at the center frequency is approximately 5 dB at the speeds of 100km/h and 120km/h. Above 1kHz, most of the broadband noise from any profile is either reflected or attenuated in the path.

[1]NACA 0012 noise was also measured at positive and negative incidence angles to give rise to the secondary tones, and the results are presented in Appendix B.

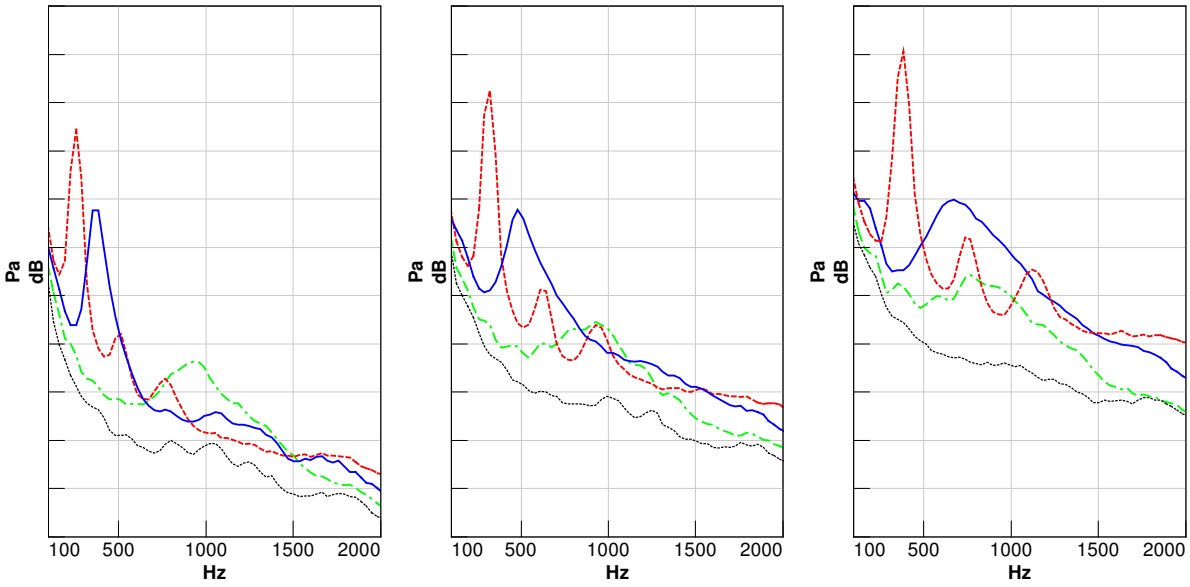

Figure 3.12: Reference profiles noise at varying wind speeds.
Exterior SPL [Grid = 5 dB], Frequency range: 0.1 – 2kHz.
Wind speeds: 80km/h (*left*), 100km/h (*center*), 120km/h (*right*).
--- Circular cylinder, — Elliptical cylinder, —· NACA 0012, ··· No bar.

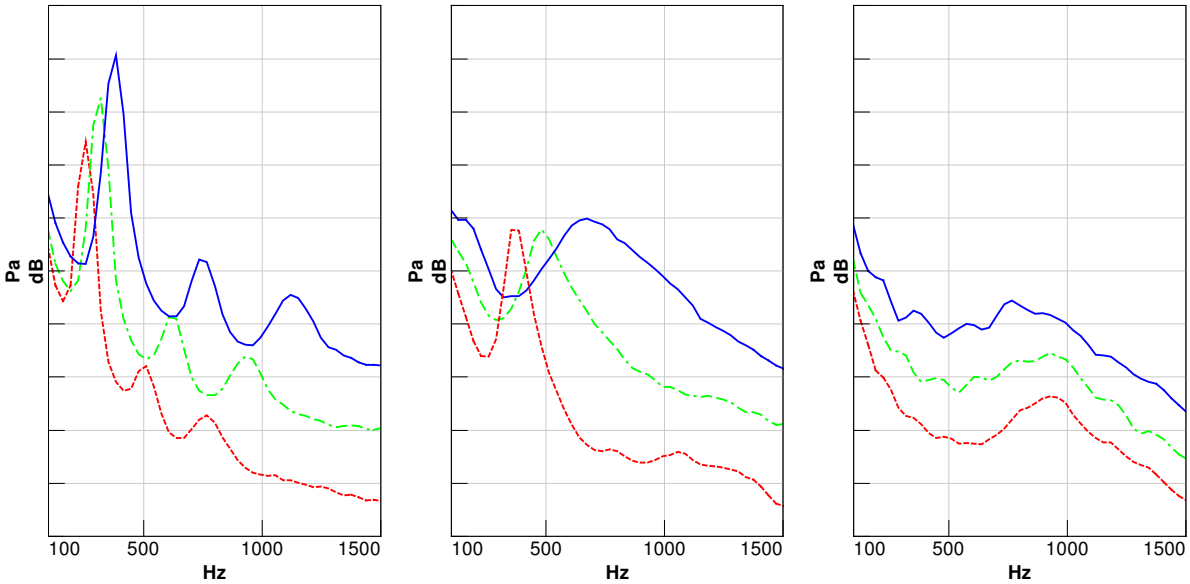

Figure 3.13: Reference profiles noise Reynolds effect.
Exterior SPL [Grid = 5 dB], Frequency range: 0.1 – 1.5kHz.
Circular cylinder (*left*), Elliptical cylinder (*center*), NACA 0012 (*right*).
Wind speeds: --- 80km/h, —· 100km/h, — 120km/h.

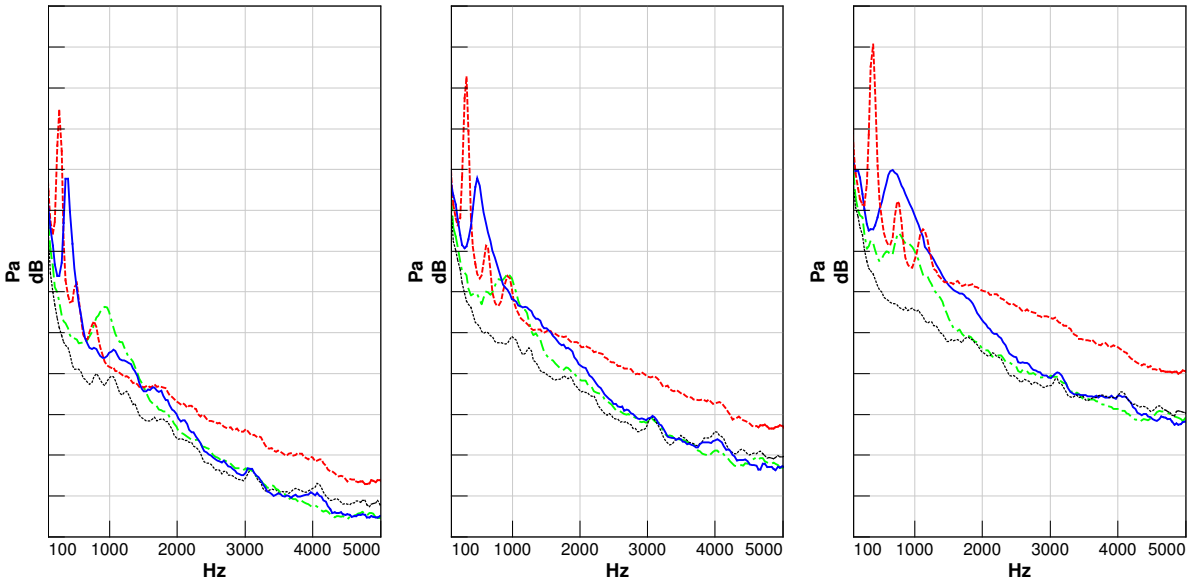

Figure 3.14: Reference profiles noise at varying wind speeds.
Exterior SPL [Grid = 5 dB], Frequency range: 0.1 – 5kHz.
Wind speeds: 80km/h (*left*), 100km/h (*center*), 120km/h (*right*).
--- Circular cylinder, — Elliptical cylinder, —· NACA 0012, ··· No bar.

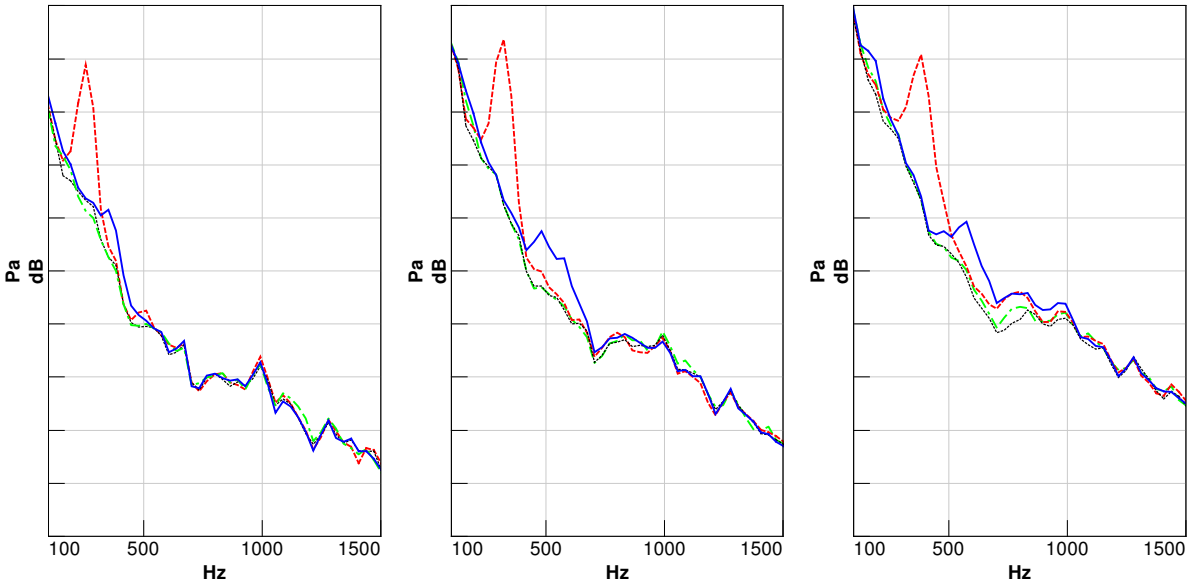

Figure 3.15: Reference profiles noise at varying wind speeds.
Interior SPL [Grid = 5 dB], Frequency range: 0.1 – 1.5kHz.
Wind speeds: 80km/h (*left*), 100km/h (*center*), 120km/h (*right*).
--- Circular cylinder, — Elliptical cylinder, —· NACA 0012, ··· No bar.

3.3 Elliptical Cylinder Geometry

Grounded on the learnings that the NACA 0012 presents minimum broadband noise contribution and no discrete tones at the flow conditions of interest, different leading and trailing edge configurations were clay-milled and tested with the objective of identifying which are the effective trends towards noise reduction in elliptical crossbars. To build the clay models, an Aluminum cross-profile (Figure 3.16a) was machined and used as core, splitting the elliptical geometry into four uniform quadrants (Figure 3.16b) to be separately explored. Aluminum templates (Figure 3.16c) were cut to the desired outlines and used to hand-mill the clay bars (Figure 3.16d), which were covered in flatback tape to keep its surface roughness controlled (Figure 3.16e-f).

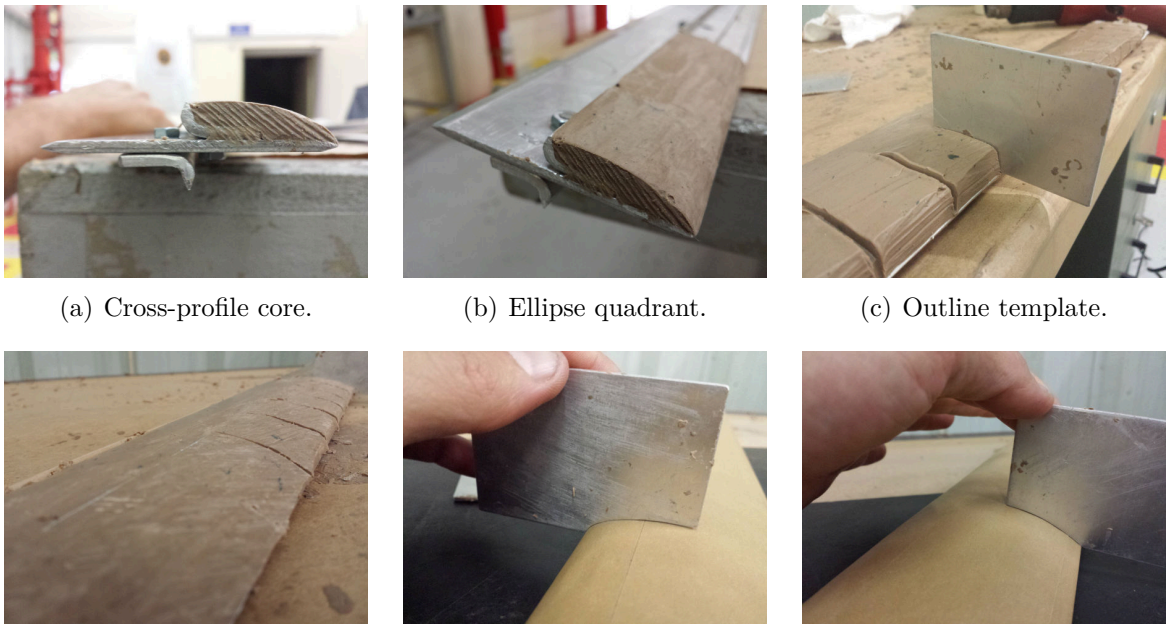

(a) Cross-profile core. (b) Ellipse quadrant. (c) Outline template.

(d) Clay milled surface. (e) Sleek finishing (LE). (f) Sleek finishing (TE).

Figure 3.16: Clay milled crossbar.

The following parameters were assessed:

- Trailing edge bluntness
- Trailing edge asymmetry
- Leading edge bluntness
- Leading edge asymmetry
- Leading and trailing edge asymmetry

3.3.1 Trailing Edge Bluntness

Figure 3.17 shows the different trailing edge 2D sections milled and tested. The sections are plotted over the circular cylinder and the NACA 0012 in gray as reference. The leading edge was kept elliptical for all trailing edge configurations (blue line). Figure 3.18 shows the crossbar parts after milling and finishing with flatback tape. Clay-over-tape technique (different surfaces divided by tape) was adopted to allow measuring all sections in a single test shift excluding the need of re-milling and reinstalling parts, hence minimizing noise factors.

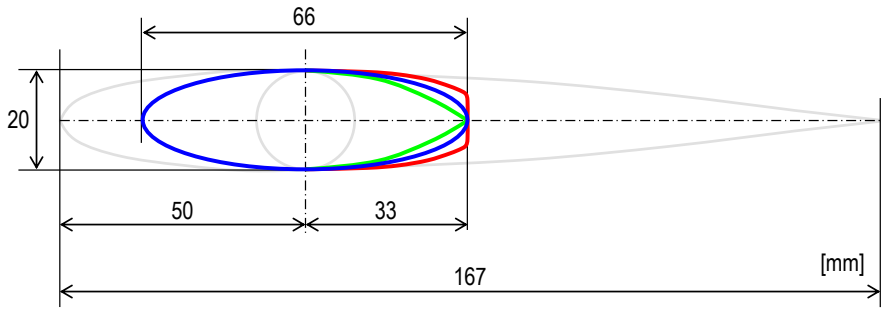

Figure 3.17: Different trailing edge bluntness 2D sections.
— Blunt TE, — Elliptical TE, — Thin TE.

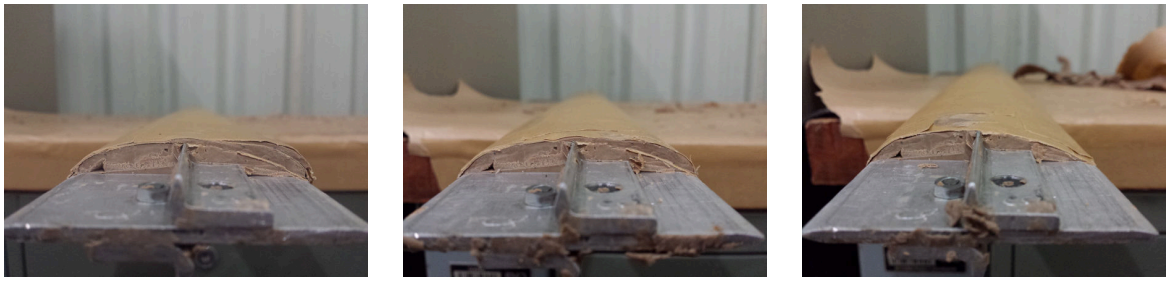

(a) Blunt TE. (b) Elliptical TE. (c) Thin TE.

Figure 3.18: Different trailing edge clay bars.

Figure 3.19 reveals the noise spectra of the different trailing edge configurations plotted according to Reynolds. In all flow conditions, the blunt trailing edge caused an increase in the main vortex intensity (higher pressure level) and a reduction in bandwidth when compared to the elliptical trailing edge, thus behaving similar to the blunt body represented by a circular cylinder. The periodicity and pressure fluctuation is not as strong as the circular cylinder, so the main tone frequency is not as low as for the circular cylinder, and the harmonics are not present. The broadband noise generated by the blunt trailing edge is slightly lower than the elliptical trailing edge case, indicating the boundary layer separation forms more unstable shear layers that originate stronger eddies, and consequently higher broadband noise than the elliptical trailing edge case.

In an opposite direction, the thin trailing edge completely eliminated the main tone. The spectrum of the thin trailing edge contains essentially a significant broadband noise increment when compared to the elliptical and blunt trailing edges, which is the main characteristic of the NACA 0012 noise signature as shown in section 3.2. The results are in agreement with the numerical study presented by Ramirez and Wolf (2016) in regards to the tonal noise characteristics, i.e. with the increase of trailing edge bluntness in an airfoil at M_∞ from 0.2 to 0.5, the dominant tonal noise peak increases in amplitude and shifts to lower frequencies (Figure 3.20). DNS calculations in the near-field coupled with FW-H Acoustic Analogy formulation demonstrated the effects of compressibility on the vortex shedding sound generation and propagation of the NACA 0012 airfoil with different Trailing Edge bluntness radii (Figure 3.21). The pressure fluctuation in the near wake of the trailing edge generates an aeroacoustic dipole source with higher amplitude and period, at a lower frequency.

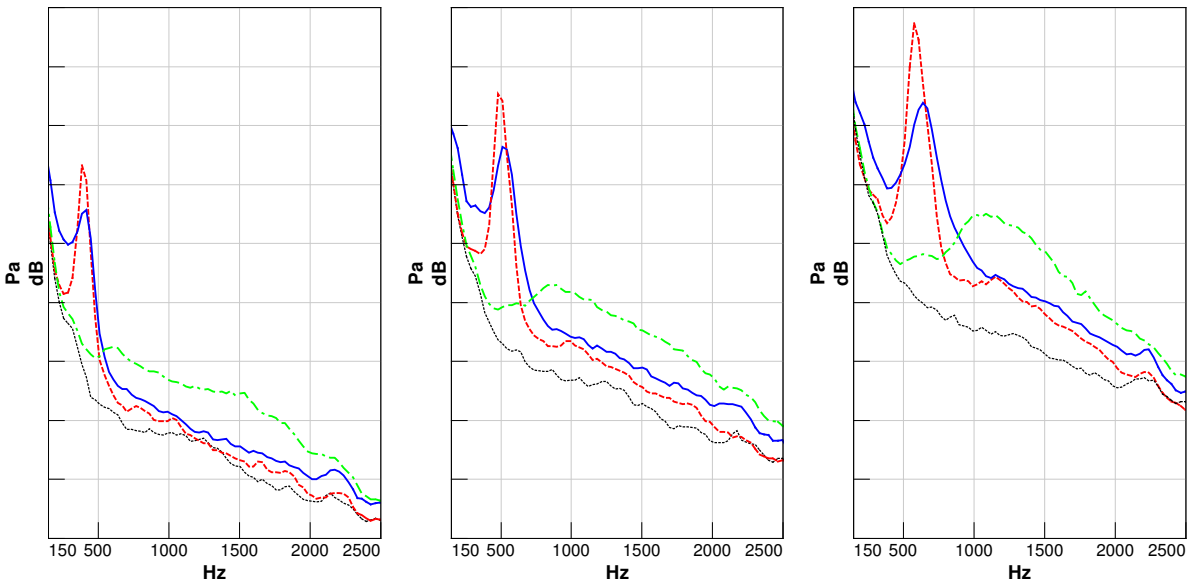

Figure 3.19: Trailing edge bluntness variation.
Exterior SPL [Grid = 5 dB], Frequency range: 0.15 – 2.5kHz.
Wind speeds: 80km/h (*left*), 100km/h (*center*), 120km/h (*right*).
--- Blunt TE, — Elliptical TE, —· Thin TE, ··· No bar.

Figure 3.22 compares the noise from the elliptical cylinder with blunt and thin trailing edges to the circular cylinder and NACA 0012, respectively. The blunt trailing edge tones are lower in amplitude and grow proportionally to the circular cylinder tones. The broadband noise from the blunt trailing edge is also lower in amplitude than the circular cylinder noise. Data suggests that those are effects from increasing chord and reducing the aspect ratio ($AR = \frac{thickness}{chord}$) of an elliptical or similar profile, i.e. main tones decrease in amplitude and increase in frequency with the increase in chord, and the broadband noise is also inversely proportional to chord length. The comparison of the

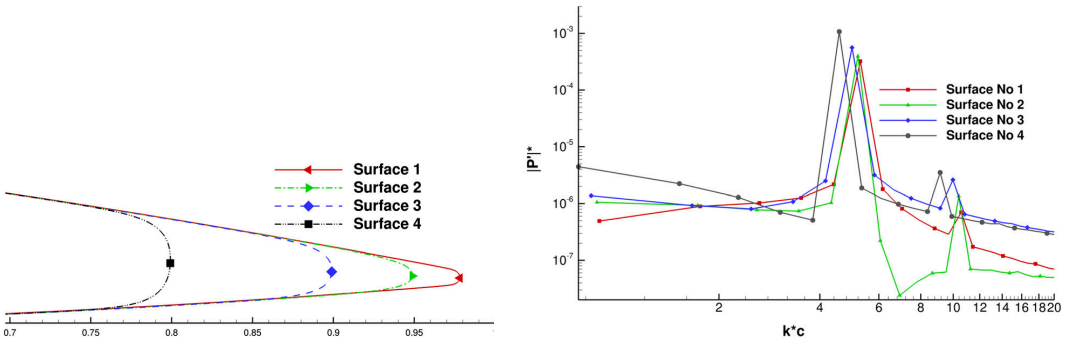

(a) Different TE bluntness. (b) Noise spectra at $M_\infty = 0.5$.

Figure 3.20: Non-dimensional acoustic pressure spectra at $M_\infty = 0.5$, adapted from Ramirez and Wolf (2016).

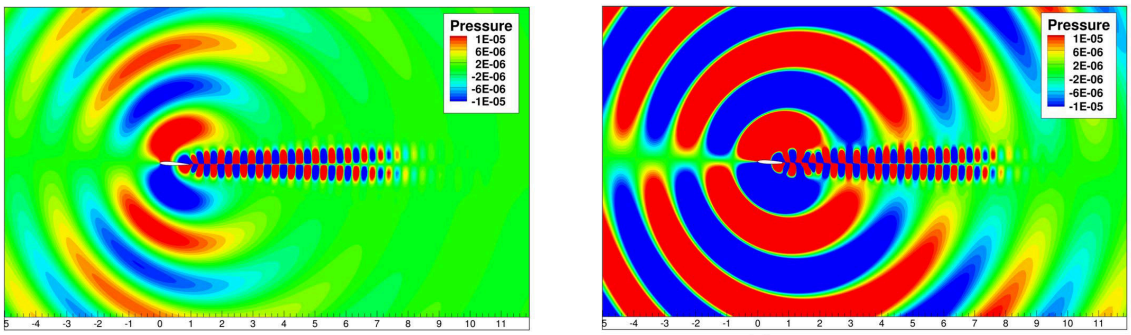

(a) Surface 1 (Thin TE). (b) Surface 4 (Blunt TE).

Figure 3.21: NACA 0012 Acoustic pressure contours at vortex shedding frequency, adapted from Ramirez and Wolf (2016).

thin trailing edge elliptical profile with the NACA 0012 is also revealing. The spectra are reasonably similar until 1kHz when the thin trailing edge profile starts generating higher amplitude broadband noise, which means the energy of the quadrupole sources that generate broadband noise is directly affected by the taper angle of the profile, i.e. the lower the angle, the smaller the thickness between upper and lower separation and consequently the lower the broadband noise.

From the receiver perspective (Figure 3.23), the thin trailing edge crossbar noise is barely noticed in this particular vehicle. Its broadband noise contribution, which starts at 500Hz and 1kHz for the vehicle speeds of 80km/h and 120km/h and ranges up to 3kHz, is mostly attenuated or reflected in the path. With respect to practical engineering applications, tapering the trailing edge of elliptical or other blunt profiles is promising in terms of tonal noise suppression. For vehicle applications, the profile curvature radius is limited by United Nations ECE (UNECE) Regulation No. 26, which defines the criteria for exterior protruding surfaces.

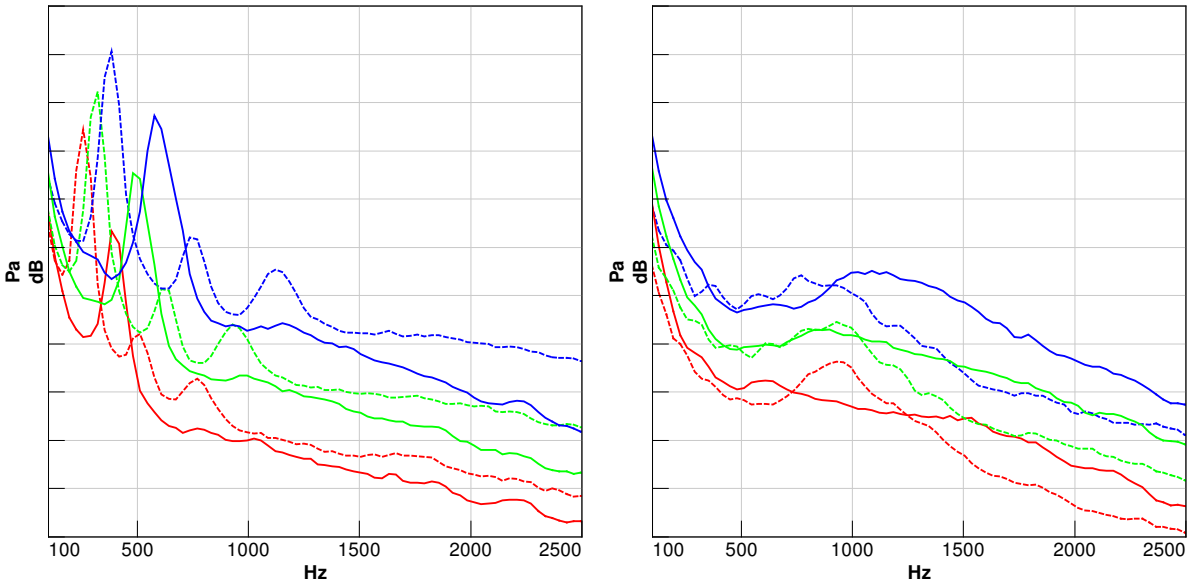

Figure 3.22: Thin and Blunt TE compared to reference profiles.
Exterior SPL [Grid = 5 dB], Frequency range: 0.1 – 2.5kHz.
Left: — Blunt TE & --- Circular cylinder, *Right:* — Thin TE & --- NACA 0012.
Wind speeds: — 80km/h, — 100km/h, — 120km/h.

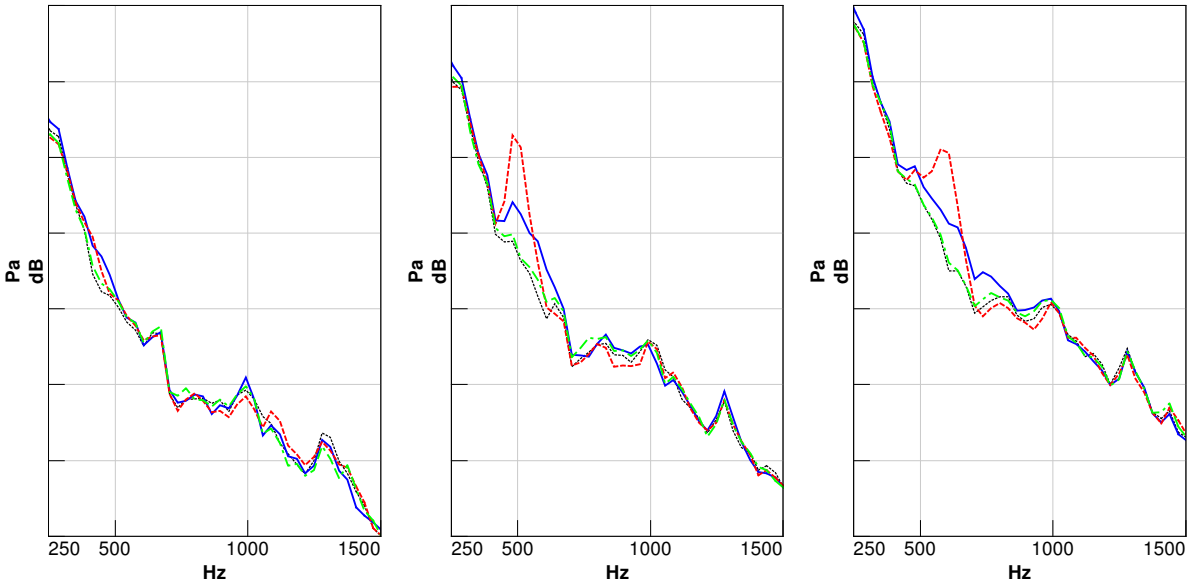

Figure 3.23: Trailing edge bluntness variation.
Interior SPL [Grid = 5 dB], Frequency range: 0.25 – 1.5kHz.
Wind speeds: 80km/h (*left*), 100km/h (*center*), 120km/h (*right*).
--- Blunt TE, — Elliptical TE, —· Thin TE, ··· No bar.

3.3.2 Trailing Edge Asymmetry

Different upper and lower trailing edge bluntnesses were also tested (Figure 3.24) and plotted along with the symmetric thin and blunt trailing edge profiles (Figure 3.25). Upper-only thin trailing edge was capable to reduce the main tone intensity significantly in all airflow speeds, with the advantage of generating less broadband noise than the symmetric thin trailing edge. Interestingly, the lower-only blunt trailing edge also reduced the main tone intensity at 80km/h and 100km/h in reference to the elliptical trailing edge, in opposite to the symmetric blunt trailing edge behavior i.e. increasing noise. Those results indicate asymmetry at the trailing edge changes the boundary layer separation dynamics and vortex periodicity, thus reducing the dipole source strength and the main tone intensity.

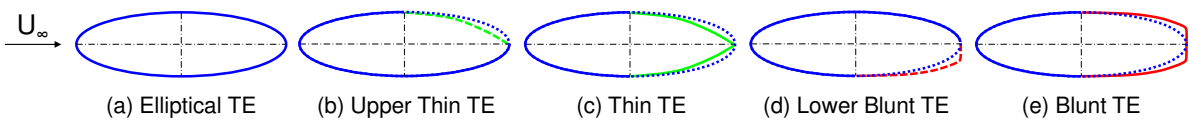

Figure 3.24: Asymmetric trailing edge 2D sections.

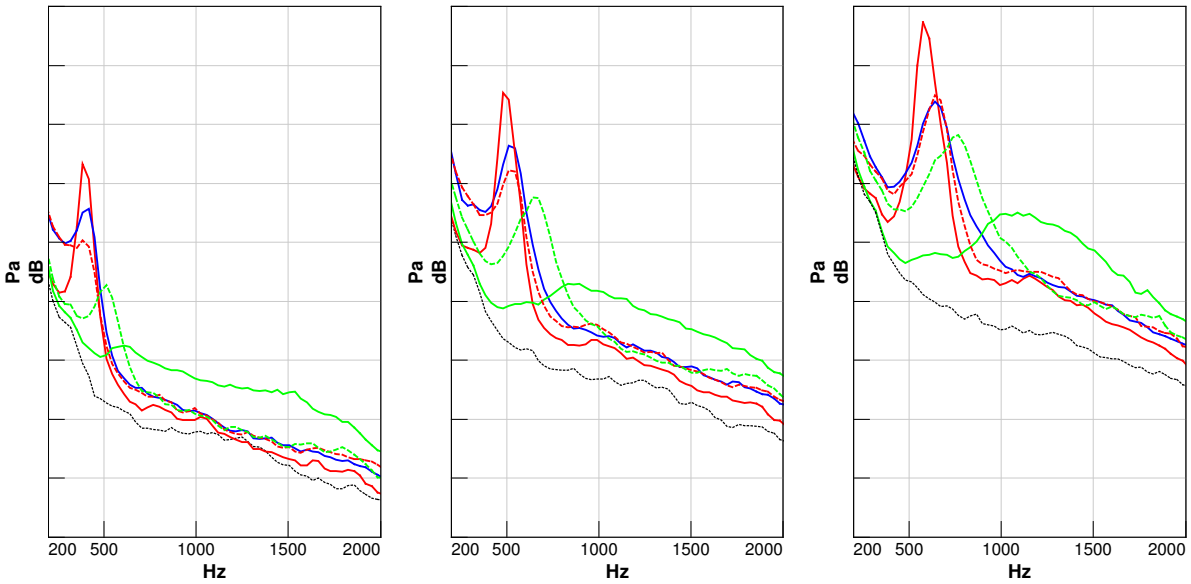

Figure 3.25: Asymmetric trailing edges.
Exterior SPL [Grid = 5 dB], Frequency range: 0.2 – 2kHz.
Wind speeds: 80km/h (*left*), 100km/h (*center*), 120km/h (*right*).
— Ellip. TE, --- Upr.Thin TE, — Thin TE, --- Lwr.Blunt TE, — Blunt TE, ··· No bar.

3.3.3 Leading Edge Bluntness

Figure 3.26 shows the different leading edge 2D sections tested. The sections and parts are the same as in Figures 3.17 and 3.18, flipped vertically during test. The trailing edge was kept elliptical for all leading edge configurations (blue line). In opposite to the results presented for the trailing edge modifications (Figure 3.19), the blunt leading edge presented the lowest noise levels in both tonal and broad bands. Tapering the leading edge did not change the tone characteristics significantly in reference to the elliptical leading edge, except for lower speeds, but did increase the broadband noise. It is proven the tonal noise originated in elliptical shapes is mostly influenced by the trailing edge bluntness, while the leading edge affects predominately the broadband noise.

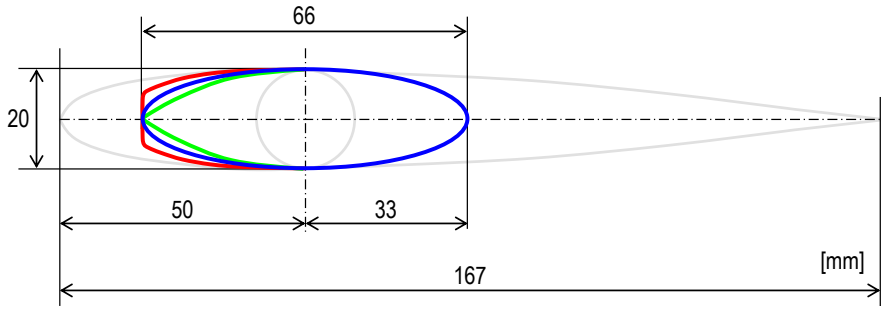

Figure 3.26: Different leading edge bluntness 2D sections.
— Blunt LE, — Elliptical LE, — Thin LE.

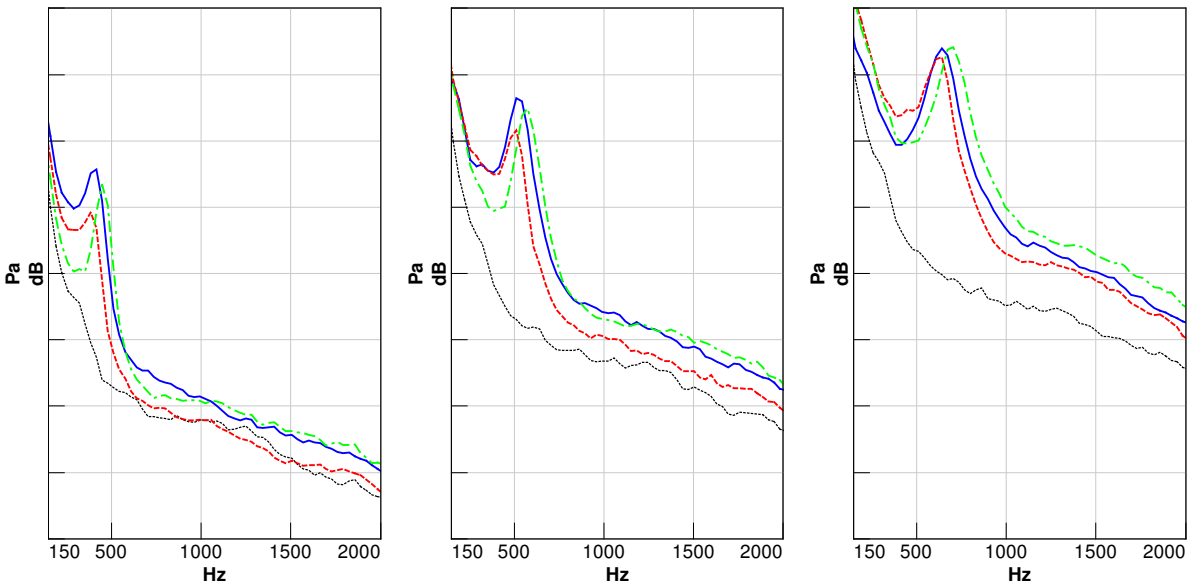

Figure 3.27: Leading edge bluntness variation.
Exterior SPL [Grid = 5 dB], Frequency range: 0.15 – 2kHz.
Wind speeds: 80km/h (*left*), 100km/h (*center*), 120km/h (*right*).
--- Blunt LE, — Elliptical LE, —· Thin LE, ··· No bar.

3.3.4 Leading Edge Asymmetry

Asymmetric leading edges did not present significant differences in both tonal and broadband noise. At 80km/h ($Re_c = 98,000$) and 100km/h ($Re_c = 123,000$), all different leading edge configurations (asymmetric, thinner and blunter radii) presented a reduction in the main tone amplitude and an increase in its frequency. At 120km/h ($Re_c = 147,000$), the tone has nearly the same characteristics for all leading edge configurations. In reference to broadband noise, partially thin leading edge (upper-only) presented same or higher levels according to R_c, while partially blunt trailing edge (lower-only) reduced broadband noise levels in all speeds.

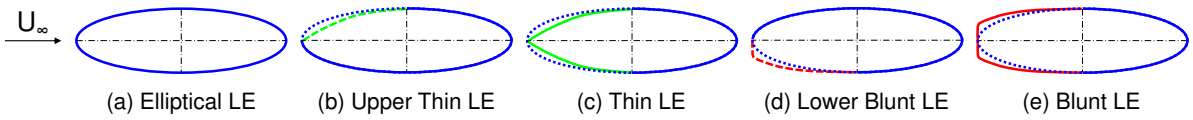

Figure 3.28: Asymmetric leading edge 2D sections.

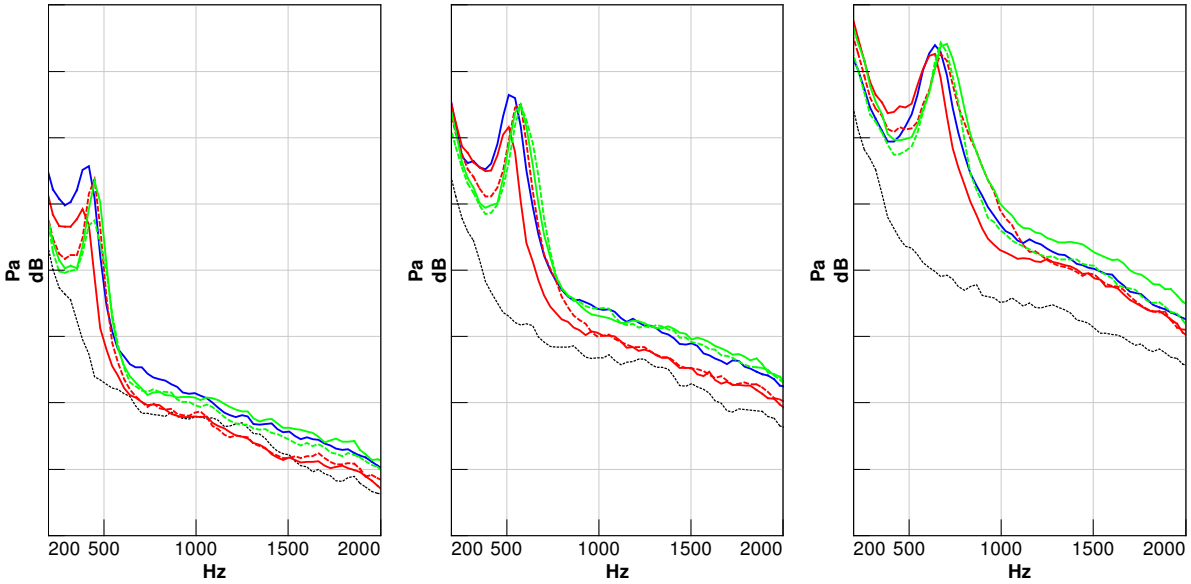

Figure 3.29: Asymmetric leading edges.
Exterior SPL [Grid = 5 dB], Frequency range: 0.2 – 2kHz.
Wind speeds: 80km/h (*left*), 100km/h (*center*), 120km/h (*right*).
— Ellip. LE, --- Upr.Thin LE, — Thin LE, --- Lwr.Blunt LE, — Blunt LE, ··· No bar.

3.3.5 Leading and Trailing Edge Asymmetry

A profile combining half-thin and half-blunt trailing and leading edges was tested in two orientations (Figure 3.30), creating two different conditions of asymmetry in reference to the roof plane. Their noise spectra differ considerably in the broadband region. Asymmetry 1 generates significantly more broadband noise than Asymmetry 2, which generates less broadband noise than the symmetric elliptical profile. Considering the profiles are identical but mirrored in x, the observed effect could be potentially related to the wake interaction with the roof. Asymmetry 1 works as an upward diffuser which accelerates the airflow underneath the profile, increases wake height in reference to the roof and generates more broadband noise. Asymmetry 2 represents a downward diffuser and generates an aeolian tone with lower pressure amplitude at 80km/h, but similar in higher speeds. Interestingly, the tone generated by Asymmetry 2 has similar levels to Asymmetry 1 (at 100km/h and 120km/h) but is not centered in a single frequency band – it presents two main frequencies that are very close to each other.

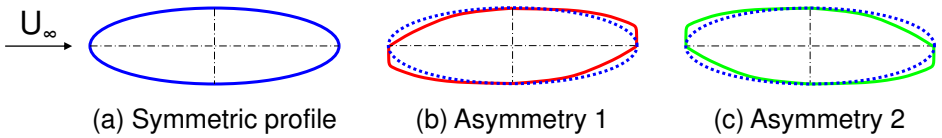

Figure 3.30: Asymmetric Leading and trailing edge 2D sections.

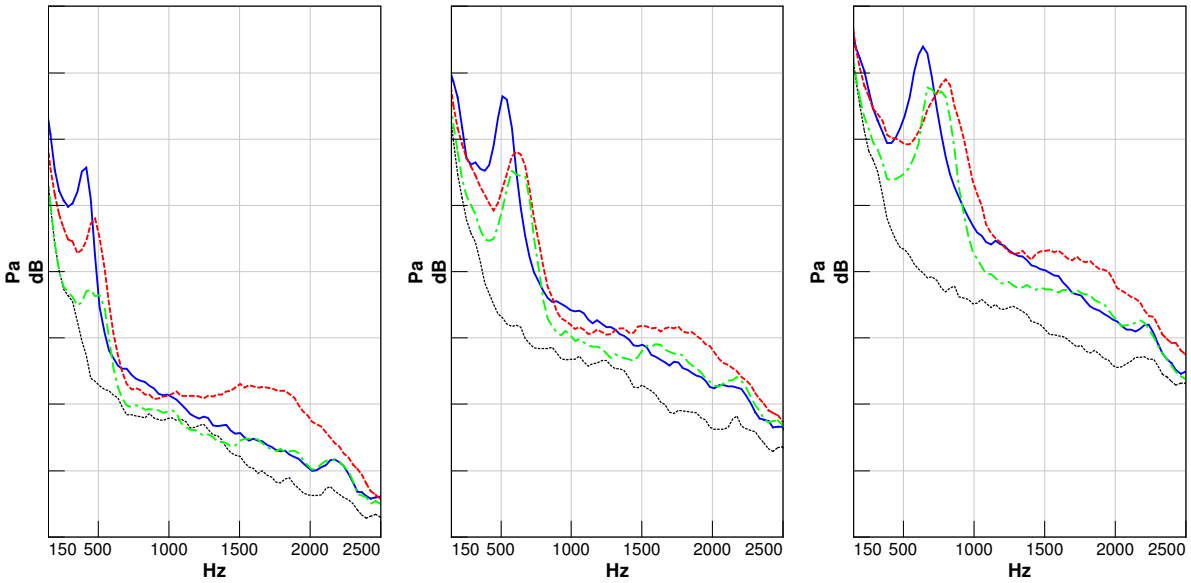

Figure 3.31: Leading and trailing edge asymmetry.
Exterior SPL [Grid = 5 dB], Frequency range: 0.15 – 2.5kHz.
Wind speeds: 80km/h (*left*), 100km/h (*center*), 120km/h (*right*).
— Symmetric ellipse, --- Asymmetry 1, —· Asymmetry 2, ··· No bar.

3.4 Angle of Attack

Applying positive and negative incidence angles to a crossbar is known as an effective empirical solution to the aeolian tone for some particular crossbar and vehicle designs. The elliptical cylinder was tested at different incidence angles, ranging from –6° (leading edge downwards) to +6° (leading edge upwards) in increments of 2° (Figure 3.32). The angles were gaged at the left and right ends of the crossbar using a goniometer as shown in Figure 3.33 (AoA = –6°, 0 and +6°). Considering the angles were not calibrated using higher precision tools, significant errors may apply between consecutive steps of 2°. Minor errors are expected between steps distant by 4° or more.

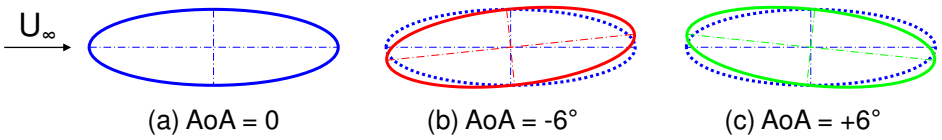

Figure 3.32: Angle of Attack variation, –6° to +6°.

(a) AoA = –6° (LE down). (b) AoA = 0. (c) AoA = +6° (LE up).

Figure 3.33: Angle of Attack goniometer gage.

Figure 3.34 shows the noise spectra for incidence angles from –6° to +6° in increments of 2°. Negative incidence angles (red lines) increase tonal noise amplitude and decrease its center frequency in lower airflow speeds. As Reynolds increases, the effect on the center frequency and amplitude of the tone is reduced, and the tone bandwidth increases. Positive incidence angles show an opposite trend. At lower speeds, the tone switches to higher frequencies and is nearly suppressed for an angle of +6° (9 dB reduction from AoA = 0 to +6°). The same effect is observed at higher speeds, but with a lower displacement of the center frequency and effect on amplitude. Positive angles also tend to narrow tone's bandwidth down. At 120km/h, the amplitude reduction is the order of 5 dB, against 9 dB at 80km/h. Figure 3.35 brings only the conditions of –6°, 0 and +6° to elucidate the AoA effects on the tonal noise amplitude, frequency and bandwidth. In conclusion, negative incidence angles significantly increase tonal noise amplitude and bandwidth and reduce its

center frequency, what is totally undesired. In contrast, positive incidence angles reduce tone amplitude and bandwidth and increase its center frequency. An angle of +6° was capable to completely eliminate the tone at 80km/h, but it was not as effective in higher speeds. Figure 3.36 plots the noise spectra at the receiver location. It is possible to see the positive Angle of Attack of +6° is a very effective solution at 80km/h, where the noise is brought down to the levels of the No-bar condition. At 120km/h, however, an incremental noise is observed at the 0.9kHz region, still lower than for AoA = 0.

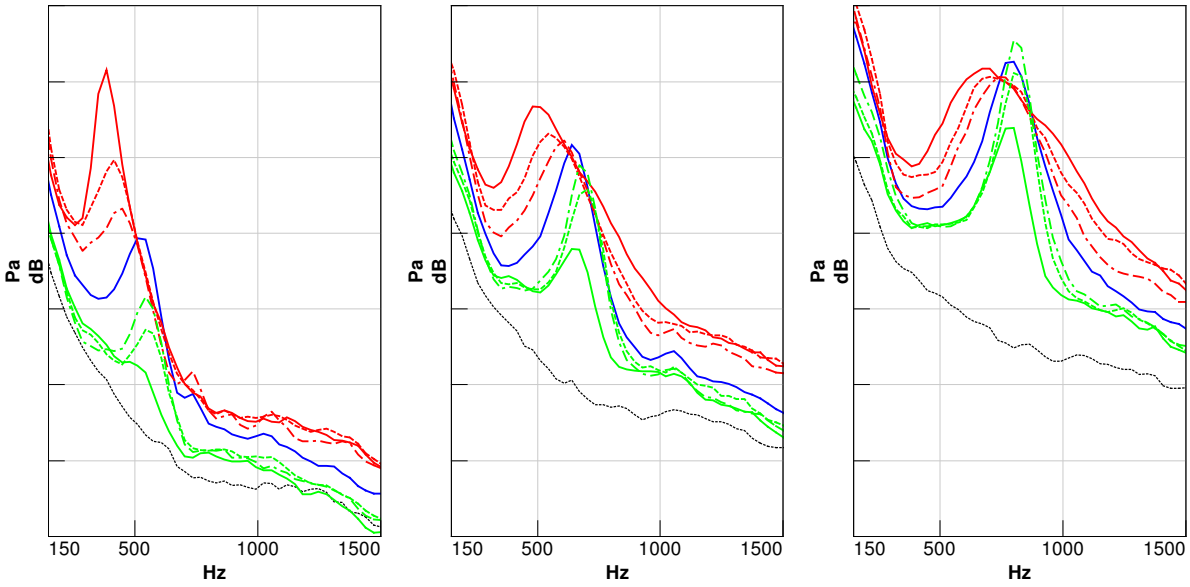

Figure 3.34: Angle of Attack variation, –6° to +6° ($\Delta\alpha$=2°).
Exterior SPL [Grid = 5 dB], Frequency range: 0.15 – 1.5kHz.
Wind speeds: 80km/h (*left*), 100km/h (*center*), 120km/h (*right*).
— –6°, --- –4°, —· –2°, — 0°, —· +2°, --- +4°, — +6°, ··· No bar.

Figure 3.37 reveals the same noise spectra from Figure 3.34 but up to 3kHz to give rise to broadband effects. The broadband noise trend above 1kHz is very clear. Negative incidence angles increased broadband noise while positive incidence angles reduced. Figure 3.38 brings only the conditions of –6°, 0 and +6° to elucidate the AoA effects on the broadband noise.

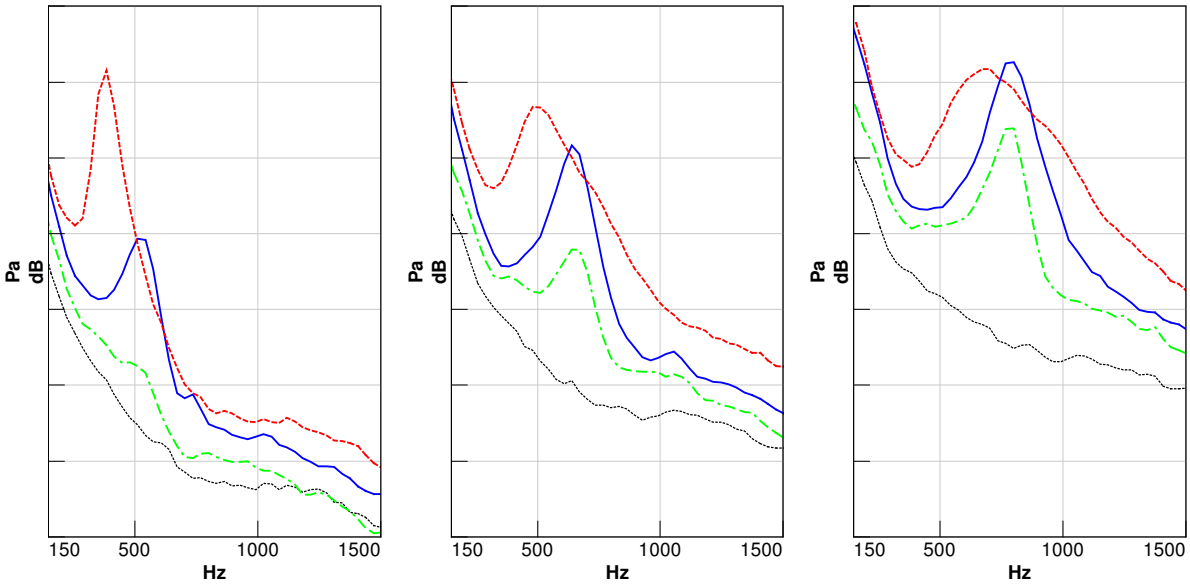

Figure 3.35: Angle of Attack variation, –6° and +6°.
Exterior SPL [Grid = 5 dB], Frequency range: 0.15 – 1.5kHz.
Wind speeds: 80km/h (*left*), 100km/h (*center*), 120km/h (*right*).
--- –6°, — 0°, —· +6°, ··· No bar.

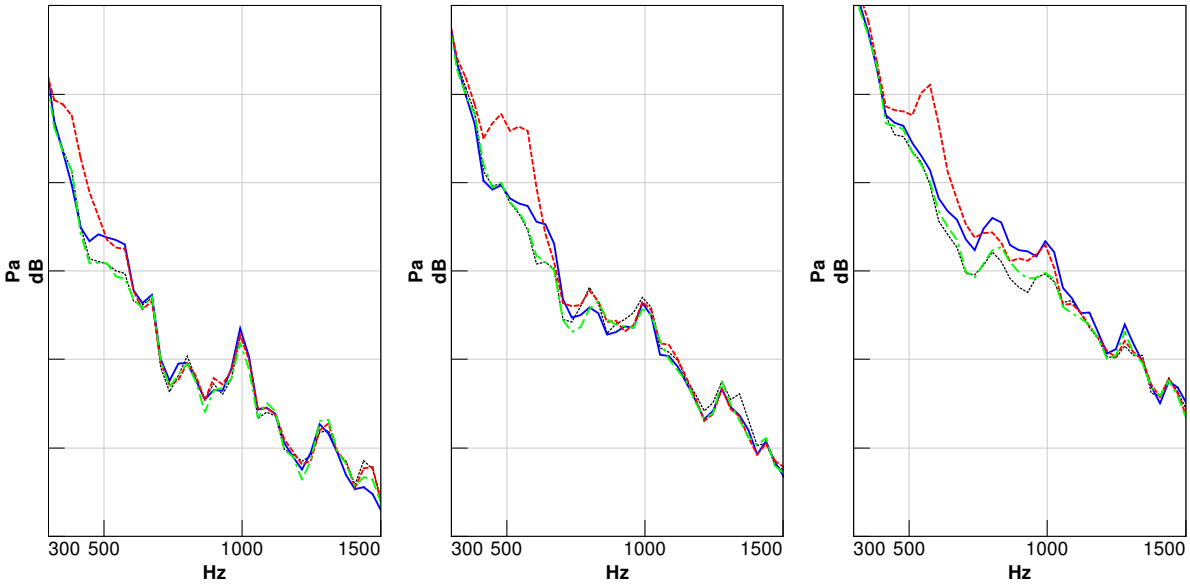

Figure 3.36: Angle of Attack variation, –6° and +6°.
Interior SPL [Grid = 5 dB], Frequency range: 0.3 – 1.5kHz.
Wind speeds: 80km/h (*left*), 100km/h (*center*), 120km/h (*right*).
--- –6°, — 0°, —· +6°, ··· No bar.

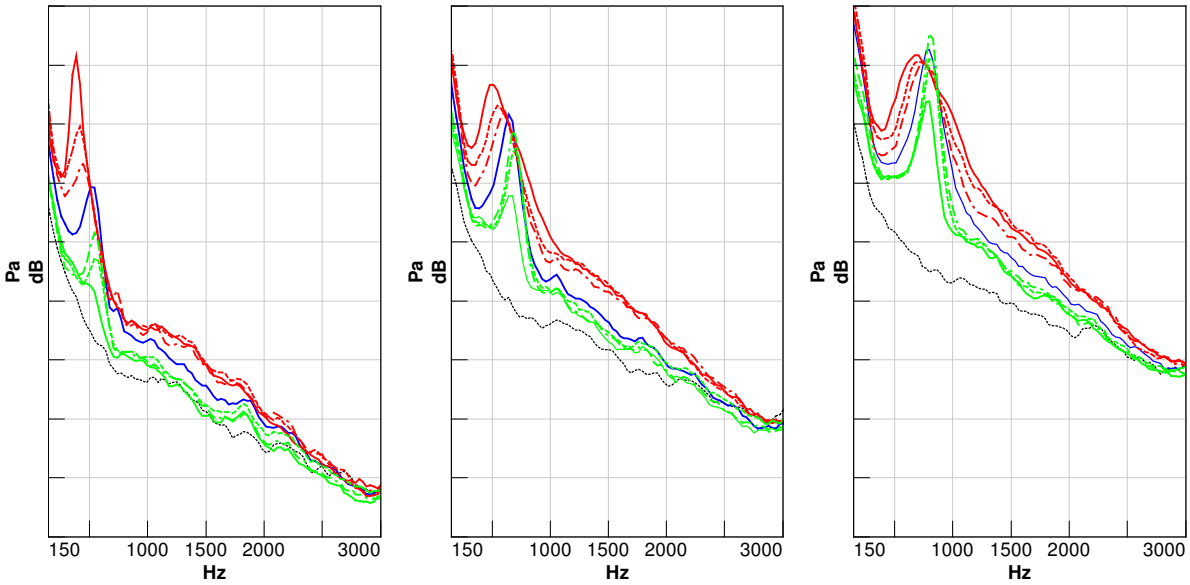

Figure 3.37: Angle of Attack variation, –6° to +6° ($\Delta\alpha$=2°).
Exterior SPL [Grid = 5 dB], Frequency range: 0.15 – 3kHz.
Wind speeds: 80km/h (*left*), 100km/h (*center*), 120km/h (*right*).
— –6°, --- –4°, —· –2°, — 0°, —· +2°, --- +4°, — +6°, ··· No bar.

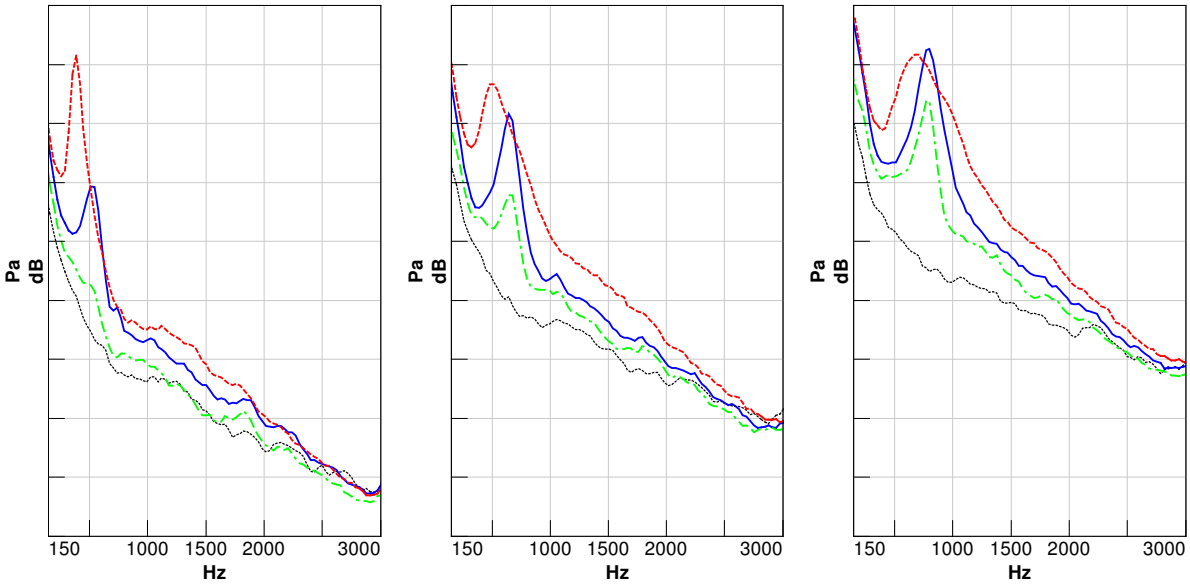

Figure 3.38: Angle of Attack variation, –6° and +6°.
Exterior SPL [Grid = 5 dB], Frequency range: 0.15 – 3kHz.
Wind speeds: 80km/h (*left*), 100km/h (*center*), 120km/h (*right*).
--- –6°, — 0°, —· +6°, ··· No bar.

Data suggests the opposite narrow and broadband noise behavior presented by negative and positive incidence angles is potentially related to ground effect. It is also plausible to assume the effects are opposite once data is taken uniquely at the suction side of the profile. In this case, negative and positive angles results would correlate with measurements taken at both suction and pressure sides of the profile, which could only be tested and analyzed in the free sound field domain of an aeroacoustic wind tunnel.

In order to verify how the ground is affecting the near wake, local flow visualization was performed at different incidence angles (–5° and +5°). Figures 3.39 and 3.40 show snapshots of the tufts motion at the speeds of 80km/h and 120km/h respectively. In both airflow speeds, the movement of the tufts located at center of the upper side of the crossbar is chaotic for AoA = +5°, while those same tufts are static for AoA = –5°, indicating the upper boundary layer separation starts earlier at +5° than –5°, as expected.

The motion of the tufts placed at the crossbar trailing edge is also more frenetic (higher frequency) at +5° than those at –5°, whereas their motion presents larger vertical amplitude and lower speed (lower frequency). Those observations agree with the noise data presented in Figure 3.34, i.e. for positive Angles of Attack, higher frequency and lower amplitude tones are expected (directly correlated to the main vortex shedding frequency), while for negative incidence angles, higher amplitude and lower frequency tones are expected.

It was also noticed the roof tufts past the crossbar present larger lateral motion at –5° than at +5°, in both airflow speeds (that effect is better visualized at 80km/h). That observation is coherent to the broadband noise data from Figure 3.37. At –5°, the wake height is larger (higher broadband noise) and meets the roof boundary layer earlier than at +5°, in despite of the intuitive thinking that a positive Angle of Attack would promote earlier wake interaction to roof. The wake interaction for various Reynolds conditions is proven by Cavalheiro *et. al* (2016) and was previously discussed at Section 3.1.

Figure 3.41 shows the streamlines of an elliptical cylinder at Angles of Attack ranging from 0° to +6° in steps of 2°, obtained via Particle Image Velocimetry (PIV) by Kwon and Park (2005). The Reynolds number is 300,000. The near-wake structure at AoA = 0° is characterized by an almost-symmetric and highly periodic dual vortex which rotation centers are located close to the trailing edge surface. As the Angle of Attack increases, the dual vortex looses its vertical symmetry and the eddy formed upstream of the trailing edge remains closer to the trailing edge surface than the downstream eddy, which has nearly no interaction with the trailing edge surface. In fact, as shown in Figure 3.42, both eddies hold off the trailing edge with the increase in Angle of Attack, what could possibly explain the tonal noise amplitude and bandwidth reduction. It is also noticed in Figure 3.41 that, as the Angle of Attack increases, the boundary layer separation point

on the suction side moves toward the trailing edge, while the separation point on the pressure side remains fixed. This delayed boundary layer separation and consequently asymmetric flow behavior alters the surface pressure distribution and the wake thickness, thus reducing broadband noise.

(a) AoA = +5° (Leading Edge upwards) (b) AoA = -5° (Leading Edge downwards)

Figure 3.39: Roof flow visualization at 80km/h (AoA = ±5°).

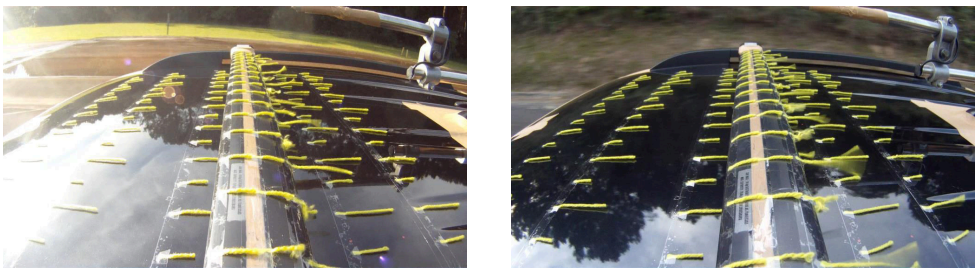

(a) AoA = +5° (Leading Edge upwards) (b) AoA = -5° (Leading Edge downwards)

Figure 3.40: Roof flow visualization at 120km/h (AoA = ±5°).

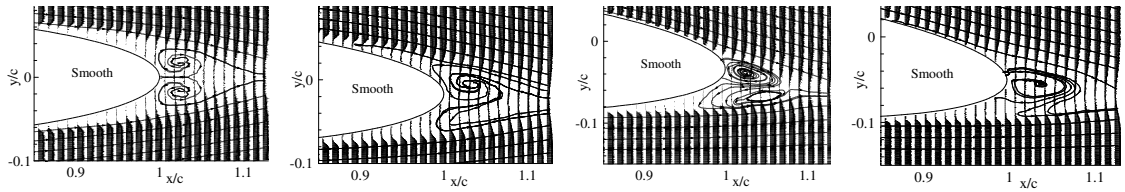

(a) AoA=0°. (b) AoA=+2°. (c) AoA=+4°. (d) AoA=+6°.

Figure 3.41: Streamlines around elliptical cylinder at different Angles of Attack. $Re_c = 300,000$, adapted from Kwon and Park (2005).

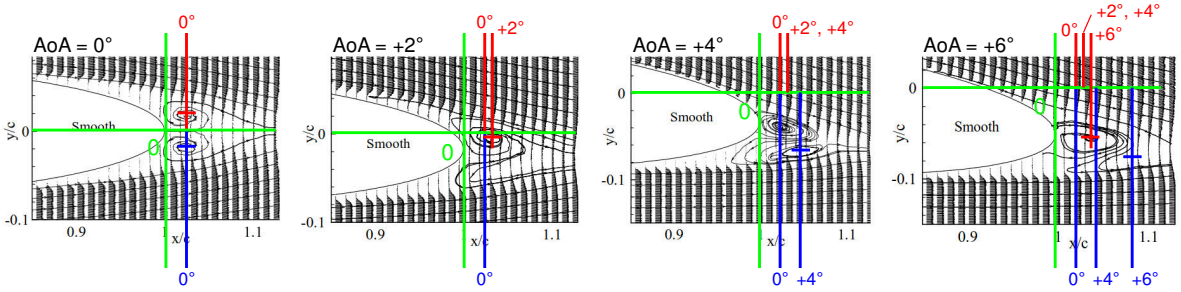

Figure 3.42: Vortex locations around an elliptical cylinder at different Angles of Attack. $Re_c = 300,000$, adapted from Kwon and Park (2005).

4 NOISE CONTROL TECHNIQUES

4.1 Boundary Layer Tripping (BLT)

Boundary Layer Tripping devices, also known as Turbulators or Vortex Generators (VG), are canonical aerodynamic solutions mostly used in the Unmanned Aerial Vehicles (UAV) industry for boundary layer control and aerodynamic stability in low Reynolds regimes, as well as in wind and turbomachinery applications as a measure to reduce aerodynamic drag and noise produced by the turbulent flow over the trailing edge of rotor blades (Winkler *et. al* (2009)), Figure 4.1). Boundary Layer Tripping technique is also used in wind tunnel tests to simulate full scale or high Reynolds number flows in low Reynolds number airfoils (Gopalarathnam *et. al* (2003)). Santhanakrishnan and Jacob (2005) foresee a promising application of Boundary Layer Tripping in Micro Aerial Vehicles (MAV) for defense purposes, as well as in the aerospace industry, due to the characteristic small airfoil aspect ratios and low Reynolds regimes ($Re_c < 500,000$). Such flow regimes are similar to the airflow around automotive crossbars ($80,000 < Re_c < 300,000$), what makes the use of Boundary Layer Tripping a promising solution in this field. In fact, nearly all of the industry-known solutions to mitigate automotive crossbar noise are based on different types of Boundary Layer Tripping, as it will be demonstrated in upcoming sections (Figures 4.2, 4.3, 4.6, and many other examples).

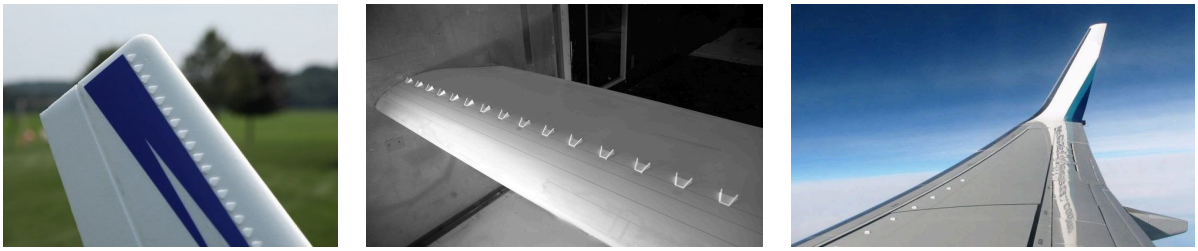

(a) UAV wing. (b) Wind turbine blade. (c) Commercial aviation.

Figure 4.1: Boundary Layer Tripping applications.

4.1.1 Aerodynamics of Boundary Layer Tripping (BLT)

Surface perturbations are capable of inducing an earlier boundary layer transition than on a free surface once they generate disturbances in the form of eddies and vortices which modify the velocity profile within the boundary layer so that it is rendered more unstable and resistant to flow separation (Gupta (2013)), improving aerodynamic stability and delaying stall. At the Reynolds regime of interest ($80,000 < Re_c < 300,000$), the highly viscous flow is laminar, and the largest contribution to the total drag is from the pressure or form drag component (or "bubble" drag), which arises due to the viscous influence of the boundary layer on the primarily inviscid pressure field. As the flow separates, the main vortices develop and the form drag increases drastically, and the primary solution for drag reduction lies in the development of efficient methods for controlling flow separation (Santhanakrishnan and Jacob (2005)).

Boundary Layer trips are able to completely eliminate or at least reduce the intensity of the laminar bubble, so they are often used to improve the aerodynamics performance of an airfoil that has a large bubble drag in the clean configuration (Gopalarathnam *et. al* (2003)). Some authors support Boundary Layer Tripping does not hold a clear advantage over airfoils designed for optimum performance in clean condition (Lyon *et. al* (1997)). Improvements in drag may be compromised by a small but noticeable loss in lift performance (Gopalarathnam *et. al* (2003)).

Turbulence promoting devices range from passive actuation trough mechanical elements (stair-steps, rounded bumps, ramps, roughness, grooves, trip wires, zigzag tapes or serrations), to active methods such as jets, deployable spoilers, acoustic excitation or surface vibration (Santhanakrishnan and Jacob (2005) and Chrusciel (1997)). The countless combinations of tripping geometries, sizes and locations relative to the airfoil chord are daunting, and a particular configuration optimized for one airfoil at a specific Reynolds number may prove less effective in different operating conditions, resulting in a myriad of experiments on airfoils with trips (Lyon *et. al* (1997)). From the flow separation perspective, even varying the Angle of Attack can be considered a Boundary Layer tripping method. Owing to the difficulties in predicting the effects of trips even on flat plate, the use of trips on low Reynolds number airfoils has primarily relied on trial-and-error approach in wind-tunnel testing. The underlying physical processes are so complex and nonlinear that make analytical and even computational description extremely difficult (Kerho and Bragg (1997)).

4.1.2 Aeroacoustics of Boundary Layer Tripping (BLT)

Although the application of Boundary Layer Tripping is questionable for pure aerodynamics applications, it has a direct effect on the near-wake structure and may offer significant changes in the aeroacoustic performance of either thin or blunt airfoils at low Reynolds. The fluid dynamic and noise mechanisms behind this separation control methodology is not clearly understood, and a direct correlation from drag and lift effects to noise effects does not exist. The primary goal of applying perturbations on the surfaces of a rigid structure is to reduce the flow coherence at the trailing edge of the profile and consequently the intensity of the aeroacoustic sources that interact with the trailing edge surfaces and propagates do the far-field. As for pure aerodynamics purposes, the practical application of Boundary Layer Tripping towards noise reduction lies essentially on empirical methods once the tripping effectiveness is quite profile and Reynolds-dependent.

As previously mentioned, nearly all of the industry-known solutions to mitigate automotive crossbar noise are based on Boundary Layer Tripping techniques, but few data on the acoustic effects of Boundary Layer Tripping is available in the literature (Winkler *et. al* (2009)). Section 4.1.3 discusses the common industry solutions based on Boundary Layer Tripping technique, and further in this work, the following Boundary Layer Tripping methods applied on the elliptical cylinder noise were assessed:

- Two-Dimensional Outwards BLT (stair-steps)
- Two-Dimensional Inwards BLT (grooves)
- Turbulence Mesh BLT (roughness)
- Three-Dimensional BLT (tipped vanes)

4.1.3 Common Boundary Layer Tripping Industry Practices

4.1.3.1 Manufacturers A and B - Two-Dimensional Outwards BLT

Figures 4.2 and 4.3 show two examples of practical application of 2D Outwards Boundary Layer Tripping techniques in automotive roof crossbars. These manufacturers, named as A and B, advertise their noise control solutions based on common complaints from costumers who own components with uncontrolled noise performance. Manufacturer A (Figure 4.2) adopted a rubber trip inserted into the upper leading edge of the extruded profile and called it "Wind Barrier". The rubber insert is an additional component

intended to meet other design requirements, however at the trade-off of adding cost and complexity to the part. In its advertisement, the manufacturer claims "The Wind Barrier creates small swirls, forming an air cushion on the surface of the cross bar which acts as a bridge for the airstream above the T-Slot, preventing the development of noise under all driving conditions[1]". The manufacturer also highlights the trailing edge "Shape Break" as another solution, unclear whether it optimizes aerodynamic or aeroacoustic performance: "we have introduced a specially designed "Shape Break" at the trailing edge of the bar that controls the airflow in a favorable way. At the same time, the Shape Break improves the stability of the crossbar and helps to keep its weight low[2]". From the data discussed in section 3.3, we know the trailing edge geometry is directly related to the near-wake vorticity and consequently the noise behavior of the crossbar, so potentially the feature does have a positive effect on noise control. Manufacturer B (Figure 4.3) claims its product was optimized in the Wind Tunnel and has reduced "drag and noise reduced to nearly zero[3]". Zero drag and noise is quite an ambitious achievement, nevertheless the important consideration is that the crossbar shape seems to be optimized for both drag and noise performance, and three potential noise reduction solutions are identified: the 2D Outwards Boundary Layer Tripping at the upper leading edge , the trailing edge taper angle, and the trailing edge tip perturbation. Manufacturers A and B are just illustrations of two actual applications of BL Tripping in automotive crossbars. Plenty 2D Boundary Layer Tripping solutions exist worldwide.

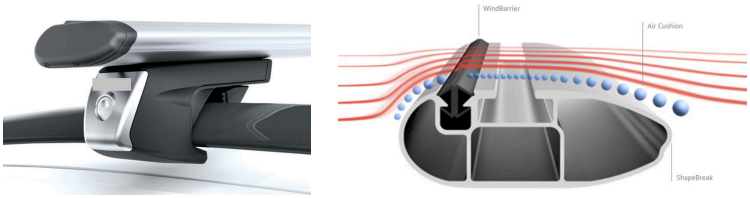

(a) Commercial part. (b) Claimed technology.

Figure 4.2: 2D Outwards Boundary Layer Tripping - Manufacturer A.

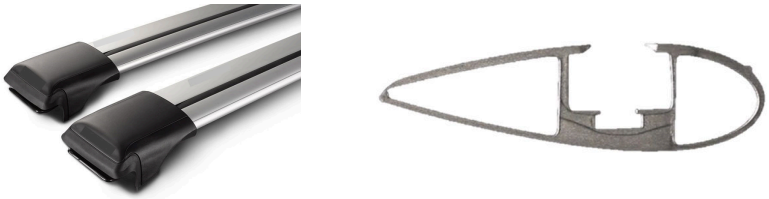

(a) Commercial part. (b) Claimed technology.

Figure 4.3: 2D Outwards Boundary Layer Tripping - Manufacturer B.

[1] http://www.atera.de/en/signo-rt-rail-roof-bars.html
[2] http://www.atera.de/en/signo-rt-rail-roof-bars.html
[3] http://www.whispbar.com/about/technology/

4.1.3.2 Manufacturer C - Two-Dimensional Inwards BLT

Figure 4.4 shows the application of 2D Inwards Boundary Layer Tripping in a commercial crossbar (Manufacturer C). The elliptical profile has grooves applied on the upper and lower leading edges. The part was tested with no grooves (clean configuration), with the upper groove only, lower groove only and with both grooves. Clay was used to fill up the grooves and reproduce the upper and lower sides in clean configuration. Figure 4.5 shows the aeroacoustic effects observed at the source (Exterior SPL) and at the receiver location (Interior SPL). In the upper plots it is clear the effectiveness of tripping at both sides instead of at one side. One can also see the grooves are not capable of eliminating the main broad tonal from the elliptical profile but attenuate its intensity and shift its center frequency to a higher value, what could be positive depending on the transmission path characteristics of the vehicle. In this specific case, the crossbar with both grooves applied have presented a satisfactory performance in terms of customer perception once the remaining incremental noise is barely noticeable from inside the cabin. The tonal noise center frequency offset to a higher value was beneficial. At 80km/h, traces of the tone are noticed inside the cabin at approximately 600Hz. As wind speed and the center frequency increases, the tone suppression also increases. At 120km/h, the tone occurs at about 0.9kHz and is barely noticed at the vehicle occupant location.

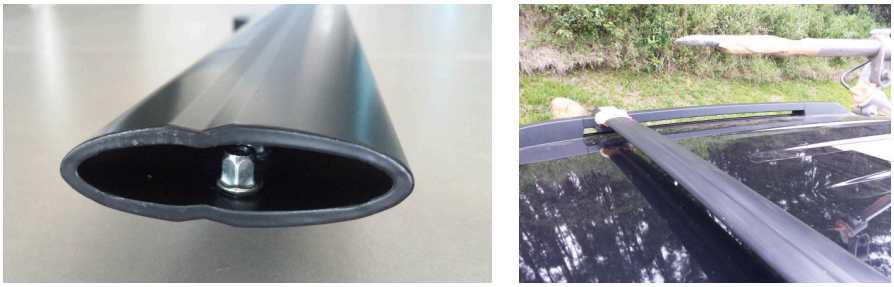

(a) Commercial profile. (b) Part test.

Figure 4.4: 2D Inwards Boundary Layer Tripping - Manufacturer C.

4.1.3.3 Manufacturers D and E - Three-Dimensional BLT

Another common solution applied in the automotive industry is the installment of a rubber insert on the upper surface of the crossbar. Similar to the serration trip, the insert has tipped vanes that change local airflow direction and promote instantaneous boundary layer transition. The rubber material also protects the crossbar and the carried goods from scratches. The solution is protected by patent. Manufacturers D and E adopt such solution (Figures 4.6 and 4.10). Manufacturer D claims its "Wind Diffuser™ technology disturbs the airflow to reduce noise and drag[4]". In addition to the rubber

[4] https://www.thule.com/en-gb/gb/roof-rack/roof-bars/thule-wingbar-960-_-960100

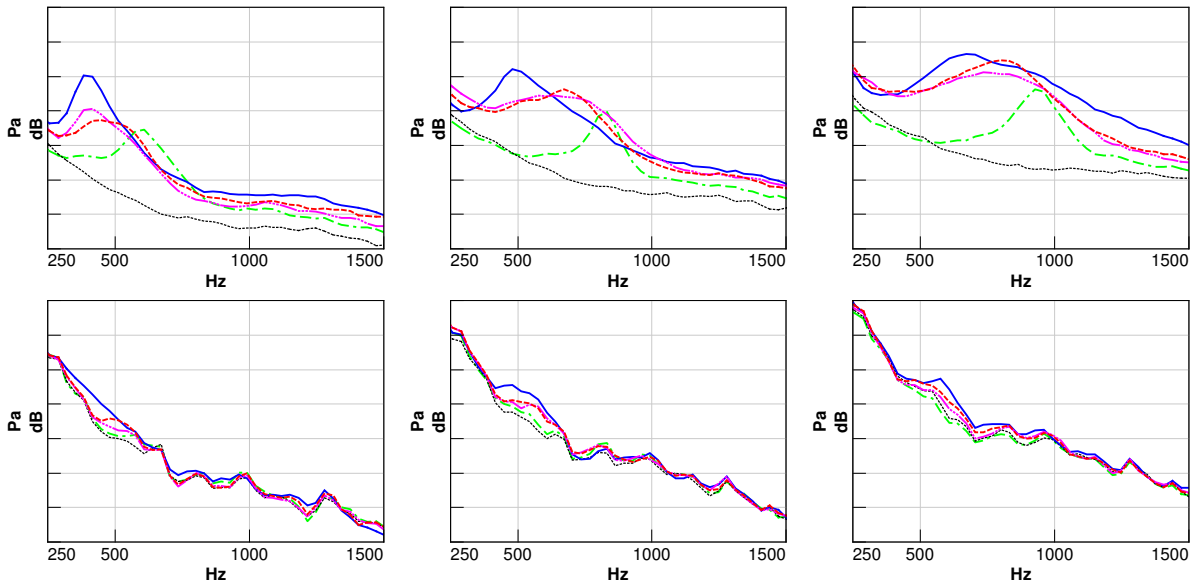

Figure 4.5: 2D Inwards Boundary Layer Tripping - Manufacturer C test.
Exterior & Interior SPL [Grid = 5 dB], Frequency range: 0.25 – 1.5kHz.
Wind speeds: 80km/h (*left*), 100km/h (*center*), 120km/h (*right*).
Microphone location: Exterior SPL (*top*), Interior SPL (*bottom*).
— No tripping, --- Upper groove, —··· Lower groove, —· Upr. & Lwr. grooves, ··· No bar.

strip, the truncated airfoil profile of Manufacturer D has two grooves on the lower side of the profile which may be affecting its aeroacoustic behavior. The effect of both features, i.e. the rubber strip and the surface grooves, were investigated (Figure 4.7). One can see in the upper plots of the Figure 4.8 that both Leading and trailing edge lower grooves are capable to reduce the main tone amplitude from approximately 2 dB at 80km/h up to 8 dB at 120km/h, as well as reduce its center frequency, what indicates the grooves force an earlier separation and the profile behaves more bluntly than in clean configuration. Even in the presence of the lower grooves, the main tone keeps its narrow bandwidth. By adding the 3D rubber strip on the upper surface of the profile (Figure 4.8 lower), the effect on tonal noise suppression is higher, i.e. over 15 dB of SPL reduction in higher speeds, added by a negative offset in the center frequency. Interestingly, summing up the effects of the 3D rubber strip with the lower 2D grooves, the intensity of the main tone increases, and its center frequency reduces furthermore. In conclusion, the intruding 2D trips must have been developed and implemented for other requirements but noise (e.g. structural resistance or manufacturing requirements).

The rubber insert does have a positive effect in the tone suppression, however it just reduces its amplitude to an acceptable level for the vehicle occupants, as demonstrated in Figure 4.9. The upper plots show the Exterior SPL data close to the source, for the tripped and untripped bar conditions, while the lower plots bring the Interior SPL of the same conditions. The tripped condition without the 2D grooves at the lower surface of

the crossbar was also plotted. As shown in Figure 4.8, the 3D strip reduces the main tone amplitude and shifts its center frequency to lower values. Without the lower 2D grooves, noise suppression would be higher. From the vehicle occupants perspective, the noise drastically reduces at the frequency of the untripped bar tone, but a residual incremental noise is noticed at the frequency of the tripped bar tone, in special at 100 and 120km/h. Without the lower grooves that increase tonal noise amplitude (Figure 4.8), the noise spectra at the occupant location would not present such residual noise. Such finding is related to this specific vehicle and the characteristics of its transmission path.

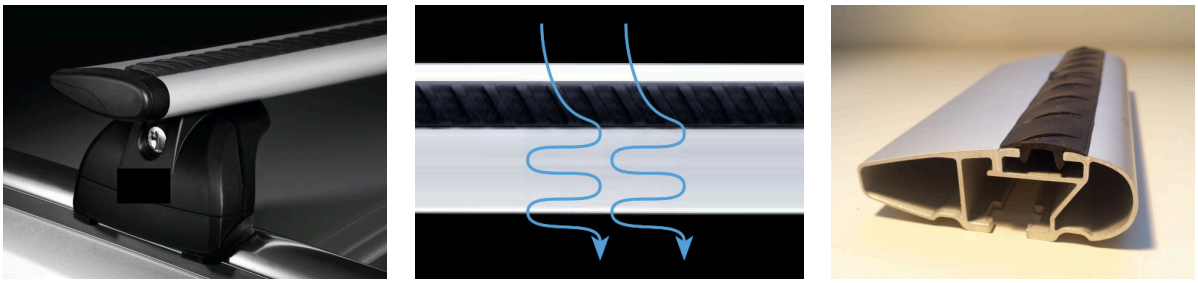

(a) Commercial part. (b) Advertised solution. (c) Crossbar profile.

Figure 4.6: 3D Boundary Layer Tripping - Manufacturer D.

(a) No grooves and tripping. (b) Lwr 2D BLT (upside-down). (c) Upper 3D BL Tripping.

Figure 4.7: 3D Boundary Layer Tripping - Manufacturer D test.

Manufacturer E adopts the tipped rubber insert on the upper surface of its irregular shaped profile (Figure 4.10). The effectiveness of the rubber insert in this type of blunt profile was investigated. A similar result to Manufacturer D is observed (Figure 4.11), but in this case the primary tone looses its narrowband characteristic, and its center frequency does not switch to a lower value. The resulting Sound Pressure Level inside the vehicle cabin is also plotted in Figure 4.11. Up to 100km/h, the residual noise increment for the vehicle occupants is negligible. At 120km/h, the incremental noise can be perceived at the 500Hz region. That observation refers to this specific vehicle and the characteristics of its transmission path.

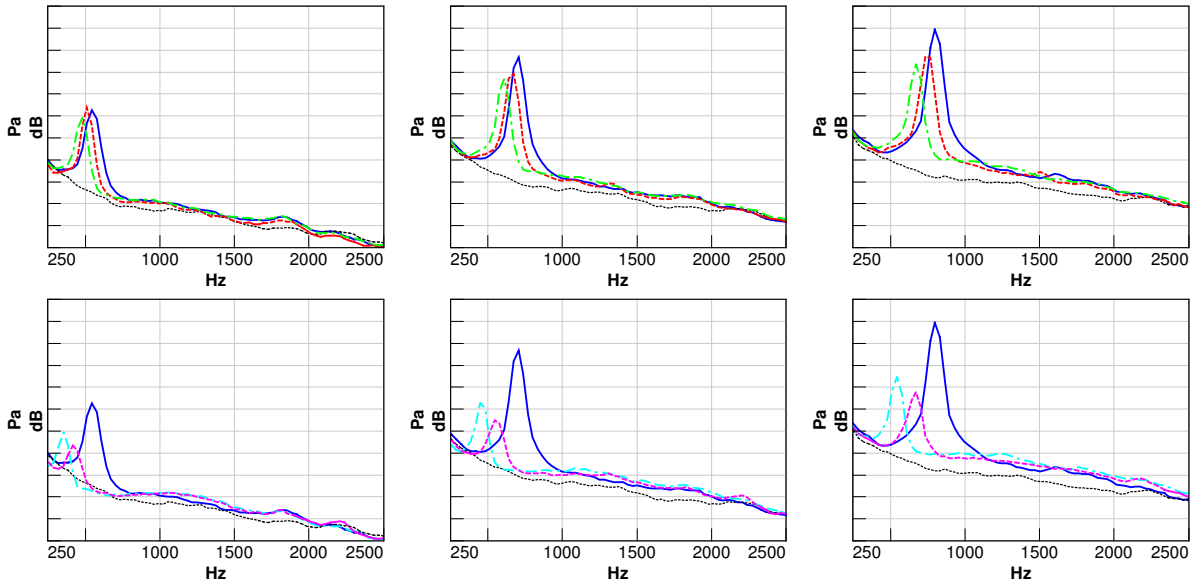

Figure 4.8: 3D Boundary Layer Tripping - Manufacturer D test.
Exterior SPL [Grid = 5 dB], Frequency range: 0.25 – 2.5kHz.
Wind speeds: 80km/h (*left*), 100km/h (*center*), 120km/h (*right*).
2D Tripping effect (*top*), 3D Tripping effect (*bottom*).
— No tripping, --- Lwr. 2D LE tripping, —· Lwr. 2D LE+TE tripping,
--- Upr. 3D tripping, —· Upr. 3D tripping + Lwr. 2D LE+TE tripping, ··· No bar.

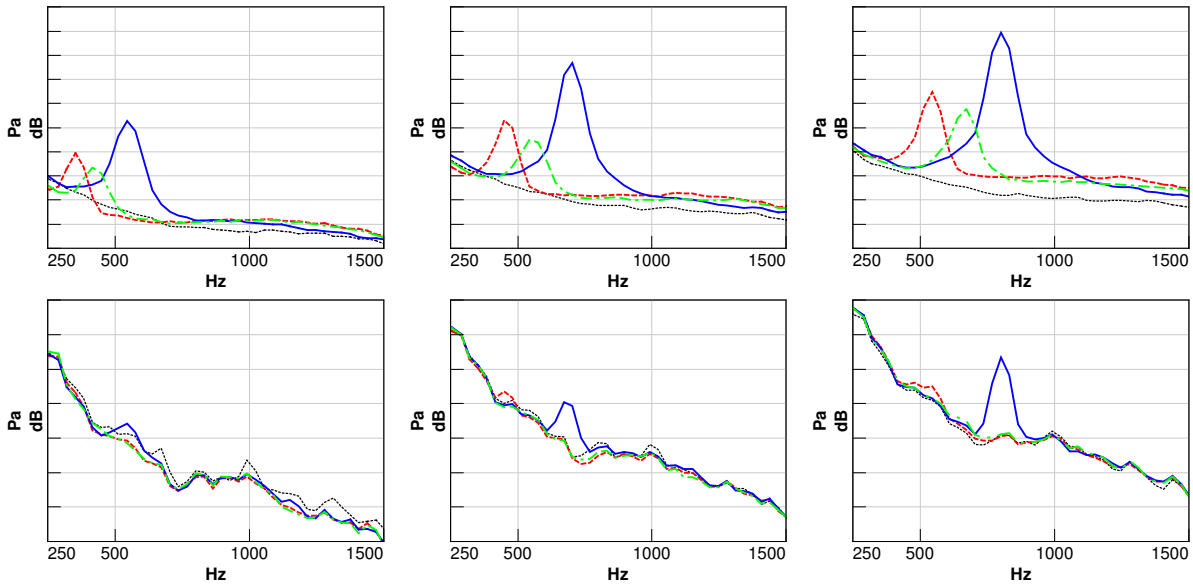

Figure 4.9: 3D Boundary Layer Tripping - Manufacturer D test.
Exterior & Interior SPL [Grid = 5 dB], Frequency range: 0.25 – 1.5kHz.
Wind speeds: 80km/h (*left*), 100km/h (*center*), 120km/h (*right*).
Microphone location: Exterior SPL (*top*), Interior SPL (*bottom*).
— No tripping, --- 3D tripping and grooves, —· 3D tripping only, ··· No bar.

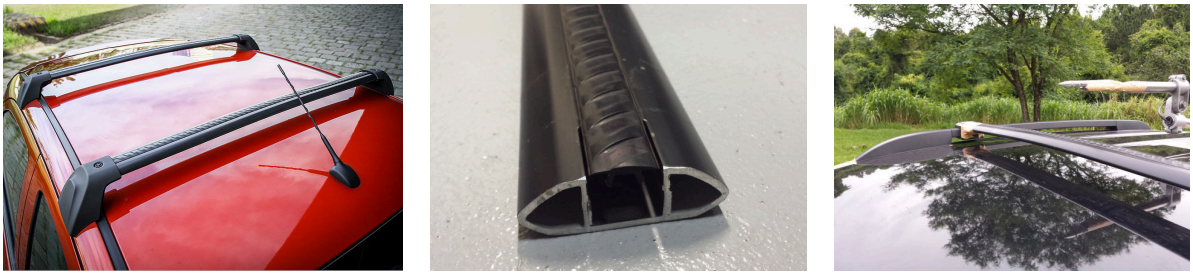

(a) Commercial part. (b) Crossbar profile. (c) Part test.

Figure 4.10: 3D Boundary Layer Tripping - Manufacturer E.

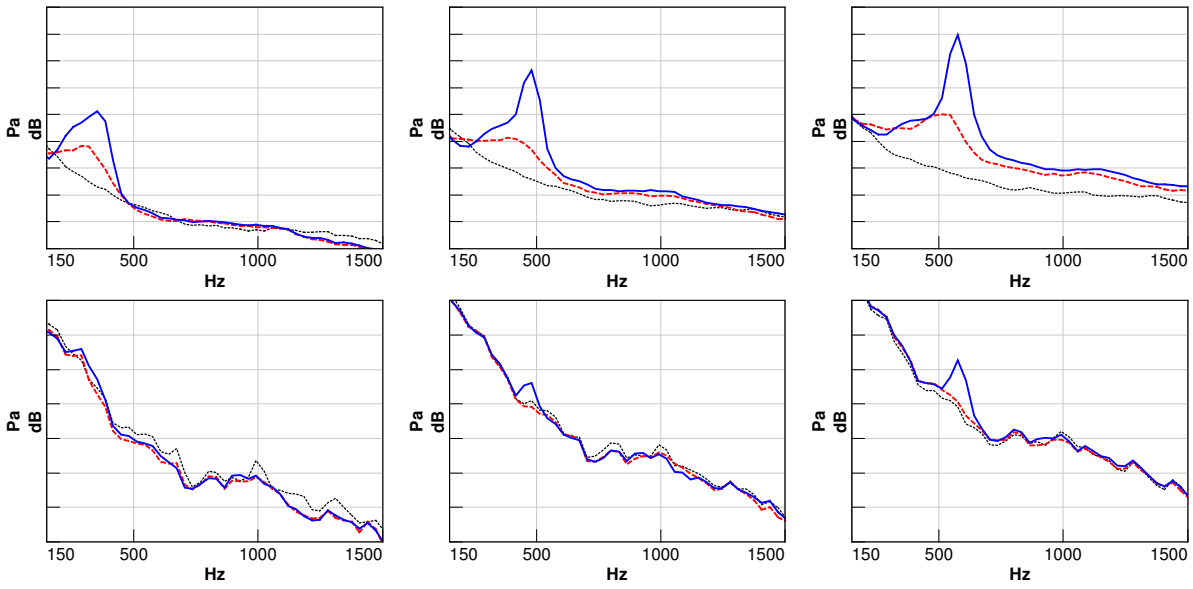

Figure 4.11: 3D Boundary Layer Tripping - Manufacturer E test.
Exterior & Interior SPL [Grid = 5 dB], Frequency range: 0.15 – 1.5kHz.
Wind speeds: 80km/h (*left*), 100km/h (*center*), 120km/h (*right*).
Microphone location: Exterior SPL (*top*), Interior SPL (*bottom*).
— No tripping, --- 3D tripping, ··· No bar.

4.1.4 Two-Dimensional Outwards BLT applied on an Elliptical Cylinder

Drag reduction by employing two-dimensional Boundary Layer Tripping was reported by Lyon *et. al* (1997), along with a rich survey of the studies performed up to that moment. The authors assessed single and multiple 2D plain (stair-steps) Boundary Layer Tripping solutions, of different heights and locations, on Reynolds numbers between 100,000 and 300,000 and in four different airfoils, focusing primarily on qualitative effects obtained by flow visualization and aerodynamic properties. Trips were located relative to the untripped laminar separation locations. Data shows dramatic drag reductions for relatively thin trips, with thicker trips having slightly better performance. The trip location proved to be of little significance for trips located upstream of laminar separation. Little advantage was seen in utilizing multiple 2D trips or complex 3D trips over single 2D trips (Lyon *et. al* (1997)).

Kwon and Park (2005) investigated the effects of Boundary Layer Tripping on the the aerodynamic characteristics of an elliptic airfoil ($AR = 0.16$) at the Reynolds number of 300,000. In addition to the measurement of aerodynamic forces and moments, the velocity field around the airfoil was surveyed by Particle Image Velocimetry (PIV). Circular trip dots were used for the trip. The diameter of the dots was 1.27mm and the height 0.29mm ($0.1c$). The dots were placed with a spacing of 1.27mm in spanwise, at 10% of the chord from the leading edge , on both sides of the airfoil surface (upper and lower leading edge BLT). The boundary layer of the smooth surface separates ahead of $x/c = 0.9$, forming reversed flow region and vortices just after the trailing edge , and the tripped condition retards the boundary layer separation down to around $x/c = 0.97$, reduces the vortex scale and the height of the far-wake (Figure 4.12). The recirculation region is also more densely packed in the tripped condition. That demonstrates the potential offered by applying Boundary Layer Tripping techniques towards tonal and broadband noise reduction. Kwon and Park (2005) also tested the effect of BL Tripping at different Angles of Attack. Vortex scale reduction is observed at $+2°$ and $+4°$, but as AoA increases further, tripping looses effectiveness. For Angles of Attack higher than $+6°$, the wake structures for the smooth airfoil and those for the tripped airfoil do not show significant differences indicating the trip effect disappears for this range of Angle of Attack.

In this study, a stair-step with 1.5mm of height ($0.075h$ and $0.02c$, similar to Santhanakrishnan and Jacob (2005)) was installed in three different positions relative to the center of the elliptical profile (before, at and after the center). Those positions were tested at both the upper and lower sides of the profile (Figures 4.13 and 4.14). The precise location where the boundary layer separates is unknown. Flow visualization with

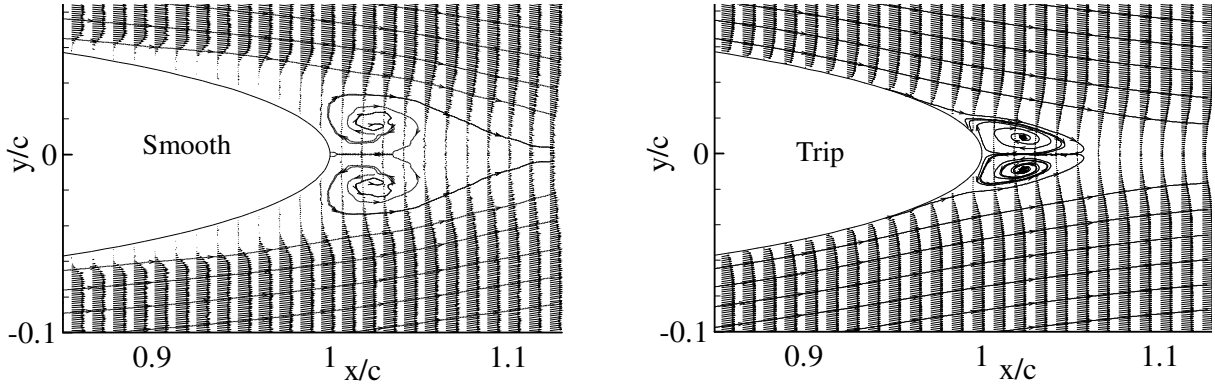

Figure 4.12: Wake vortex structure with streamlines for a smooth and tripped elliptical cylinder at AoA=0° and $Re_c = 300,000$, adapted from Kwon and Park (2005).

tufts of yarn (Figures 3.4 and 3.5) indicate the separation point at 80km/h is close to the trailing edge of the crossbar, and as wind speed increases, separation point moves forward towards the center of the crossbar. Literature indicates the optimum trip location for aerodynamics is at the leading edge , either at the pressure or suction sides, no matter at which precise x/c location it would be once it is upstream of the laminar separation point in clean condition (Lyon *et. al* (1997)). For noise applications, no data was found in the literature.

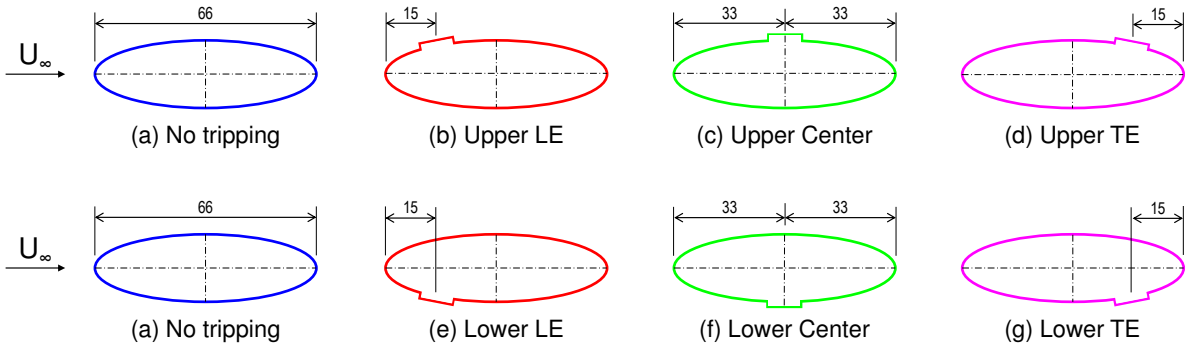

Figure 4.13: 2D Outwards Boundary Layer Tripping profiles [mm].

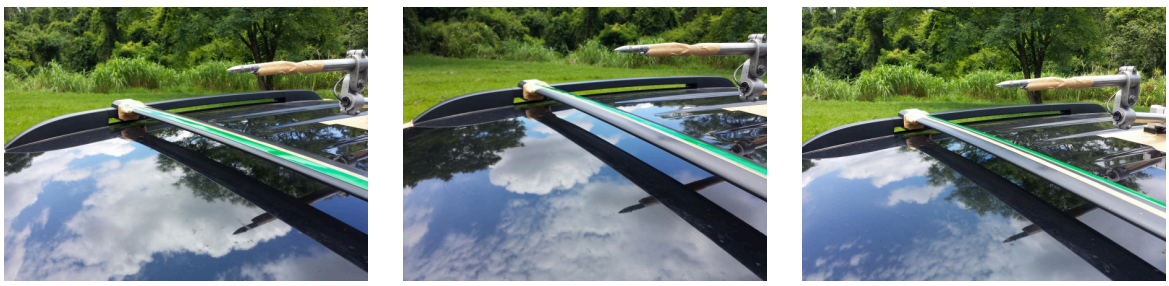

(a) Upper LE. (b) Upper Center. (c) Upper TE.

Figure 4.14: 2D Outwards Boundary Layer Tripping (upper side).

Figure 4.15 reveals the narrowband effects of 2D Outwards Boundary Layer Tripping on the elliptical cylinder crossbar. Several observations can be withdrawn from the spectral plots. To begin with, tripping at the center of the ellipse i.e. the point of maximum thickness, was capable of reducing the tonal noise intensity just in lower speeds, where the separation point is expected to be closer to the trailing edge . In higher speeds, tripping at the center increased the aeolian tone intensity and narrowed its bandwidth. The effect is well understood once tripping at the center of the profile increased total profile thickness and Aspect Ratio by 15%, and the increase in noise is expected for an increased bluntness (Figure 3.12). The strip is causing a drastic perturbation of the airflow path instead of an earlier transition of the boundary layer state to turbulent. Consequently, the center-tripped elliptical cylinder assumed the behavior of a blunter body presenting a well defined vortex structure with the primary acoustic tone at lower frequencies. Tripping at the leading and trailing edges have presented a reduction in the tone amplitude, at varying levels, in all wind speeds and at both upper and lower sides of the ellipse. In some cases the reduction was expressive, but negligible in others (e.g. tripping at the upper side at 120km/h). Tripping at the leading edge performed better than at the trailing edge in all wind speeds. In the majority of cases, tripping at the leading and trailing edges also reduced the tone bandwidth. By comparing tripping at the upper versus lower sides for all tripping locations, one can observe tripping at the lower side is more effective than at the upper side, in special in higher wind speeds where the effect of upper side tripping is essentially a reduction in the tone bandwidth with nearly no effect in amplitude. It is important to observe that, in any case, tripping did not fully eliminate the formation of a center tone, it just reduced its intensity.

Figure 4.16 shows the broadband effects of 2D Boundary Layer Tripping up to 7kHz. Tripping at the trailing edge originated high frequency tones that are totally undesired, mainly with tripping located at the upper side of the profile. Up to 2kHz, different from the narrowband observations, tripping at the upper side of the profile was more effective in reducing broadband noise at the speeds of 80 and 100km/h. At 120km/h, tripping at the lower leading edge was more effective. Above 2kHz, the noise spectra is similar for all cases, except for the trailing edge tripping which generates secondary tones.

Figure 4.17 compares the most effective 2D Outwards BLT locations, i.e. tripping at the upper and lower leading edges, up to the 3kHz frequency band. Lower LE tripping is in fact the best location looking at the tonal noise behavior, which is the most critical for the vehicle occupants. At 120km/h, upper LE tripping did not reduce the tone amplitude considerably, and the lower LE tripping was capable of reducing also the broadband noise more effectively. At 80 and 100km/h, upper LE tripping was most effective in broadband noise suppression.

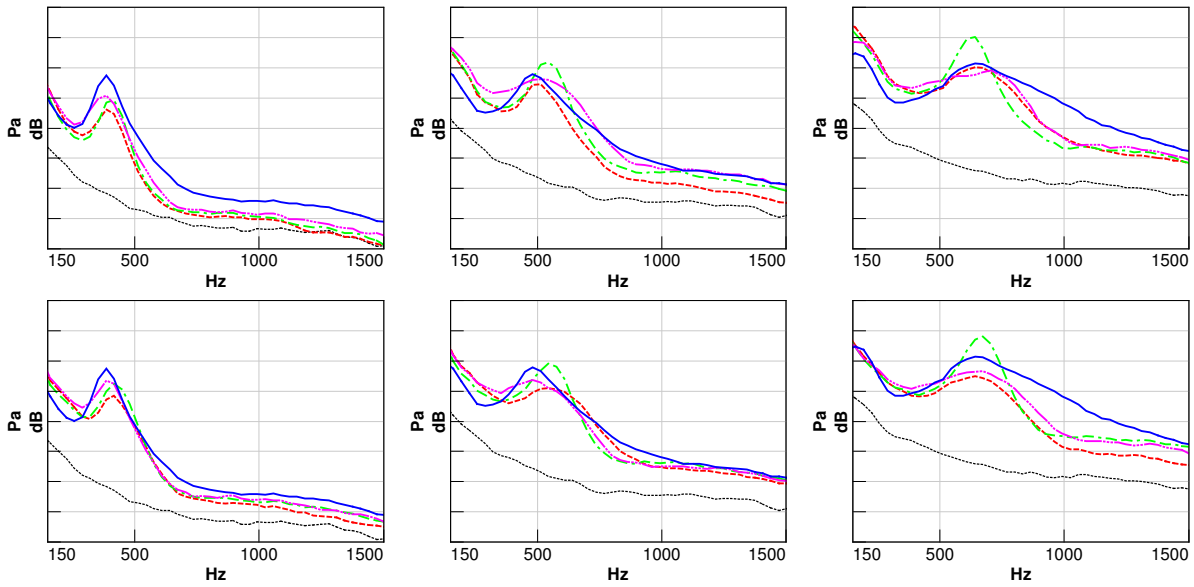

Figure 4.15: 2D Outwards Boundary Layer Tripping.
Exterior SPL [Grid = 5 dB], Frequency range: 0.15 – 1.5kHz.
Wind speeds: 80km/h (*left*), 100km/h (*center*), 120km/h (*right*).
Trip location: Upper side (*top*), Lower side (*bottom*).
— No tripping, --- Leading edge, —· Center, —··· Trailing edge, ··· No bar.

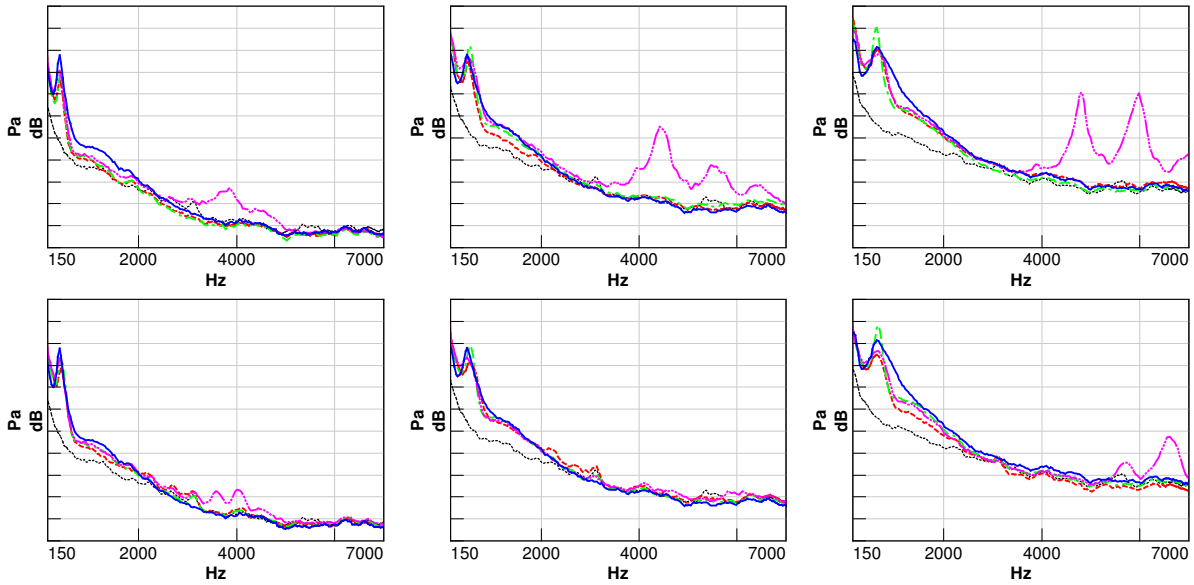

Figure 4.16: 2D Outwards Boundary Layer Tripping.
Exterior SPL [Grid = 5 dB], Frequency range: 0.15 – 7kHz.
Wind speeds: 80km/h (*left*), 100km/h (*center*), 120km/h (*right*).
Trip location: Upper side (*top*), Lower side (*bottom*).
— No tripping, --- Leading edge, —· Center, —··· Trailing edge, ··· No bar.

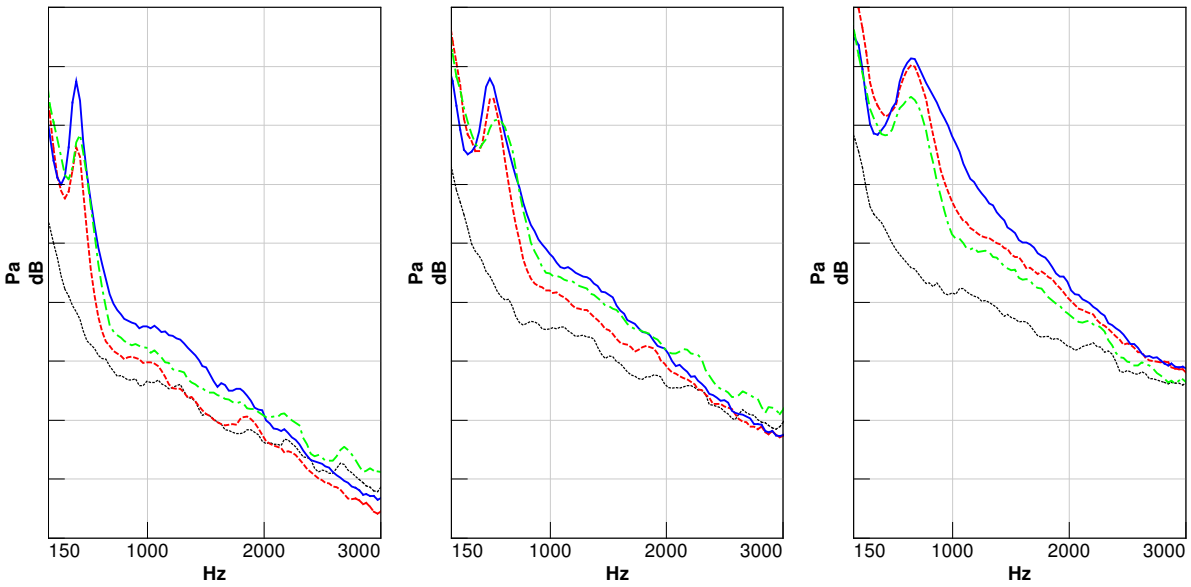

Figure 4.17: 2D Outwards leading edge BLT.
Exterior SPL [Grid = 5 dB], Frequency range: 0.15 – 3kHz.
Wind speeds: 80km/h (*left*), 100km/h (*center*), 120km/h (*right*).
— No tripping, —· Lower LE, --- Upper LE, ··· No bar.

4.1.5 Two-Dimensional Inwards BLT applied on an Elliptical Cylinder

A triangle-shape step intruding into the profile surface (also known as groove) was tested in two different positions relative to the center of the profile (before and after the center). Those positions were tested at both the upper and lower sides of the profile and in combination of both (Figures 4.18 and 4.19). The depth of the intrusion is the same of the outwards tripping of the section 4.1.4, i.e. 1.5mm ($0.075h$ and $0.02c$). No reference of the noise effects of surface grooves was found on the literature.

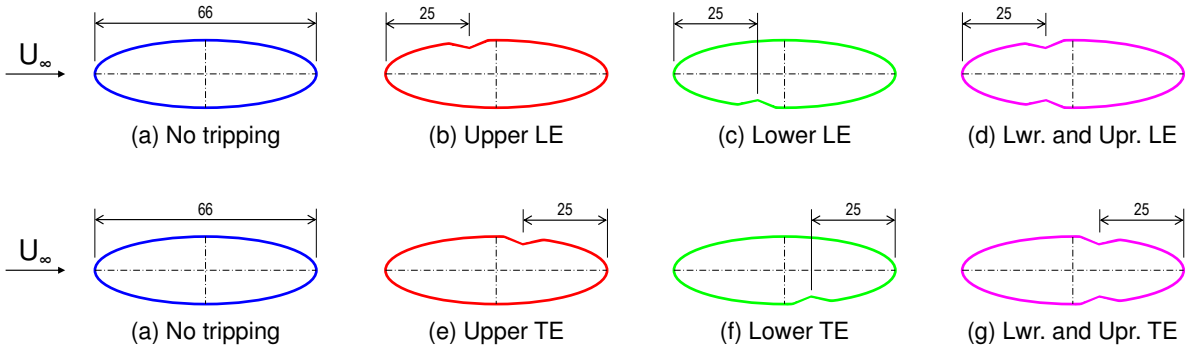

Figure 4.18: 2D Inwards Boundary Layer Tripping profiles [mm].

(a) No tripping (clay fill). (b) Upper LE. (c) Upper TE.

Figure 4.19: 2D Inwards Boundary Layer Tripping (upper side).

Figure 4.20 reveals the narrow and broadband noise effects of 2D Inwards Boundary Layer Tripping on the elliptical cylinder crossbar. Several observations can be withdrawn from the spectral plots. Similar to 2D Outwards BLT, the grooves do not eliminate the tonal noise formation but reduce its intensity and bandwidth at varying levels. By comparing tripping at the upper and the lower sides, at an specific location and wind speed, one can see a slight benefit of the lower side tripping on the tonal noise suppression. It is clear, however, that tripping at both upper and lower sides is reasonably more effective than a single side trip, except with tripping at the trailing edge in higher speeds. Due to that consideration, and added to the qualitative effects observed in the other locations and wind speeds, tripping at both upper and lower leading edge is the most effective feature in both narrow and broadband noise suppression.

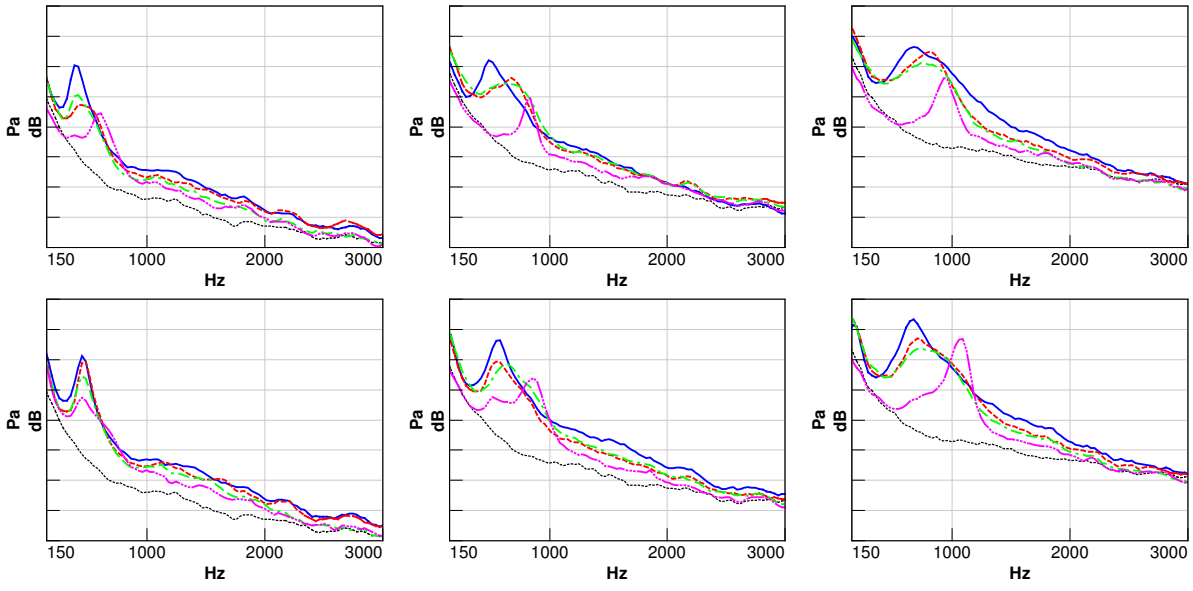

Figure 4.20: 2D Inwards Boundary Layer Tripping.
Exterior SPL [Grid = 5 dB], Frequency range: 0.15 – 3kHz.
Wind speeds: 80km/h (*left*), 100km/h (*center*), 120km/h (*right*).
Trip location: Leading edge (*top*), Trailing edge (*bottom*).
— No tripping, --- Upper side, —· Lower side, —·· Upper and Lower sides, ··· No bar.

4.1.6 Turbulence Mesh BLT applied on an Elliptical Cylinder

Most of the work in roughness-related research has been aimed to understand the aerodynamics effects of ice accretion on unsteady flows over an airfoil (Santhanakrishnan and Jacob (2005)). It is known that small surface roughness primarily causes premature boundary layer transition and affects the surrounding flow field. Most of the existing data focuses on the empirical relationships of the roughness size and location with the degradation in aerodynamic performance (Kerho and Bragg (1997)).

The majority of the available literature has been performed for roughness heights smaller than the boundary layer thickness. In the present study, the precise boundary layer thickness is unknown, and a relatively high roughness height is chosen ($h = 1.5mm$, same as 2D Outwards and Inwards BLT). The chord-wise extent of the roughness strip is also the same as in 2D Outwards BLT ($l = 12mm$) and is expected to be enough to trigger a complete boundary layer transition to the fully turbulent state (Figure 4.21). The roughness strip was installed at the same positions of the 2D Outwards BLT (Figures 4.22 and 4.23) and its effect on the aeroacoustics of the elliptical cylinder was assessed.

In the upper surface of the ellipse, all strip configurations increased the amplitude of the primary tone and reduced its bandwidth (Figure 4.24). The strip is either too tall or too long that is causing a drastic perturbation of the airflow path instead of an earlier transition of the boundary layer state to turbulent. Consequently, the tripped elliptical cylinder assumed the behavior of a blunter body presenting a well defined vortex structure with a primary acoustic tone at lower frequencies. With the strips located at the lower center of the ellipse, similar effect was observed with the strip at the upper center of the profile. The strips placed at the lower leading and trailing edges were capable to reduce the tonal noise amplitude as well as its bandwidth in higher speeds. Tripping at the lower leading edge was more efficient than at the lower trailing edge .

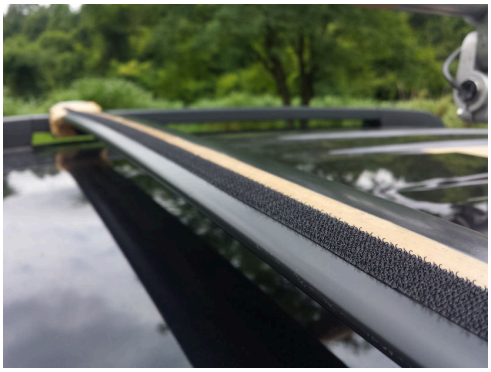

Figure 4.21: Turbulence Mesh Boundary Layer Tripping detail.

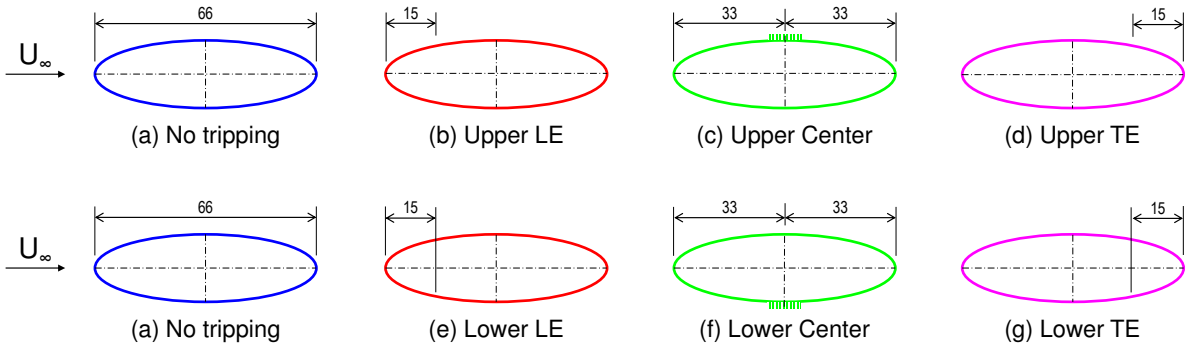

Figure 4.22: Trubulence Mesh Boundary Layer Tripping locations [mm].

(a) Upper LE. (b) Upper Center. (c) Upper TE.

Figure 4.23: Turbulence Mesh Boundary Layer Tripping (upper side).

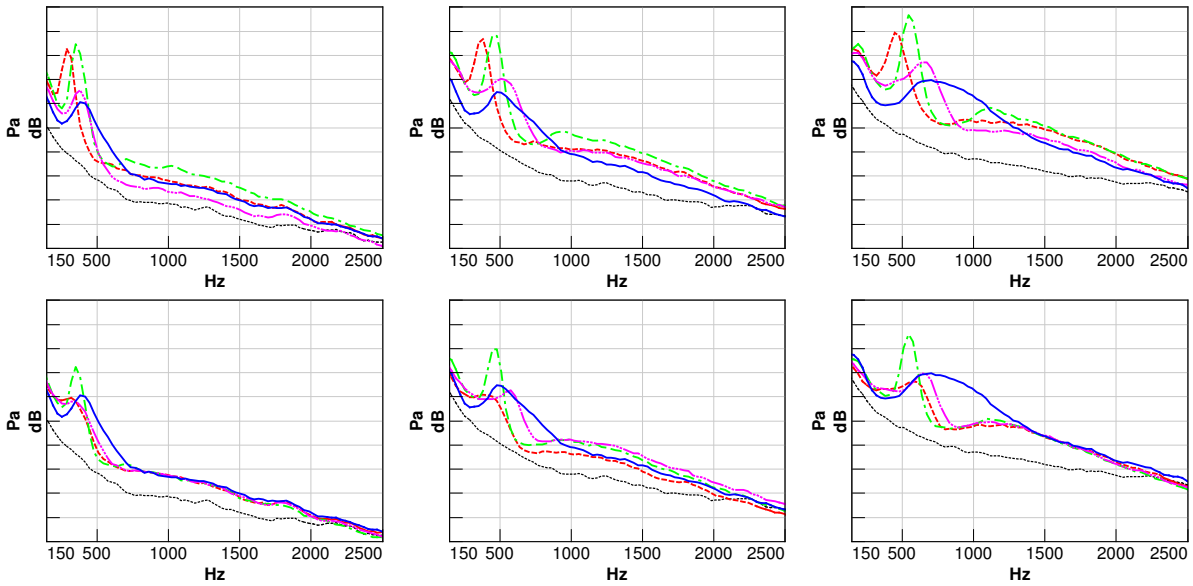

Figure 4.24: Turbulence Mesh Boundary Layer Tripping.
Exterior SPL [Grid = 5 dB], Frequency range: 0.15 – 2.5kHz.
Wind speeds: 80km/h (*left*), 100km/h (*center*), 120km/h (*right*).
Trip location: Upper side (*top*), Lower side (*bottom*).
— No tripping, --- Leading edge, —· Center, —··· Trailing edge, ··· No bar.

4.1.7 Three-Dimensional BLT applied on an Elliptical Cylinder

Lyon *et. al* (1997) have tested the aerodynamic effects of 3D Boundary Layer Tripping on three different airfoils at the Reynolds range of interest ($100,000 < Rey_c < 190,000$), and compared the results to single and multiple 2D tripping. The authors also studied different tripping locations and heights, and indicate little advantage in using 3D tripping over single or multiple 2D tripping for aerodynamic drag reduction.

Winkler *et. al* (2009) have studied the aerodynamic properties and the trailing edge noise of a NACA 6512-63 airfoil at zero Angle of Attack and $Rey_c = 190,000$, in clean and tripped conditions (single stair-step and serration tripping types at the leading edge). The authors have used incompressible Large Eddy Simulation (LES) coupled with different CAA methods (Amiet's and Ffowcs Williams & Hall's Trailing-Edge noise theories and Curle's compact dipole solution) to compute tonal and broadband noise and compare to experimental measurements taken at an aeroacoustic wind tunnel. The primary objective of the study is to assess different modeling methods of Boundary Layer Tripping. Results demonstrate single 2D stair-steps may be too thin to disturb the boundary layer and promote efficient transition, therefore requiring trip height optimization, whereas the 3D serrations are more efficient and lead to direct transition. Figures 4.25 and 4.26 show the instantaneous contours of wall-shear stress and flow-field visualization of the airfoil in clean, with 2D tripping and 3D serrations, obtained by LES. One can see the 3D serration was more effective in transitioning the boundary layer at the pressure (lower) side of the airfoil. In the suction (upper) side, transition point is fairly the same for the three cases (2D and 3D tripping slightly delayed separation), with differences in the vorticity scales developed after transition.

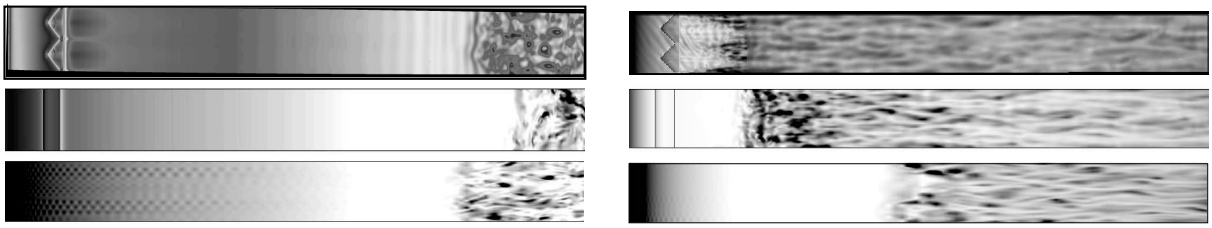

Figure 4.25: Instantaneous contours of wall-shear stress on the airfoil suction side (left) and pressure side (right), for the 3D serration trip, 2D step trip and clean airfoil LES (from top to bottom). Adapted from Winkler *et. al* (2009).

The effectiveness of the 3D tripping on the elliptical cylinder profile was assessed (Figure 4.27). The trip was installed on the upper side of the profile. At all wind speeds, the trip was capable of completely eliminating the broad tonal from the clean ellipse (Figure 4.28), revealing the change in airflow direction disturbs the main vortex shedding

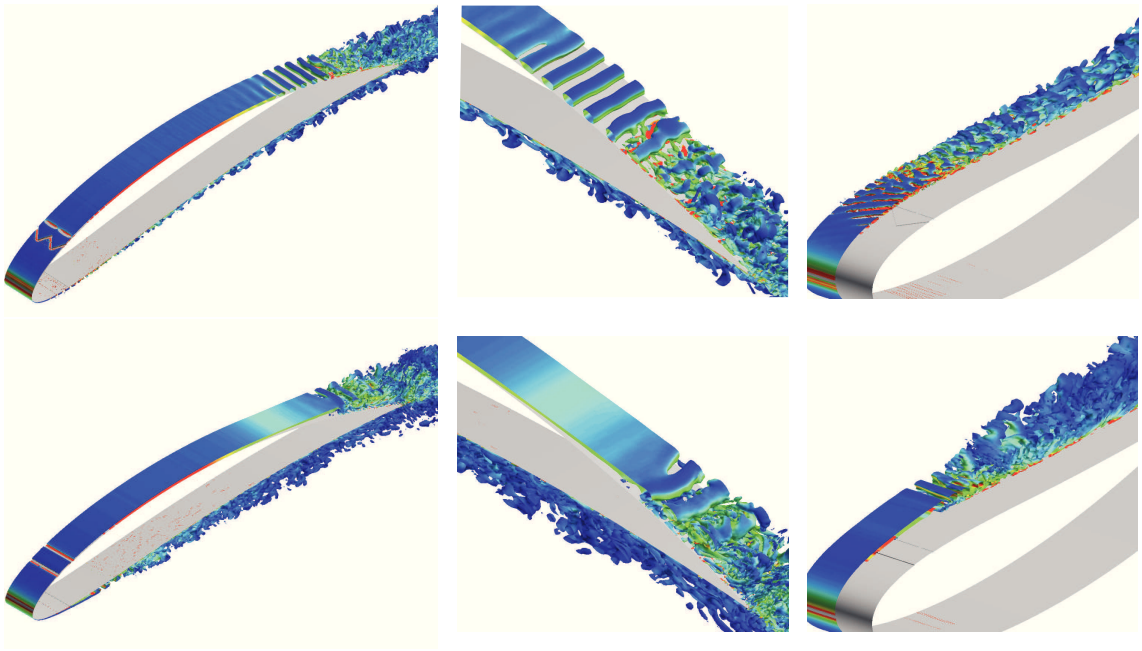

Figure 4.26: Flow-field visualization of the airfoil suction side (left), its trailing edge region (middle) and the pressure side (right) of the flow-field by isosurfaces for the serration trip LES (top) and the step trip LES (bottom). Adapted from Winkler *et. al* (2009).

periodicity, and consequently the formation of a dipole source. On the other hand, it increases the wake and the intensity of the quadrupole sources in lower speeds (transition occurs earlier than in clean configuration), causing an increase in the broadband noise. In higher speeds, the broadband noise is similar to that of the clean ellipse (same or approximate transition point).

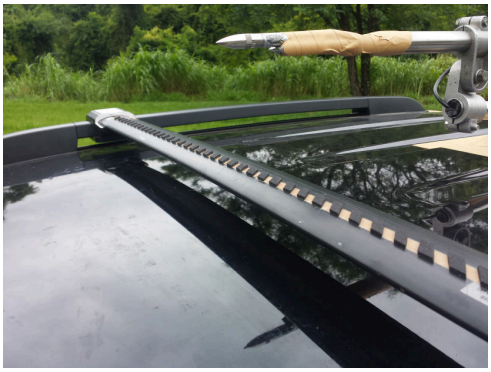

Figure 4.27: 3D Boundary Layer Tripping on Elliptical cylinder.

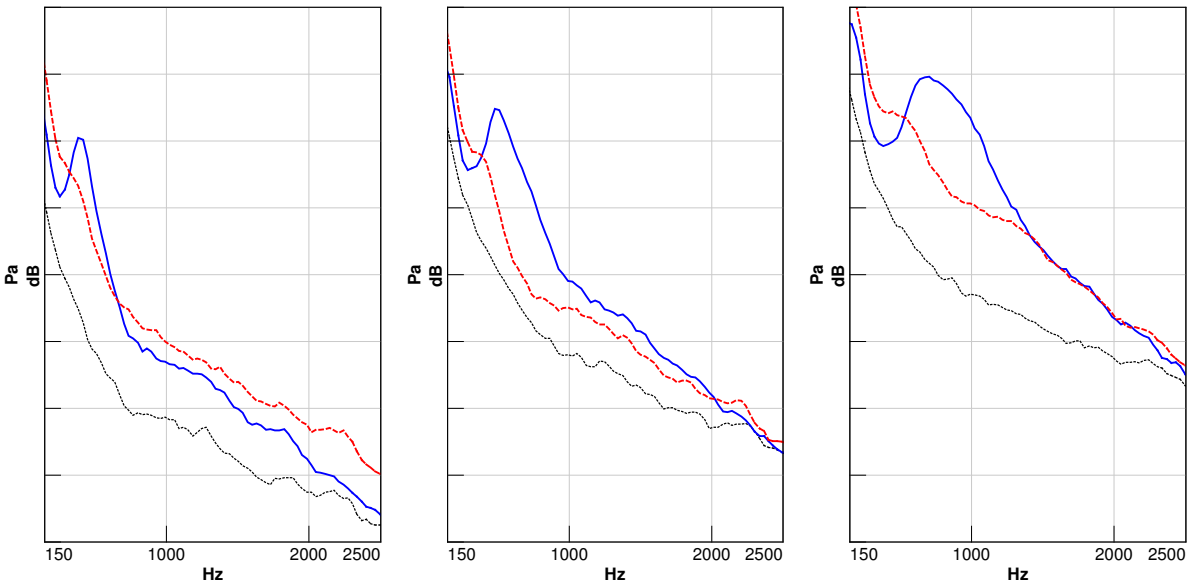

Figure 4.28: 3D BL Tripping on Elliptical cylinder.
Exterior SPL [Grid = 5 dB], Frequency range: 0.15 – 2.5kHz.
Wind speeds: 80km/h (*left*), 100km/h (*center*), 120km/h (*right*).
— No tripping, --- Upper 3D tripping, ··· No bar.

4.1.8 Overall Boundary Layer Tripping Analysis

The objective of the present section is to compare the effectiveness of each of the Boundary Layer Tripping methods assessed separately. Such analysis cannot be done in a single spectral plot once each type of tripping data was acquired in a different test shift, so the shift-to-shift variation (5 dB at 80km/h and 3 dB at 120km/h) would represent a significant noise factor. Therefore, the overall analysis was done by assessing the effect of each tripping type qualitative and quantitatively in separate spectra, considering the reference conditions (no bar and untripped bar) measured in its test shift. The three first rows of Figure 4.29 bring the data for the 2D tripping and roughness installed at the lower leading edge of the profile (optimum position for all types of tripping). The 2D and roughness strips have the same height and chord-wise length. The bottom row of Figure 4.29 shows data of the 3D tripping at the upper side of the profile. The center frequency of the broad tonals was marked with vertical lines and the Sound Pressure Level of each spectrum at that center frequency is showed in the cursor legend at the upper right of each window. The center frequency value of the clean elliptical profile is colored in blue, and for the tripped condition in red.

At 80 and 100km/h, the behavior of the 2D outwards and inwards tripping is similar qualitative and quantitatively. Both tripping methods reduced the main tone amplitude by 5 dB at 80km/h and 3 dB at 100km/h (Figure 4.29). At 120km/h, 2D Outwards tripping performed slightly better in reducing the tonal noise amplitude than the 2D

inwards tripping. The broadband noise behavior of both 2D tripping methods is similar at all wind speeds (Figure 4.30). Roughness at the lower leading edge caused a switch of the center frequency to a lower value in all wind speeds with a reduction in amplitude of approximately 2 dB. No reduction in broadband noise was observed when comparing to the clean ellipse noise. 3D tripping eliminated the tone and kept the same broadband noise levels as the clean ellipse profile, except at 80km/h where it slightly increased the broadband noise.

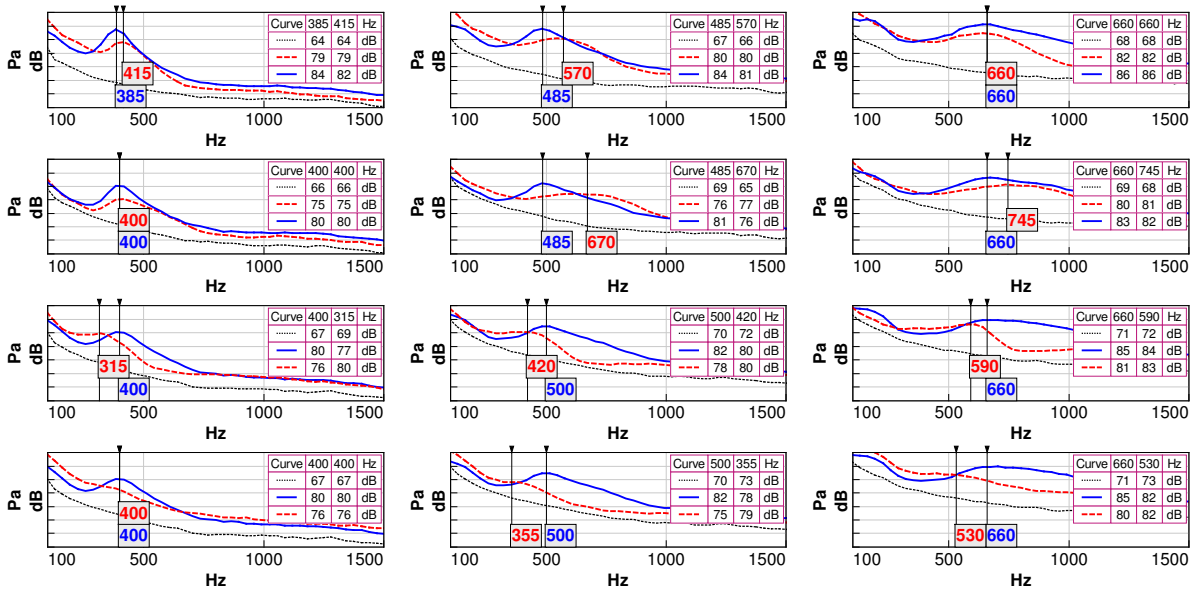

Figure 4.29: Overall Boundary Layer Tripping Analysis.
Exterior SPL [Grid = 5 dB], Frequency range: 0.1 – 1.5kHz.
Wind speeds: 80km/h (*left*), 100km/h (*center*), 120km/h (*right*).
Tripping types: 2D Out. (1^{st} *line*), 2D In. (2^{nd} *line*), Roughness (3^{rd} *line*), 3D (4^{th} *line*).
— No tripping, --- Tripped, ··· No bar.

The effectiveness of the Boundary Layer Tripping types was assessed from the receiver perspective (vehicle occupants) with the interior microphone (Figure 4.31). As it is observed in Figure 4.29, 2D Outwards and Inwards tripping switched the broad tonal center frequency to higher values at 100 and 120km/h. In the opposite, Roughness and 3D tripping switched the center frequency to lower values. For this specific vehicle and the characteristics of its transmission path, Roughness and 3D tripping were more effective in suppressing the incremental noise from the elliptical crossbar. Roughness tripping effect was superior to 2D tripping in despite of presenting lower acoustic pressure suppression at the source. The three-dimensional effect associated to roughness and tipped vanes plays an important role in suppressing the tonal noise from the crossbar. From the manufacturing standpoint, however, 3D tripping is more complex to implement once it requires additional components, while 2D tripping can be implemented on the crossbar extrusion tooling.

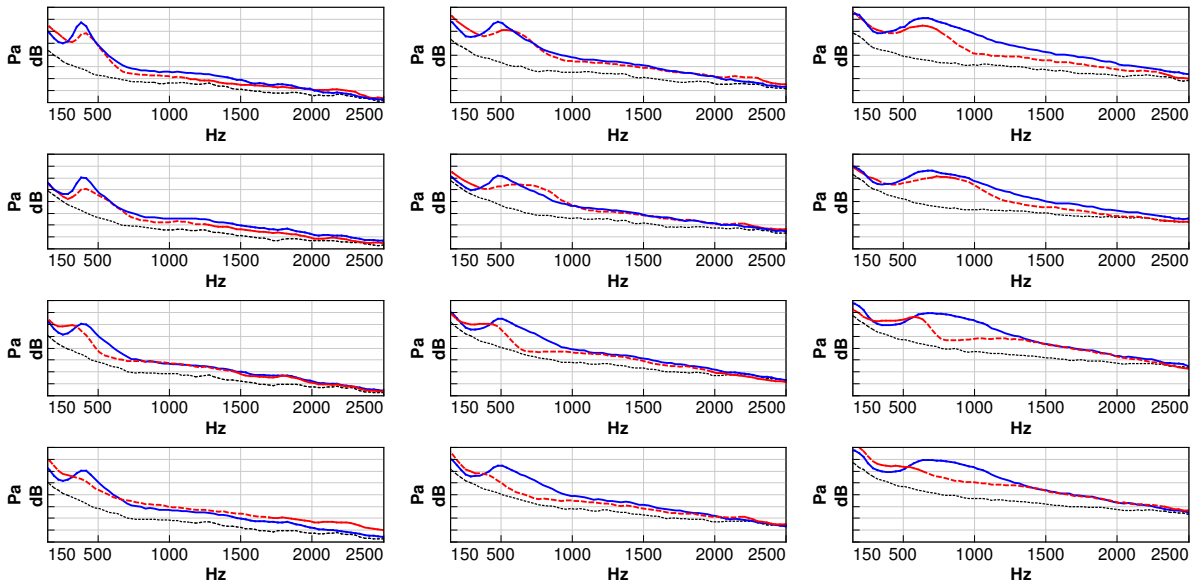

Figure 4.30: Overall Boundary Layer Tripping Analysis.
Exterior SPL [Grid = 5 dB], Frequency range: 0.1 – 2.5kHz.
Wind speeds: 80km/h (*left*), 100km/h (*center*), 120km/h (*right*).
Tripping types: 2D Out. (1^{st} *line*), 2D In. (2^{nd} *line*), Roughness (3^{rd} *line*), 3D (4^{th} *line*).
— No tripping, --- Tripped, ··· No bar.

When analyzing the effectiveness of different solutions to the aeroacoustic problem in automotive crossbars, the transmission path must be taken into consideration. An analysis based uniquely on exterior data at the source region may lead to incorrect or non-optimized solutions.

4.2 Perforation

All the aeroacoustic noise mitigation techniques explored in the previous sections refer to existing solutions in the field. The objective so far was to analyze common practices, identify the strengths and weakness of each and determine which ones present the optimum benefit towards noise reduction. The present and following sections have the objective of analyzing innovative solutions known from the literature and other fields of application such as turbomachinery and aeronautics, those which were never applied in automotive aeroacoustics.

The present section brings the application of a porous media on the upper and lower sides of the trailing edge of an elliptical cylinder as a potential tonal and broadband noise attenuation strategy. The perforation effect on the aeroacoustics of flat plates and wing sections has been studied since trailing edge porosity was found as one of the rationale behind the silent flight of owls (Jaworski and Peake (2013)). Trailing edge noise can be

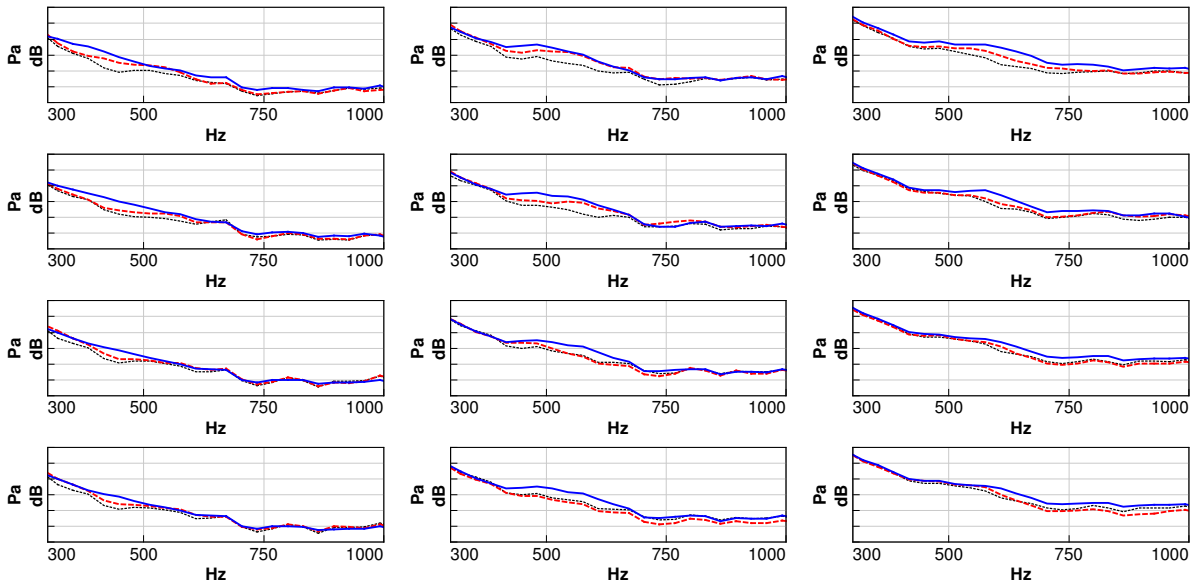

Figure 4.31: Overall Boundary Layer Tripping Analysis.
Interior SPL [Grid = 5 dB], Frequency range: 0.3 – 1kHz.
Wind speeds: 80km/h (*left*), 100km/h (*center*), 120km/h (*right*).
Tripping types: 2D Out. (1^{st} *line*), 2D In. (2^{nd} *line*), Roughness (3^{rd} *line*), 3D (4^{th} *line*).
— No tripping, --- Tripped, ··· No bar.

effectively eliminated by perforated surfaces once they affect the phase of the sound waves and reduce the scattered sound levels (Cavalieri *et. al* (2016)). Other strategies to reduce trailing edge noise similar to porosity are based on the modification of the trailing edge geometry in the form of sawtooth serrations or stiff brush inserts. Therefore, perforation is a promising solution to mitigate trailing edge noise in relatively blunt profiles in low Mach flows, such as in automotive roof rack applications.

Figure 4.32 shows the two rows of perforations drilled both on the upper and lower trailing edge surfaces of the elliptical crossbar. The perforations have 3mm of diameter and are spaced 20mm span-wise and 10mm chord-wise. The distance from the rearmost row to the trailing edge is 10mm. Figure 4.33 reveals the noise spectra measured with the upper perforations taped (lower perforations open only) and with the upper and lower perforations open. With the lower perforations open only, a pressure amplitude reduction is observed only at 80km/h. The broadband noise effect is negligible except at 80km/h where pure high frequency tones start to appear at the 3kHz region. With both upper and lower perforations open, the tonal noise pressure level reduces approximately 5 dB in higher speeds, demonstrating the noise reduction mechanism is related to the sound scattering on both surfaces of the profile. Interestingly, the residual tone is actually split in two separate tones with lower amplitude and narrower bandwidths (within the original clean profile tonal frequency bandwidth). As a counter effect, however, with both side perforations open, whistling occurs at all speeds (stronger in lower speeds). The high

frequency tones completely degrade the sound signature inside the vehicle cabin. The effectiveness of perforation is confirmed, but with rise to the counter effect that circular surface perforations parallel to the airflow direction originate high frequency whistling which needs to be addressed by geometric optimization, such as orifice diameter and shape tuning.

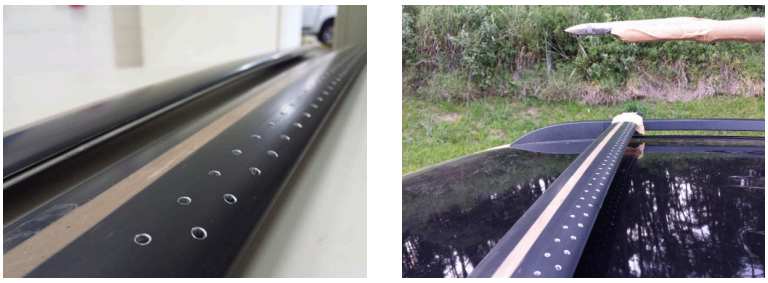

(a) Trailing edge perforations. (b) Measurement.

Figure 4.32: Perforation applied on the trailing edge of the elliptical crossbar.

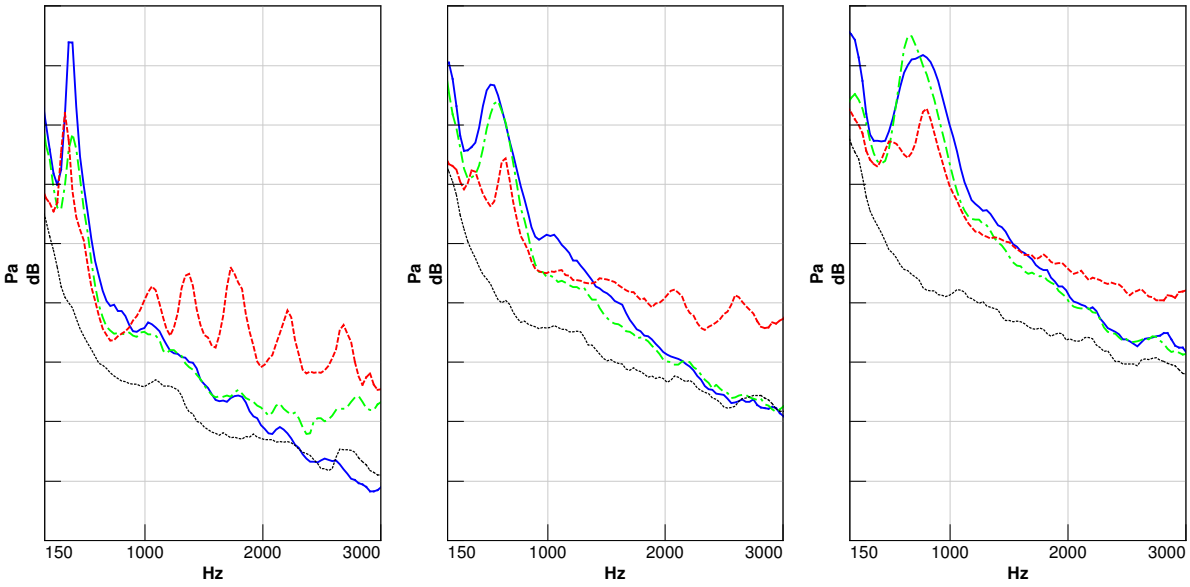

Figure 4.33: Perforation effect.
Exterior SPL [Grid = 5 dB], Frequency range: 0.15 – 3kHz.
Wind speeds: 80km/h (*left*), 100km/h (*center*), 120km/h (*right*).
— No perforations, —· Lower perforations, --- Upper & Lower perforations, ··· No bar.

4.3 Active Trailing Edge Blowing (TEB)

Active Trailing Edge Blowing (TEB), also known as the Wake-filling Concept (Winkler *et. al* (2010)), has been studied for decades with the major objective of improving the aerodynamic performance of blunt profiles and wing sections. Recently, with the advances

in aircraft noise regulations and the consequent necessity of reducing airframe noise during take-off and landing, active blowing has been considered as an alternative to reduce noise from high-lift devices (Pollenske and Pfingsten (2010)), airfoils (Gerhard *et. al* (2014), Ramirez and Wolf (2015)), high-speed fan rotors and tandem airfoils (Brookfield and Waitz (2000), Winkler *et. al* (2010), Enghardt *et. al* (2015)). Figure 4.34 illustrates the application of TEB on airfoils and fan rotors. Both concepts adopt internal passages within the airfoil and blades for injection of fluid into the wake through blowing slots located in the trailing edge or surfaces near.

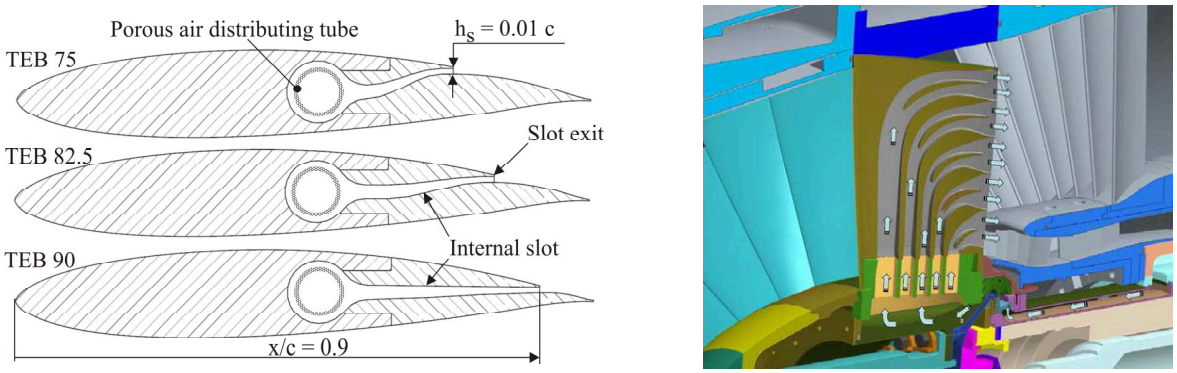

(a) TEB airfoil sections.

(b) TEB fan rig.

Figure 4.34: TEB application on airfoils and fan rotors, adapted from Gerhard *et. al* (2014) (a) and Enghardt *et. al* (2015) (b).

Trailing Edge Blowing has the potential of reducing both tonal and broadband noise emitted by wing sections in low Mach and Reynolds flow regime. One of the theories is that by filling in the wake with flow mass and momentum, the mean velocity profile changes and the wake deficit reduces, and consequently the amplitude of the periodic pressure fluctuations and of the tonal noise can be significantly reduced (Brookfield and Waitz (2000), Winkler *et. al* (2010)). A second explanation is that blowing reduces trailing edge tonal noise generation by moving the quadrupole incident field away from the airfoil surface hence reducing the scattered field, as demonstrated by Ramirez and Wolf (2015) for a NACA 0012 with thickened trailing edge at positive Angle of Attack, in $M_\infty = 0.1$ and $Re_c = 100,000$ flow (Figure 4.35). Depending on the location and geometry of the blowing slots, the main shear layers are modified and can reduce the broadband noise as well, however, they can also generate undesired pure tones (whistling) or transmit noise from the airflow blowing system to the receiver. Therefore, the design of the blowing system, either supplied by piping or by internal air compressors, must account for those counter effects to be efficient.

In this project, three different blowing slot strategies were assessed. The first one is the application of a spanwise opening at the trailing edge across the entire crossbar (Figure 4.36a). The gap was tested in two different heights ($h = 1.5mm$ and $3mm$). The second

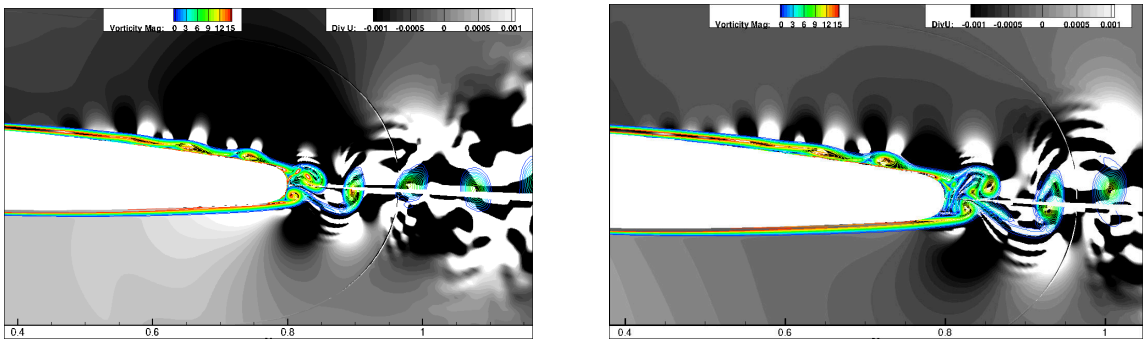

(a) No blowing. (b) With blowing ($U_b = 10\%U_\infty$).

Figure 4.35: Contours of vorticity magnitude in color and contours of dilatation in grayscale for $M_\infty = 0.1$ for a NACA 0012 with thickened trailing edge at positive Angle of Attack, adapted from Ramirez and Wolf (2015).

concept is similar to the one used by Enghardt *et. al* (2015), which is the application of an array of orifices at the trailing edge (Figure 4.36b). The orifices have a diameter of $2mm$ and are spaced by $20mm$. The third concept uses the perforations studied in section 4.2 as blowing outlets on the upper and lower surfaces of the trailing edge (Figure 4.36c). The perforations have 3mm of diameter and are spaced 20mm span-wise and 10mm chord-wise. The distance from the rearmost row to the trailing edge is 10mm.

(a) TE gap ($h = 1.5mm$, $3mm$). (b) TE orifices. (c) Upper & Lower perforations.

Figure 4.36: Trailing Edge Blowing slot types.

Different blowing mass flow rates were assessed. The target is to achieve different blowing speeds (U_b) up to 30% of U_∞. The active air blowing system is similar to the one used by Pollenske and Pfingsten (2010), which has used a small fraction of the cold engine flow to generate the blowing jet flow. In this case, a fraction of the HVAC (Heating, Ventilation and Air Conditioning) air system was collected and piped into the crossbar by an external duct (Figure 4.37). The key advantage of using the HVAC system air is that various blowing jet speeds can be obtained by adjusting the Air Conditioning operating mode, which includes the variation of the CRFM speed (Condenser, Radiator and Fan Module) from V1 to V5 adjustable at the Instrument Panel knob, the circulation mode, i.e. outside air or recirculation mode, and the number of open Air Conditioning vents.

The vehicle tested has four Air Conditioning vents (one at each corner of the Instrument Panel and two at the center). A second advantage of using HVAC air is the control of the airflow temperature. In this study, the conditioned air temperature was fixed at 20°C, but in further studies the temperature could be assessed as well. The air was collected uniquely at the left corner vent, but the condition of the remaining three vents directly influences the mass rate at the piped vent. In order to estimate the resulting blowing jet flow rate and speed (U_b), for each type of blowing slot, all available Air Conditioning volumetric flow rates ($\dot{V}$) were measured at the test bench shown in Figure 4.38 and the results are listed in Table 4.1. in total, 40 different airflow rates were available.

(a) Airflow piping system. (b) HVAC system air intake.

Figure 4.37: HVAC air piping system.

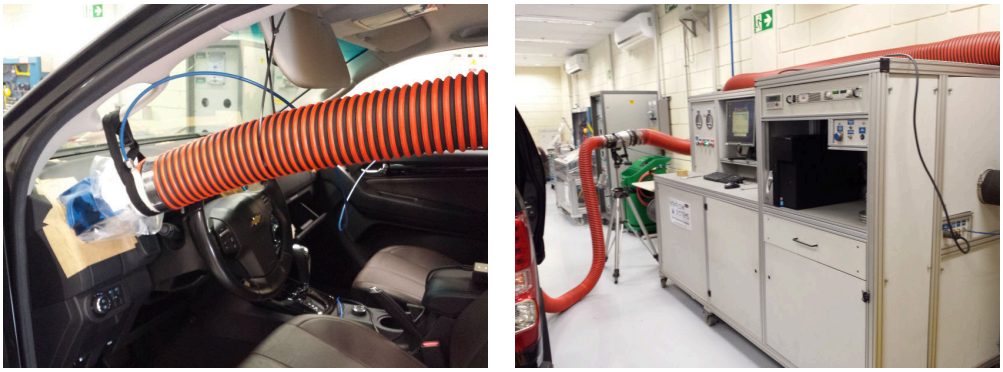

(a) HVAC system air intake. (b) Airflow test bench.

Figure 4.38: HVAC system airflow measurement.

The total crossbar trailing edge blowing area (A_b) was calculated for each type of blowing slot. The trailing edge gaps with $h = 1.5mm$ and $3mm$ present a total open area of 1.35 $10^{-3}m^2$ and 2.7 $10^{-3}m^2$ respectively. The trailing edge orifices provide an area of 0.14 $10^{-3}m^2$ and the trailing edge perforations 1.27 $10^{-3}m^2$. With the total volumetric flow rate and the blowing slot areas, the blowing speeds were estimated ($U_b = \frac{\dot{V}}{A_b}$). For the trailing edge gaps with $h = 1.5mm$ and $3mm$, blowing speeds from 4% to 51% of U_∞ and from 2% to 26% of U_∞ were available, respectively. For the perforations,

Volumetric airflow rate ($\dot{V}$), m^3/s			
Open AC Vents	CRFM Speed	Recirculation Mode	Outside Air
L	V1	0.0152	0.0128
	V2	0.0294	0.0246
	V3	0.0380	0.0324
	V4	0.0464	0.0403
	V5	0.0555	0.0489
L+R	V1	0.0108	0.0097
	V2	0.0214	0.0178
	V3	0.0275	0.0234
	V4	0.0343	0.0292
	V5	0.0416	0.0353
L+R+CL	V1	0.0091	0.0072
	V2	0.0173	0.0142
	V3	0.0227	0.0187
	V4	0.0278	0.0232
	V5	0.0335	0.0285
L+R+CL+CR	V1	0.0073	0.0059
	V2	0.0149	0.0121
	V3	0.0196	0.0160
	V4	0.0241	0.0201
	V5	0.0297	0.0248

Table 4.1: Total Volumetric airflow rate provided by the HVAC system. L=Left, R=Right, CL=Center Left, CR=Center Right.

blowing speeds of 4% to 55% of U_∞ were obtained, and for the trailing edge orifices, the minimum blowing speed obtained was 35%, while the maximum values were even higher than U_∞. Once head losses and back pressure were not considered in the calculations, the actual airflow exiting the outlets and consequently the blowing speed are lower than the estimated values. Instead of testing the different concepts of trailing edge blowing uniquely at the target blowing speeds ($U_b \leq 30\% U_\infty$), each blowing outlet type was tested under all AC operational conditions, i.e. with all available blowing jet speeds, and just the best results in terms of noise suppression were plotted in Figure 4.40. The optimum blowing speeds relative to the free stream flow speed is shown in Table 4.2. The blowing conditions presented on Figure 4.40 refer to Table 4.2.

Prior to assessing the blowing effect, the presence of trailing edge gap without blowing was verified. The noise spectra for the $h = 3mm$ gap (Figure 4.36a) without blowing

Optimum estimated blowing speeds (U_b), $\%U_\infty$			
Blowing type	%80km/h	%100km/h	%120km/h
TE Gap, $h = 1.5mm$	51%	41%	34%
TE Gap, $h = 3mm$	16%	21%	17%
TE Orifices	NA*	NA*	64%
Perforations	55%	30%	10%

Table 4.2: Estimated airflow speed at the blowing outlets.
***Estimated value inconsistent without consideration of back pressure.**

is shown in Figure 4.39. Traces of tonal noise suppression are observed in all speeds. The reduction in amplitude is higher than the test run variation discussed in Section 2.6 (Figure 2.11), indicating the absence of a center strip of the rigid trailing edge wall affects the scattering of the main vortex dipole source of sound. A secondary effect of the trailing edge gap is the occurrence of secondary narrowband tones above 1kHz (whistling) similar to the the perforation effect (Figure 4.33). The physical mechanism behind the generation of those tones is unclear at the present moment. The same effect was observed with the $h = 1.5mm$ trailing edge gap, and in much lower severity, the trailing edge orifices (Figure 4.40).

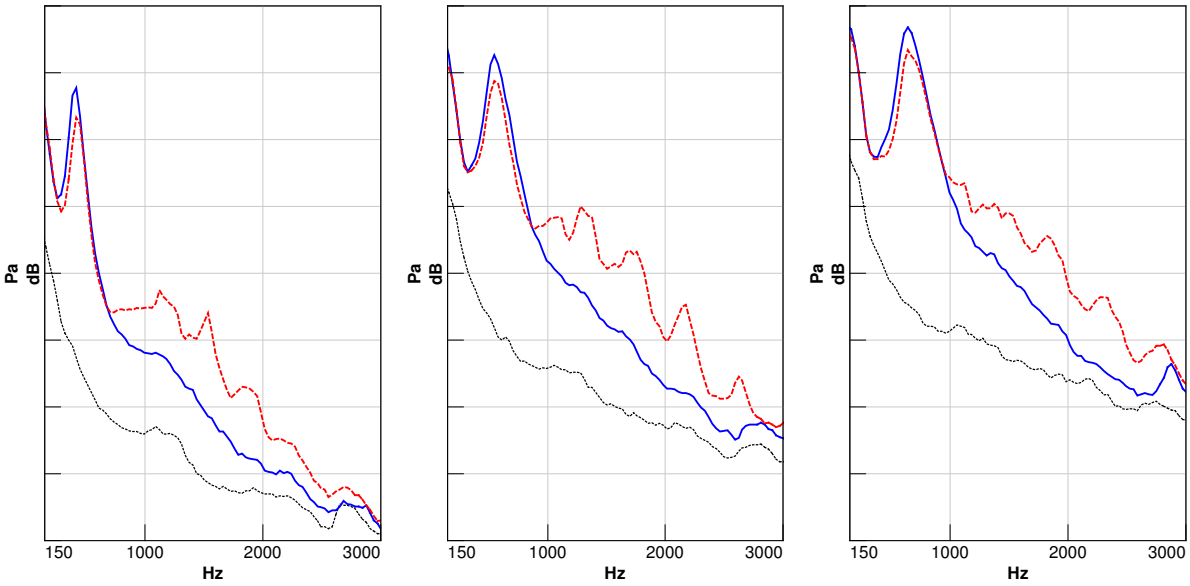

Figure 4.39: Trailing edge gap effect.
Exterior SPL [Grid = 5 dB], Frequency range: 0.15 – 3kHz.
Wind speeds: 80km/h (*left*), 100km/h (*center*), 120km/h (*right*).
— TE gap closed (no blowing), --- TE gap open (no blowing), ··· No bar.

The blowing effect for the three different blowing slot concepts, and blowing speeds described in Table 4.2, is shown in Figure 4.40. A clear reduction in the tonal noise amplitude is observed in lower speeds, for all types of blowing outlets. Active blowing

through trailing edge orifices is definitely capable of completely eliminating the primary tone of the crossbar at 80km/h and reducing its intensity at 100km/h. The trailing edge gaps of $h = 1.5mm$ and $3mm$ were less effective than the trailing edge orifices and present the counter effect of high frequency whistling. At 120km/h, the trailing edge orifices, at the present design conditions, were not capable of suppressing the primary tone significantly, but the results in lower speeds indicate that, with further optimization of the number and geometry of the orifices, blowing through trailing edge orifices is a promising solution.

Figure 4.41 shows the application of blowing through the perforations at the upper and lower surfaces of the crossbar trailing edge (Figure 4.36c). The high frequency tones are still present as in the no-blowing condition. The main tone, however, is significantly suppressed in higher speeds, further than with no blowing (perforation effect only). Once the spectral plots from Figures 4.40 and 4.41 cannot be directly compared once acquisitions were made in different test shifts, the effect of blowing applied through orifices on the trailing edge and perforations on the upper and lower surfaces of the trailing edge is compared in Figure 4.42. At all speeds, blowing through the upper and lower perforations were more effective in reducing the amplitude of the main tone, however those perforations presented more severe whistling in high frequency.

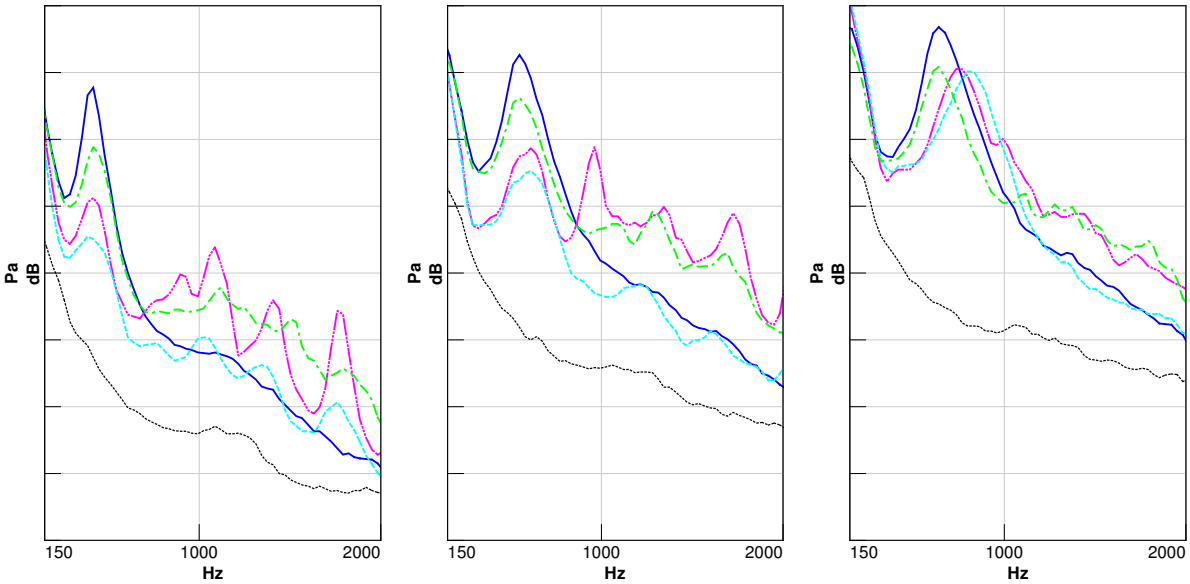

Figure 4.40: Trailing Edge Blowing effect.
Exterior SPL [Grid = 5 dB], Frequency range: 0.15 – 2kHz.
Wind speeds: 80km/h (*left*), 100km/h (*center*), 120km/h (*right*).
— TE gap closed (no blowing), ··· No bar,
—··· TE gap $h = 1.5mm$, —· TE gap $h = 3mm$, - - - TE orifices.

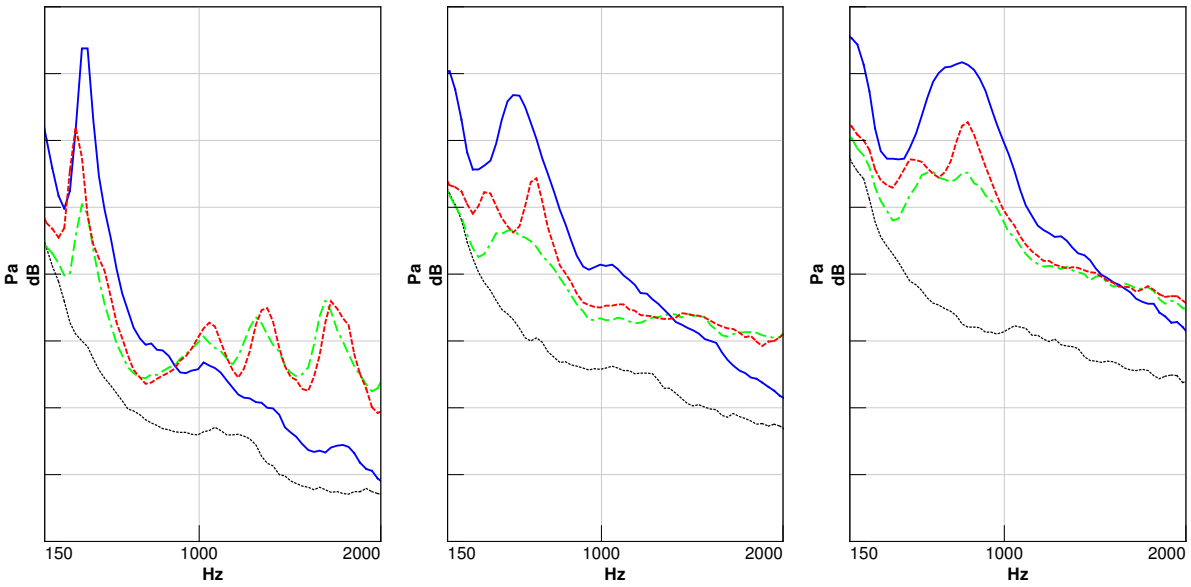

Figure 4.41: Perforation and Blowing effect.
Exterior SPL [Grid = 5 dB], Frequency range: 0.15 – 2kHz.
Wind speeds: 80km/h (*left*), 100km/h (*center*), 120km/h (*right*).
— No orifices, ··· No bar,
--- Upr. & Lwr. perforations (no blowing), —· Upr. & Lwr. perforations + blowing.

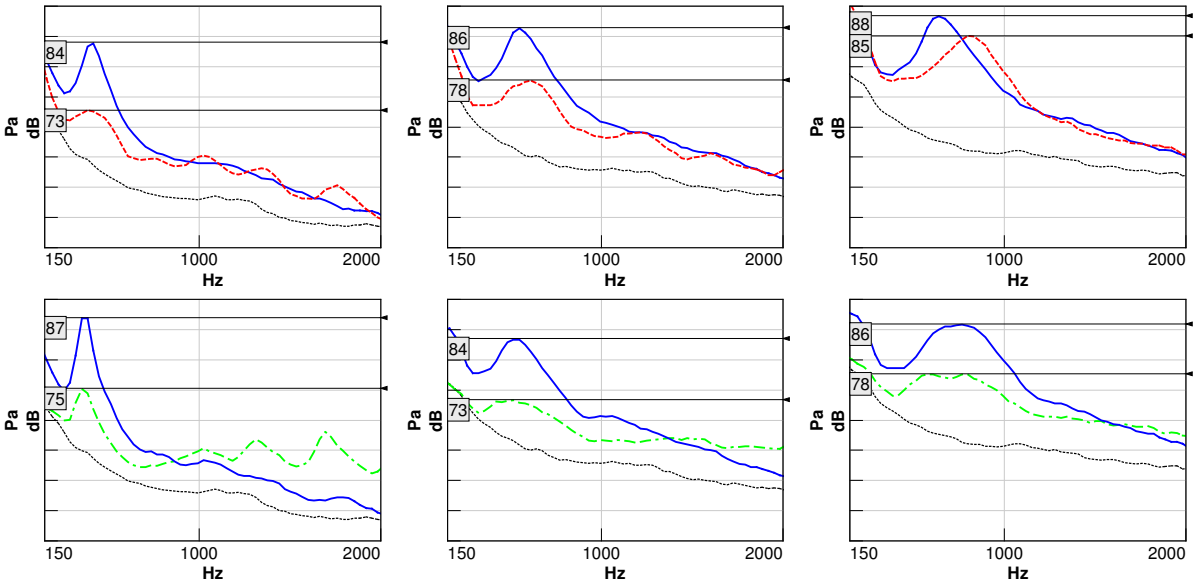

Figure 4.42: Comparison of blowing through TE orifices and perforations.
Exterior SPL [Grid = 5 dB], Frequency range: 0.15 – 2kHz.
Wind speeds: 80km/h (*left*), 100km/h (*center*), 120km/h (*right*).
— No orifices and blowing, ··· No bar,
--- TE orifices + blowing, —· Upr. & Lwr. perforations + blowing.

5 CONCLUSIONS

Motivated by the N&V challenges caused by vehicle electrification, the aeroacoustic phenomena associated to automotive roof crossbars were deeply studied in this project. A robust methodology to measure crossbar noise on track considering inherent variation and uncertainty was developed, enabling a clear understanding of the noise generation mechanisms associated to elliptical profile crossbars, which represent the basic shape used in automotive roof rack systems. Wake interaction and the key geometric contributors to the tonal and broadband noise originated by the crossbar were understood, and noise control techniques such as Angle of Attack and two and three-dimensional Boundary Layer Tripping (BLT) were deeply investigated. In addition, a new look to innovative noise solutions such as Perforation and Trailing Edge Blowing (TEB) was provided. Thin trailing edges were capable to completely eliminate the aeolian tone. Positive incidence angles were effective in suppressing the aeolian tone just in lower speeds. Three-dimensional BLT techniques have demonstrated an advantage over two-dimensional BLT methods. Both TEB and Perforation were effective in reducing the aeolian tone but presented counter effects such as high frequency whistling. Further learnings on each specific sub area of this work are summarized in the following item list.

Experimental method:

- Exterior sound pressure measurements taken on track have demonstrated good accuracy when compared to the same measurements taken in an aeroacoustic wind tunnel, as well as good repeatability with exterior noise factors controlled. Exterior sound intensity measurements on track are highly affected by low frequency phase mismatching, and interior sound pressure (receiver location) does not capture aeroacoustic effects in due resolution **(Sections 2.4 and 2.6)**.

Wake interaction:

- Flow visualization and reference aeroacoustic measurements have proven the roof effect does not change the flow dynamics and noise generation mechanisms associated to roof crossbars significantly. Flow restriction causes a small increase in the tonal noise frequency for gap ratios above critical when vortex suppression occurs **(Section 3.1)**. That implicates the generated crossbar noise has a small dependence on the vehicle characteristics for gap ratios above critical, allowing for the development of crossbar shapes in reduced scale aeroacoustic wind tunnels using

natural scale crossbars under this gap ratio condition. On the other hand, in-vehicle validation at the receiver location is still required to account for transmission path effects such as reflection and absorption.

Reference profiles:

- The characteristics of the tonal noise generated by elliptical shape crossbars (amplitude, center frequency and bandwidth) depend on the flow regime they are immersed. In lower Reynolds ($Re_c = 98,000$), elliptical cylinders behave similar to a blunt body (circular cylinder); in higher Reynolds ($Re_c = 147,000$), elliptical cylinders presents the characteristics of a laminar profile (NACA 0012) **(Section 3.2, Figure 3.12)**;
- The elliptical cylinder generates more broadband noise (up to 5kHz) than the NACA 0012 and less than the circular cylinder. Above 1kHz most of the broadband noise is reflected and attenuated in the path (for this particular vehicle) and the incremental noise is unnoticed inside the vehicle cabin **(Section 3.2, Figures 3.14 and 3.15)**.

Elliptical cylinder geometry:

- The tonal noise amplitude and frequency generated by elliptical cylinders is mostly influenced by the trailing edge bluntness. Tapering the trailing edge (symmetrically and asymmetrically) reduces tonal noise amplitude and increases its center frequency. Symmetric sharp edge trailing edges completely eliminate the aeolian tone. In contrast, the thinnest the trailing edge, the higher the generated broadband noise **(Sections 3.3.1 and 3.3.2)**;
- The leading edge shape affects predominately the broadband noise. Increasing leading edge bluntness reduces broadband noise. Tapering the leading edge increases broadband noise. Leading edge bluntness and asymmetry affected the tonal noise characteristics just in lower speeds ($R_c = 98,000$) **(Sections 3.3.3 and 3.3.4)**;
- Full asymmetry (leading and trailing edges) reduces tonal noise intensity. An asymmetry pattern that hastens the flow underneath the profile increases broadband noise. Profiles that accelerate the airflow on the top surface of the profile reduces wake thickness in reference to the roof and reduces broadband noise **(Section 3.3.5)**.

Angle of Attack:

- Negative Angles of Attack significantly increase tonal noise amplitude and bandwidth and reduce its center frequency. In contrast, positive Angles of Attack reduce tone amplitude and bandwidth and increase its center frequency. Those effects are demonstrated by local flow visualization in addition to acoustic data. This effect can be attributed to the split of the vertically symmetric vortices of the near-wake at AoA=0°, which causes the lower eddy to loose interaction with the trailing edge surface. An angle of +6° was capable to completely eliminate the tone at 80km/h, but it was not as effective in higher speeds **(Section 3.4 and Figures 3.34, 3.39 and 3.40)**;

- Negative Angles of Attack increase broadband noise while positive Angles of Attack reduce it, in comparison to AoA = 0. That effect is directly related to the height of the crossbar wake (also demonstrated with local flow visualization). **(Section 3.4 and Figures 3.37, 3.39 and 3.40)**.

Boundary Layer Tripping (BLT):

- 2D Outwards Boundary Layer Tripping does not eliminate the main tone but is capable to reduce its amplitude and bandwidth. Tripping at the upper and lower leading edges are the most beneficial locations to reduce the tonal and broadband noise amplitude, with tripping at the lower leading edge being more effective in reducing tonal noise, and tripping at the upper leading edge more effective for broadband noise suppression **(Figures 4.15, 4.16 and 4.17)**. A combination of both was not tested and is suggested for future work;

- 2D Inwards Boundary Layer Tripping (grooves) does not eliminate the tonal noise but is capable to reduce its intensity and bandwidth, similar to 2D Outwards BLT. Tripping at the leading edge at both upper and lower sides was the most effective solution for both broad and narrowband noise suppression **(Figure 4.20)**;

- Roughness Boundary Layer Tripping was evaluated using relatively large roughness height and length. In the upper side of the profile, the roughness strip caused drastic airflow perturbation and increased the tonal noise amplitude. In the lower surface, leading and trailing edge trip reduced tonal noise intensity and bandwidth, with tripping at the leading edge being more effective (similar to 2D Outwards and Inwards BLT) **(Figure 4.24)**;

- 3D Boundary Layer Tripping was assessed by installing tipped vanes on the upper center of the elliptical profile. The trip completely eliminated the broad tonal from the clean ellipse shape, but increased its broadband noise in lower speeds **(Figure 4.28)**;

- An overall Boundary Layer Tripping analysis was performed considering acoustic data acquired at the source (Exterior SPL) and receiver (Interior SPL) locations. 2D and Roughness tripping of the same height, length and location (lower leading edge) were assessed and compared to 3D tripping at the upper surface. Different from literature data focused purely on the aerodynamics properties of wing profiles, i.e. there is little advantage in utilizing 3D over 2D tripping, the three-dimensional effect associated to roughness and tipped vanes played an important role in suppressing the tonal noise from the crossbar. The analysis of Interior SPL demonstrated the importance of considering the transmission path characteristics in the development of solutions to the aeroacoustic problem of automotive roof crossbars.

Perforation:

- The effectiveness of a porous media applied on the upper and lower surfaces of the trailing edge of an elliptical cylinder was assessed. The tonal noise pressure amplitude was considerably reduced with the orifices on both upper and lower sides, demonstrating the noise reduction mechanism is related to the sound scattering on both (not only one) surfaces of the profile. The residual tone is actually split in two separate tones with lower amplitude and narrower bandwidths. The counter effect of porosity is the generation of pure high frequency tones (whistling), which requires further orifice geometric optimization (e.g. diameter and shape tuning) **(Section 4.2)**.

Trailing Edge Blowing:

- Active Trailing Edge Blowing was assessed by piping a fraction of the HVAC system airflow into the crossbar and blowing it out through different slot concepts. Optimum results were obtained with estimated blowing speeds from 10% to 55% of the freestream speed. No corrections to head loss and back pressure were applied. The first concept of blowing slot assessed is the application of a span-wise trailing edge cut with different heights. That strategy was capable to reduce the intensity of the main tone by changing the scattering of the dipole source of sound on the trailing edge surface, but presented the counter effect of high frequency whistling. The second blowing concept was the application of an array of orifices on the trailing

edge line. Those orifices were more effective in attenuating the amplitude of the main tone than the trailing edge cuts, and did not present secondary high frequency tones. The third and most effective concept of blowing was the application of orifices on the upper and lower walls of the trailing edge, which were capable of eliminating the narrowband tone in higher speeds, but presented whistling in lower speeds. None of the blowing slot concepts were tuned to avoid whistling and to obtain maximum noise suppression. Therefore, active blowing has demonstrated its potential in reducing the tonal noise but requires further geometric optimization to suppress the counter effects. The utilization of passive blowing methods rather than active is also preferred from an engineering feasibility standpoint **(Section 4.3)**.

6 FUTURE WORK

The author suggests the continuation of this project with the following topics:

- Extend the Reynolds range ($Re_c < 98,000$ and $Re_c > 147,000$) on the comparison of the elliptical cylinder noise to the circular cylinder and NACA 0012 profile, to explore the boundaries where the elliptical cylinder will present a coincident tone to the circular cylinder and the same broadband noise behavior of the NACA 0012. It would also be interesting to compare the elliptical cylinder noise to beveled trailing edge profiles' noise.
- Measure the noise from a symmetric profile (e.g. elliptical cylinder or NACA 0012) in positive and negative Angle of Attack, simultaneously at its pressure and suction sides and in free sound field domain, with the objective of understanding whether the observed opposite noise trends are related to the data acquisition side or to the presence of a ground in the acoustic field.
- Test 2D Outwards Boundary Layer Tripping combining upper and lower leading edge trips to verify whether its noise suppression effectiveness overcomes the lower leading edge single tripping configuration, as observed in 2D Inwards Boundary Layer Tripping. Also, further explore 2D Outwards Boundary Layer Tripping geometries, e.g. different tripping heights, lengths and the angle of its foreword-facing edge.
- Test 3D Boundary Layer Tripping at different locations such as the lower and upper leading and trailing edges, as well as the lower center. It would also be of great interest to understand the effect of different 3D geometries on noise suppression, e.g. variation of vanes angle and height.
- Perform a parametric study with different Perforation and Trailing Edge Blowing slot geometries to obtain optimum noise suppression without whistling counter effects. It would also be of great interest to understand the effects of blowing at the leading edge and center of the profile in order to expand the understanding of blowing effectiveness.
- Design potential passive blowing systems to collect the incoming airflow at the crossbar leading edge and blow it at the trailing edge.
- Study the solutions explored in this project numerically through high fidelity CFD and Computational Aeroacoustics (CAA) - see Appendix A.

References

ANGRILLI, F.; BERGAMASCHI, S. and COSSALTER, V. Investigation of wall induced modifications to vortex shedding from a circular cylinder. **ASME Transactions Journal of Fluids Engineering**, vol. 104, 518–522, 1982.

ARBEY, H. and BATAILLE, J. Noise generated by airfoil profiles placed in a uniform laminar flow. **Journal of Fluid Mechanics**, vol. 134, 33–47, 1983.

ARCONDOULIS, E.J.G.; DOOLAN, C.; ZANDER, A.C. and BROOKS, L. A review of trailing edge noise generated by airfoils at low to moderate reynolds number. In **Acoustics Australia / Australian Acoustical Society**, vol. 36. 2011.

BEARMAN, P.W. and ZDRAVKOVICH, M.M. Flow around a circular cylinder near a plane boundary. **Journal of Fluid Mechanics**, vol. 89, 33–47, 1978.

BIMBATO, A.M.; PEREIRA, L.A.A. and HIRATA, M.H. Influence of the wake interference on the vortex shedding flow around a circular cylinder in ground effect. In **20th ABCM COBEM - International Congress of Mechanical Engineering**. 2009.

BROOKFIELD, J.M. and WAITZ, I.A. Trailing-edge blowing for reduction of turbomachinery fan noise. **Journal of Propulsion and Power**, vol. 16, 57–64, 2000.

BROOKS, T.F.; POPE, D.S. and MARCOLINI, M.A. Airfoil self-noise and prediction. Technical Report 1218, NASA, 1989.

BRÜEL&KJAER. **Measuring Sound**, 1984.

BRÜEL&KJAER. **Microphone Handbook**, 1996.

CAVALHEIRO, M.G.; CARDOSO, E.M.; WOISKI, E.R. and VIEIRA, E. Characteristics of the flow around an elliptic cylinder near a smooth flat plate. In **10th ABCM EPTT - Spring School on Transition and Turbulence**. 2016.

CAVALIERI, A.V.G.; WOLF, W.R. and JAWORSKI, J.W. Numerical solution of acoustic scattering by finite perforated elastic plates. **The Royal Society of London A: Mathematical, Physical and Engineering Sciences**, vol. 472, n. 2188, 2016.

CHOI, J.H. and LEE, S.J. Ground effect of flow around an elliptic cylinder in a turbulent boundary layer. **Journal of Fluids and Structures**, vol. 14, n. 5, 697–709, 2000.

CHRUSCIEL, G.T. Active and passive boundary layer tripping. **AIAA - American Institute of Aeronautics and Astronautics**, vol. 54, n. AIAA-97-2016, 1997.

CHUNG, J.Y. and BLASER, D.A. Transfer function method of measuring acoustic intensity in a duct system with flow. **Journal of the Acoustical Society of America**, vol. 68, n. 6, 1570–1577, 1980.

CURLE, N. The influence of solid boundaries upon aerodynamic sound. **The Royal Society of London Series A**, vol. 231, 505–514, 1955.

DAICHIN, S.J.L. Flow structure of the wake behind an elliptic cylinder close to a free surface. **KSME International Journal**, vol. 15, n. 12, 1784–1793, 2001.

DOOLAN, C.J. Aeroacoustic simulation of bluff body noise using a hybrid statistical method. In **Acoustics**. 2009.

ENGHARDT, L.; KAUSCHE, P.; MOREAU, A. and CAROLUS, T. Active control of fan tones by means of trailing edge blowing. In **AIAA Aviation 2015 (21st AIAA/CEAS Aeroacoustics Conference)**. 2015.

EVEREST, F.A. **The Master Handbook of Acoustics**. McGraw-Hill, 4th ed., 2001.

FFOWCS WILLIAMS, J.E. and HALL, L.H. Aerodynamic sound generation by turbulent flow in the vicinity of a scattering half plane. **Journal of Fluid Mechanics**, vol. 40, n. 4, 657–670, 1970.

FFOWCS WILLIAMS, J.E. and HAWKINGS, D.L. Sound generation by turbulence and surfaces in arbitrary motion. **The Royal Society of London. Series A, Mathematical and Physical Sciences.**, vol. 264, n. 1151, 321–342, 1969.

GERHARD, T.; ERBSLÖH, S. and CAROLUS, T. Reduction of airfoil trailing edge noise by trailing edge blowing. **Journal of Physics: Conference Series 524**, vol. 524, 2014.

GOPALARATHNAM, A.; BENJAMIN, A.B.; BRYAN, D.M. and SELIG, M.S. Design of low reynolds number airfoils with trips. **Journal of Aircraft**, vol. 40, 768–775, 2003.

GUPTA, A., **Aeroacoustic investigation of beveled Trailing Edges by high-speed Particle Image Velocimetry**, Master Thesis, Faculty of Aerospace Engineering, Delft University of Technology, 2013.

HIRSCHBERG, A. and RIENSTRA, S.W. **An introduction to Aeroacoustics**. Eindhoven University of Technology, 2004.

IGLESIAS, E.L.; THOMPSON, D.J. and SMITH, M.G. Experimental study of the aerodynamic noise radiated by cylinders with different cross-sections and yaw angles. **Journal of Sound and Vibration**, vol. 361, 108–129, 2016.

JAWORSKI, J.W. and PEAKE, N. Aerodynamic noise from a poroelastic edge with implications for the silent flight of owls. **Journal of Fluid Mechanics**, vol. 723, 456–479, 2013.

JCGM 100:2008. Evaluation of measurement data - guide to the expression of uncertainty in measurement. Standard, ISO/IEC, 2008.

JEONG, D.; WOO, C. and GEUM, . The study of the parameter of roof rack and cross bar for the reduction of wind noise. In **SAE World Congress and Exhibition**. SAE International, apr 2007.

KARBON, K.J. and DIETSCHI, U.D. Computational analysis and design to minimize vehicle roof rack wind noise. In **SAE 2005 World Congress and Exhibition**. SAE International, apr 2005.

KERHO, M.F. and BRAGG, M.B. Airfoil boundary-layer development and transition with large leading-edge roughness. **AIAA - American Institute of Aeronautics and Astronautics**, vol. 35, 1997.

KIM, D.H.; CHANG, J.W. and CHUNG, J. Low-reynolds-number effect on aerodynamic characteristics of a naca 0012 airfoil. **Journal of Aircraft**, vol. 48, 1212–1215, 2011.

KINGAN, M.J. and PEARSE, J.R. Design of automobile components for the minimization of aeroacoustic noise. In **30th International Congress on Sound and Vibration, Vienna, Austria**. 2006.

KUTTRUFF, H. **Acoustics, An introduction**. Taylor & Francis, 2004.

KWON, K. and PARK, S. Aerodynamic characteristics of an elliptic airfoil at low reynolds number. In **35th AIAA Fluid Dynamics Conference and Exhibit, Ontario, Canada**, AIAA 2005-4762. 2005.

LARSSEN, J. Computational aeroacoustics for vehicle applications. 2002.

LEE, M.; LEE, J. and KIM, D. Reduction of aeolian noise from roof rack crossbars using asymmetric cross-section geometry. In **SAE 2002 World Congress and Exhibition**. SAE International, mar 2002.

LIGHTHILL, M.J. On sound generated aerodynamically, part 1: General theory. **Proceedings of the Royal Society of London Series A**, vol. 211, 564–587, 1952.

LOCKARD, D.P. An efficient, two-dimensional implementation of the ffowcs-williams and hawkings equation. **Journal of Sound and Vibration**, vol. 229, 897–911, 2000.

LYON, C.; SELIG, M. and BROEREN, A. Boundary layer trips on airfoils at low reynolds numbers. In **35th AIAA Aerospace Sciences Meeting and Exhibit**, AIAA 97-0511. 1997.

MIYARA, F. **Software-Based Acoustical Measurements**. Springer International Publishing, 2017.

NASH, E.C.; LOWSON, M.V. and MCALPINE, A. Boundary-layer instability noise on airfoils. **Journal of Fluid Mechanics**, vol. 382, 27–61, 1999.

OETTLE, N. and SIMS-WILLIAMS, D. Automotive aeroacoustics: An overview. **Journal of Automobile Engineering**, 2017.

ONUSIC, H.; HAGE, M.M. and BAPTISTA, E. Articulation index (ai): Concepts and applications. In **IX Congresso e Exposição Internacionais da Tecnologia da Mobilidade**, 2000-01-3150. SAE, 2000.

POLLENSKE, M.P. and PFINGSTEN, K. Aeroacoustic performance of an airfoil with circulation control. In **16th AIAA/CEAS Aeroacoustics Conference (31st AIAA Aeroacoustics Conference)**, AIAA 2010-3881. 2010.

RAMIREZ, W.A. and WOLF, R.W. The effects of suction and blowing on tonal noise generation by blunt trailing edges. In **AIAA Aviation 2015 (21st AIAA/CEAS Aeroacoustics Conference)**. 2015.

RAMIREZ, W.A. and WOLF, W.R. Effects of trailing edge bluntness on airfoil tonal noise at low reynolds numbers. **Journal of the Brazilian Society of Mechanical Sciences and Engineering**, vol. 38, n. 8, 2369–2380, 2016.

SANDBERG, R.; JONES, L. and SANDHAM, N. Direct numerical simulations of noise generated by turbulent flow over airfoils. In **14th AIAA/CEAS Aeroacoustics Conference**. 05 2008.

SANTHANAKRISHNAN, A. and JACOB, J.D. Effect of regular surface perturbations on flow over an airfoil. In **35th Fluid Dynamics Conference, Toronto, Canada**. 2005.

SENTHOORAN, S.; DUNCAN, B.D.; FREED, D.; HENDRIANA, D.; POWELL, R.E. and NALEVANKO, J. Design of roof-rack crossbars for production automobiles to reduce howl noise using a lattice boltzmann scheme. In **SAE 2007 Noise and Vibration Conference and Exhibition**. SAE International, may 2007.

STROUHAL, V. Ueber eine besondere art der tonerregung. **Annalen der Physik**, vol. 241, n. 10, 216–251, 1878.

TERAKADO, S.; MAKIHARA, T.; SUGIYAMA, T.; MAEDA, K.; TADAKUMA, K.; TSUBOI, K.; IYOTA, M.; KOSAKA, K. and SUGIYAMA, S. Experimental investigation of aeroacoustic cabin noise in unsteady flow by means of a new turbulence generating device. **SAE International Journal of Passenger Cars - Mechanical Systems**, vol. 10, n. 1, 309–317, mar 2017.

TRINH, V. Measurement of sound intensity and sound power. Technical Report MRL Technical Report MRL-TR-93-32, DSTO Materials Research Laboratory, Department of Defense, Australia, 1994.

VAN DYKE, M. **An album of fluid motion**. The Parabolic Press, 1982.

WANG, X. **Vehicle Noise and Vibration Refinement**. Woodhead Publishing Limited, 2010.

WINKLER, J.; CAROLUS, T.; SCHEUERLEIN, J. and DINKELACKER, F. Trailing-edge blowing on tandem airfoils: aerodynamic and aeroacoustic implications. In **16th AIAA/CEAS Aeroacoustics Conference (31st AIAA Aeroacoustics Conference)**. 2010.

WINKLER, J.; MOREAU, S. and CAROLUS, T. Large-eddy simulation and trailing-edge noise prediction of an airfoil with boundary-layer tripping. In **15th AIAA/CEAS Aeroacoustics Conference (30th AIAA Aeroacoustics Conference)**, AIAA 2009-3197. 2009.

WOLF, W.R.; AZEVEDO, J.L.F. and LELE, S.K. Convective effects and the role of quadrupole sources for aerofoil aeroacoustics. **Journal of Fluid Mechanics**, vol. 708, 502–538, 2012.

WOLF, W.R. and LELE, S.K. Acoustic analogy formulations accelerated by fast multipole method for two-dimensional aeroacoustic problems. **AIAA journal**, vol. 48, n. 10, 2274–2285, 2010.

WOLF, W.R. and LELE, S.K. Aeroacoustic integrals accelerated by fast multipole method. **AIAA journal**, vol. 49, n. 7, 1466–1477, 2011a.

WOLF, W.R. and LELE, S.K. Wideband fast multipole boundary element method: Application to acoustic scattering from aerodynamic bodies. **International Journal for Numerical Methods in Fluids**, vol. 67, 2108–2129, 2011b.

WSZOLEK, G. and ENGEL, Z. Investigations of uncertainty of acoustical measuring instruments applied to noise control. **Archives of Acoustics**, vol. 29, n. 2, 2004.

APPENDIX A - Computational Aeroacoustics

The methodologies for Computational Aeroacoustics (CAA) are summarized in Figure A.1. All the methods except the Direct Numerical Simulation (DNS) (realistic only for very few and simple academic cases) distinguish between sound generation in the *flow-field* (or *near-field*[1]) and sound propagation in the *far-field*. In the *flow-field*, although acoustic waves are present, aerodynamic pressure fluctuations due to turbulence are significantly stronger and dominate. In the *far-field*, turbulence intensity is negligible (no effective generation of sound) so the only phenomena present is acoustic wave propagation. As a general rule of thumb, the *flow-field* is about the size of an acoustic wavelength, and the *far-field* starts several acoustic wavelengths outside the region of noise generation (Larssen (2002)). In order to correctly compute for the sound propagation in the acoustic *far-field*, high fidelity Computational Fluid Dynamics (CFD) methods are required to predict the aerodynamic pressure fluctuations capable of generating aeroacoustic sources in the *flow-field*.

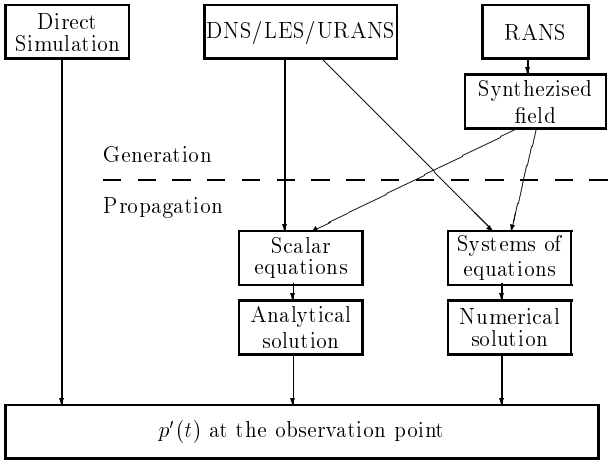

Figure A.1: Overview of Computational Aeroacoustics methods, adapted from Larssen (2002).

CFD tools use numerical methods to solve partial differential equations from the time-transient motions of the fluid flow and from its interaction with surfaces defined by boundary conditions. The traditional CFD approach in automotive engineering is to resolve the Navier-Stokes conservation of mass, momentum, and energy equations through DNS (Direct Numerical Simulation), LES (Large Eddy Simulation) or URANS (Unsteady

[1] *Near-field* is actually the overlapping area between the *flow-field* and acoustic *far-field*, but the interactions between aerodynamic pressure fluctuations and wave propagation are often neglected.

Reynolds Averaged Navier Stokes) formulations. For most of the cases, the solutions to these complex and highly non-linear equations are characterized by many degrees of freedom, thus requiring high computational resources. An alternative approach is to use the Lattice Boltzmann method (LBM) which is a special discretization of the continuum Boltzmann equation in space, time and velocity (Wang (2010)). Instead of solving the Navier–Stokes equations, the discrete Boltzmann equation is solved to simulate the flow of a Newtonian fluid with collision models. The solution obtained from any of the CFD formulations can be post-processed to derive the acoustic excitations that will be modeled as Monopole, Dipole or Quadrupole sources of sound (fundamental aeroacoustic sources).

In low Mach number flows, the acoustic *far-field* domain can be solved separately from the *flow-field*, except for the *two-way* coupled cases where energy is transferred both from the flow to the acoustics and vice-versa (e.g. flows involving resonance, such as the "open cavity buffeting noise" that appears when driving a car with the sunroof or window open[2]). In most of the aeroacoustic modeling cases, the acoustic part is dependent on the flow solution but the flow is independent of the acoustics (*one-way* coupled cases), and the solution can be split. Due to the intrinsic physical difference between flow phenomena (turbulence) and acoustic phenomena (wave propagation), the splitting of the problem is advantageous from the computational point of view.

In automotive aeroacoustic applications, where the most severe noise problems lie in the interaction of the fundamental aeroacoustic sources with rigid surfaces, the computation of the acoustic domain is typically done by resolving the Ffowcs Williams & Hawkings Acoustic Analogy (Ffowcs Williams and Hawkings (1969), Lockard (2000)), which is based based on the Lighthill's Acoustic Analogy (Lighthill (1952)) but takes into account the effects of moving boundaries. Sound scattering on the rigid surfaces of the bodies can be resolved through the Boundary Element Method (BEM) (Wolf and Lele (2010, 2011a); Wolf *et. al* (2012)). However, when the BEM is employed for three-dimensional problems, it needs techniques for the acceleration of the solution of the dense linear systems appearing in the formulation (Wolf and Lele, 2011b).

[2]Vortices in the shear layer radiate sound waves into the passenger compartment. These sound waves are reflected, and when they reach the shear layer, the release of a new vortex is triggered (Larssen (2002)).

APPENDIX B - NACA 0012 Discrete Tones

As discussed in Section 1.5.2, the generated noise from an aerodynamic section has either tonal and broadband characteristics, and contains a superposition of primary ($f_{n,max}$) and secondary (f_n) narrowband tones on a broadband hump (Arbey and Bataille (1983)). Broadband noise is due to a large number of incoherent eddies with a variety of scales and strengths, and the discrete tones are due to reasonably coherent and strong eddies in the trailing edge near wake. The discrete tones can be described in a ladder-structure in function of the airstream velocity. The frequency of the primary tone for a NACA 0012 profile at zero Angle of Attack was empirically fitted by the curve:

$$f_{n,max} = \frac{0.011 U_0^{1.5}}{\sqrt{C\nu}} \tag{B.1}$$

where C is the airfoil chord length and ν is the kinematic fluid viscosity (Arbey and Bataille (1983)). The main tone frequency, and consequently the secondary tones', has also a Strouhal number, airfoil thickness and Angle of Attack dependence. At non-zero Angle of Attack, the amplitude of the discrete tones is significantly higher.

The NACA 0012 profile noise was measured at negative and positive Angles of Attack (AoA=$\pm 3°$) with the objective of measuring the primary and secondary discrete tones. The experimental method adopted is described in Section 2.5. Figure B.1 reveals the narrowband tones occur at positive AoA. At negative AoA, the tones are weak or nonexistent. At 80km/h, four discrete tones with uneven spacing are observed. At 100 and 120km/h, just one primary and one secondary tone are observed at each speed (no ladder-structure with subsequent tones). The occurrence of the tones is being directly influenced by the sound field, with the key factor being the presence of a plane (vehicle roof) 50mm lower the profile.

The frequency of the measured main tones ($f_{n,max}$) was compared to B.1 and the correlation is shown in Figure B.2. Measured and projected values grow linearly at the a similar rate. There are fundamental differences from this study to the experiment of Arbey and Bataille (1983), such as the thickness of the NACA 0012 profile and the acoustic field, however the matching trend suggests the occurrence of the trailing edge tones by the same mechanisms. There is still no formal consensus of the precise cause of trailing edge discrete tones (Arcondoulis *et. al* (2011)). The strongest hypothesis is that at certain frequencies the sound is amplified via an acoustic feedback mechanism near the trailing edge, but the physics of the feedback mechanism is still unclear.

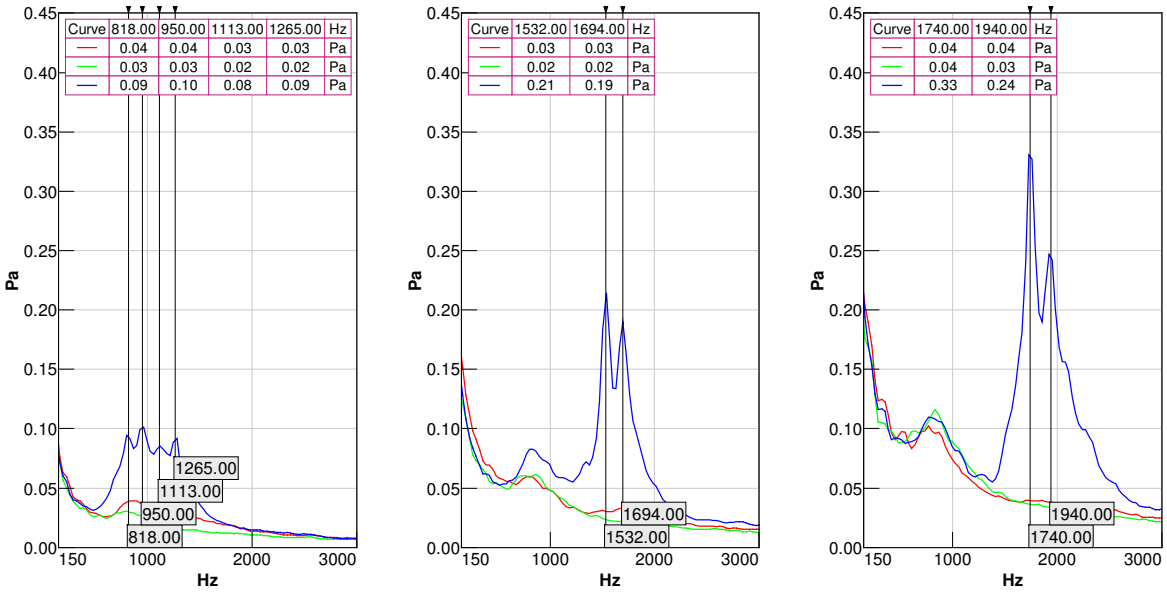

Figure B.1: NACA 0012 Noise at different AoA.
Exterior Acoustic Pressure [Pa], Frequency range: 0.15 – 3kHz.
Wind speeds: 80km/h (*left*), 100km/h (*center*), 120km/h (*right*).
— AoA=0°, — AoA=-3°, — AoA=+3°.

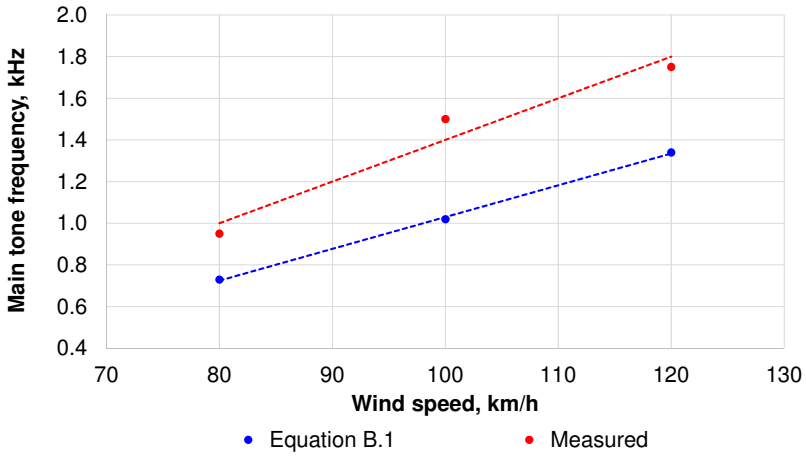

Figure B.2: Correlation of NACA 0012 tones – Measured vs. Equation B.1.

APPENDIX C - Surface Roughness

The characteristics of the Boundary Layer and its separation locations directly affect the noise behavior of an aerodynamic profile. The application of passive and active features at defined locations of the profile is known as the Boundary Layer Tripping technique, extensively discussed in Section 4.1. A secondary mean of changing Boundary Layer behavior is to change the surface roughness of the entire profile. Rough surfaces are capable of keeping the Boundary layer attached for longer than in smooth surfaces, delaying separating and consequently reducing recirculation and form drag (principle of golf dimpled balls and the *Jabulani* and *Brazuca* world cup soccer balls[1]).

With the objective of identifying the effect of different roughnesses on the aeroacoustic noise generated by the airflow around elliptical profiles, two different surface meshes were tested (Figure C.1) and compared to the smooth surface result. Figure C.2 reveals the fine mesh surface (Figure C.1a) did not change both tonal and broadband noise characteristics of the profile when compared to the smooth surface. On the other hand, the coarse mesh (Figure C.1b) significantly changed the noise spectra. The most beneficial effect was the reduction of broadband noise in all speeds, potentially caused by a reduction in the wake thickness and consequent reduction of the quadrupole sources. On the tonal noise, three effects are observed. First, the coarse mesh significantly reduced the bandwidth of the main tone, suggesting the formation of a single and coherent vortex in the near wake. Second, the coarse mesh caused an offset of the main tone center frequency to higher values in lower speeds, but not in higher speeds. In opposite, the coarse finishing increased the tone amplitude in higher speeds, but reduced it in lower speeds. That suggests the coherence of the main vortex and the dipole source loose strength in lower speeds. In higher speeds, the coarse surface crossbar presents the noise characteristics of a blunt body, with a well defined and high amplitude tone.

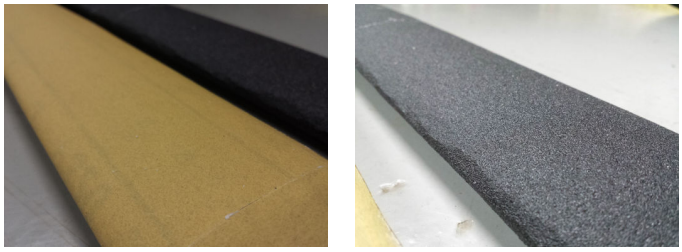

(a) Fine mesh. (b) Coarse mesh.

Figure C.1: Fine and coarse surface crossbars.

[1] `https://www.nasa.gov/content/nasa-turns-world-cup-into-lesson-in-aerodynamics`

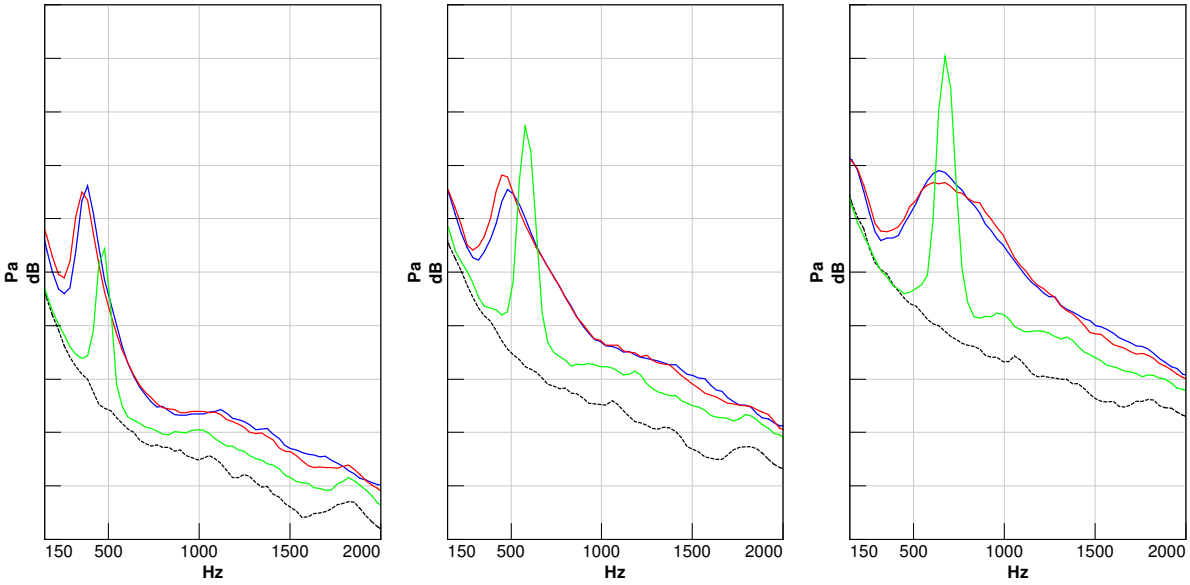

Figure C.2: Surface roughness effect.
Exterior SPL [Grid = 5 dB], Frequency range: 0.15 – 2kHz.
Wind speeds: 80km/h (*left*), 100km/h (*center*), 120km/h (*right*).
— Smooth surface, — Fine mesh, — Coarse mesh, --- No bar.